INFORMATION TO USERS

This manuscript has been reproduced from the microfilm master. UMI films the text directly from the original or copy submitted. Thus, some thesis and dissertation copies are in typewriter face, while others may be from any type of computer printer.

The quality of this reproduction is dependent upon the quality of the copy submitted. Broken or indistinct print, colored or poor quality illustrations and photographs, print bleedthrough, substandard margins, and improper alignment can adversely affect reproduction.

In the unlikely event that the author did not send UMI a complete manuscript and there are missing pages, these will be noted. Also, if unauthorized copyright material had to be removed, a note will indicate the deletion.

Oversize materials (e.g., maps, drawings, charts) are reproduced by sectioning the original, beginning at the upper left-hand corner and continuing from left to right in equal sections with small overlaps.

ProQuest Information and Learning
300 North Zeeb Road, Ann Arbor, MI 48106-1346 USA
800-521-0600

SINGLE POLARITY CHARGE SENSING IN HIGH PRESSURE XENON USING A COPLANAR ANODE CONFIGURATION

by

Clair J. Sullivan

A dissertation submitted in partial fulfillment
of the requirements for the degree of
Doctor of Philosophy
(Nuclear Engineering & Radiological Sciences)
in The University of Michigan
2002

Doctoral Committee:

Professor Zhong He, Chairperson
Professor Glenn F. Knoll
Professor W. Leslie Rogers
Professor David K. Wehe

UMI Number: 3068976

UMI Microform 3068976

ProQuest Information and Learning Company
300 North Zeeb Road
P.O. Box 1346
Ann Arbor, MI 48106-1346

In memory of Brian "Tex" Hanson.

Acknowledgments

First and foremost I would like to thank my advisor, Professor Zhong He, for his years of guidance, insight, and support. It was his help that made this thesis possible. I learned more than I can even express from conversations with him about the research or just educational philosophies in general. More importantly, I wish to thank him for working with me, especially when that was made difficult.

Most importantly, I would like to thank my husband, Michael, and all of my family who supported me and tolerated me during this process. This task, was no doubt, more difficult than anything I did in this thesis.

I would also like to express my thanks to Professor Glenn Knoll who designed the initial helical detector. Despite the fact that it never quite worked right, I will always have fond memories of that detector because it is such an elegant design.

Like many students who have gone before me, I also would like to thank Professor Ziya Ackasu. I have enjoyed our many fine conversations ranging from quantum mechanics to electrostatics to an education in the Turkish language. I also appreciate him looking after me and taking responsibility for me during the final stages of my degree. I even enjoyed being completely devastated in chess by him.

Next, I wish to extend my thanks to Dr. Jose M. Perez. I learned a great deal from him during many invaluable conversations range from subjects on such as coplanar detectors to GEANT and electrostatic simulations. I am grateful that he was able to take so much time out of his schedule to work with me and for the direction and encouragement he gave me.

Thanks are also due to my fellow students, either graduated or not, including Dr. Wen Li, Dr. Yanfeng Du, James Baciak, Carolyn Lehner, Feng Zhang, Dan Xu, Ben Strum and Scott Kiff. They provided a great deal of positive support and

assistance to this research.

This dissertation would not be complete if I did not, in some way, express my thanks to the various people who contributed to my growth as a scientist through various means. These people include Dr. Carla Barrett who was my role model, Michael Montes and Brent Capell who were my humor, Ian Stines who gave me energy, Deanna Butler who was the outside voice of reason, Sandra Shoshani who got me started, Sandra Gregorman who kept me going, Janice Haines who gave me the courage to stand up and try, and Dean Acheson who taught me how to talk about it. Also I would like to extend a special thank you to Chris Loving who kept me sane and whole through this process.

Finally, I would like to thank the person who, through their influence, put me in the position to do this research.

The research was performed under appointment of the Office of Civilian Radioactive Waste Management Fellowship Program administered by Oak Ridge Institute of Science and Education under a contract between the U.S. Department of Energy and Oak Ridge Associated Universities. The equipment for this research was acquired through a U.S. Department of Energy Nuclear Energy Education and Research (NEER) Grant number DE-FG07-99ID13772.

Contents

Dedication ii

Acknowledgments iii

List of Figures vii

List of Tables xi

CHAPTER 1 INTRODUCTION 1
- 1.1 Gas Detectors as used in Gamma-Ray Spectroscopy 2
- 1.2 High Pressure Xenon Gamma-Ray Detectors 4
- 1.3 Single Polarity Charge Sensing in Semiconductor Spectrometers . . . 8
- 1.4 Objectives and Contributions of this Work 10
- 1.5 Overview of Dissertation 11

CHAPTER 2 THEORY 12
- 2.1 Charge Induction as a Means of Signal Creation 12
- 2.2 Single-Polarity Charge Sensing with Frisch Grids 14
- 2.3 Single-Polarity Charge Sensing with Coplanar Anodes 20
- 2.4 Problems Associated with Single-Polarity Charge Sensing 26
  - 2.4.1 Insufficient Potential Between the Anodes for Coplanar Mode Operation 26
  - 2.4.2 Non-equal Gain Between the Anodes and Other Nonuniformities of the Weighting Potential 27
  - 2.4.3 Electron Trapping 31
  - 2.4.4 Signal Degradation due to Other Influences 31
- 2.5 Summary 32

CHAPTER 3 SIMULATIONS AND CALCULATIONS 33
- 3.1 Monte Carlo Simulations 33
  - 3.1.1 Considerations on the Compton Continuum of High Pressure Xenon Spectra 37
  - 3.1.2 Electron Cloud Diameter Calculation 39
- 3.2 Electrostatic Simulations and Calculations 39
  - 3.2.1 Coulomb 4.0 Simulation of Helical Detector 41
  - 3.2.2 Calculation of ΔV_{min} for the Helical Detector 41
  - 3.2.3 Simulation of the Parallel Plate Detector 45

CHAPTER 4 DESIGN 50
4.1 The Helical Design 50
4.1.1 Electric Field Considerations 53
4.2 The Planar Detector 53
4.2.1 Balancing the Weighting Field 55
4.2.2 Calculated Values for the Minimum Potential Difference Required for Complete Charge Collection 58
4.3 Preparation of the HPXe Fill Gas 58

CHAPTER 5 RESULTS AND ANALYSIS OF THE HELICAL DETECTOR 61
5.1 Initial Results 61
5.2 Anode Wire Replacement 64
5.2.1 Electron Cloud Considerations 69
5.2.2 Electronic Noise Analysis 70
5.3 Possible Coplanar Mode Failure Mechanisms 73
5.3.1 Mutual Inductance Between the Anodes 73
5.3.2 Capacitive Coupling of the Anodes 77
5.3.3 Surface Charge Considerations 79
5.3.4 IV Curves 81
5.4 Conclusions about the Helical Detector 92

CHAPTER 6 RESULTS AND ANALYSIS OF THE PARALLEL PLATE DETECTOR 94
6.1 Preliminary Parallel Plate Pulses 94
6.2 Pulse Waveforms After Detector Repair 97
6.3 New Anode Spectra 98
6.4 Analysis of Electronic Noise from Leakage Current and Detector Capacitance 101
6.5 Contribution of Electron Recombination on the Observed Spectra . . 106
6.6 Contribution of Charge Sharing Between the Anodes 108
6.7 Conclusions about the Parallel Plate Detector 113

CHAPTER 7 CONCLUSIONS AND FUTURE WORK 115

References 119

List of Figures

2.1 Normalized induced charge as a function of position within a planar detector. 14
2.2 Representation of the method of mirror charges where the potential, V(x,y,z), is determined by Equation 2.5 and the surface charge, σ(x,y), is calculated by Equation 2.7. 16
2.3 General schematic of a detector with a Frisch grid. 17
2.4 Normalized induced charge as a function of position in the detector for a planar detector with a Frisch grid. 18
2.5 General schematic of a coplanar anode device. A potential difference, $\Delta V > 0$, is established between the collecting and non-collecting anodes. 21
2.6 An examination of the Schockley-Ramo theorem as it applies to establishing the total normalized induced charge on each anode as a function of the location of charge carrier creation. 22
2.7 The normalized induced charge for coplanar anodes as determined by the Schockley-Ramo theorem. The first and second case are shown in black while the third case is shown in red. 24
2.8 The subtracted normalized induced charge for coplanar anodes calculated by subtracting the signal of the non-collecting anode from that of the collecting anode. 25
2.9 Drawing of possible electron cloud scenarios. Cloud A is created directly over the collecting anode and thus there is no charge sharing on the non-collecting anode. Cloud B is shared between both the collecting and non-collecting anodes. 27
2.10 An example of the normalized induced charge on each electrode with the collecting anode at a gain that is slightly higher (Δ) than that of the non-collecting anode. 28
2.11 The subtracted induced charge resulting from the case where the collecting anode is at a higher gain as shown in Figure 2.10. 29
2.12 Typical coplanar anode design for semiconductors. 30

3.1 Calculated mean free path in 0.5 g/cm^3 xenon using the PEGS component of EGS4. 34
3.2 The relative probability of photoelectric effect, Compton scatter, and pair production for 0.5 g/cm^3 xenon. 35
3.3 Simulated ^{137}Cs spectrum for helical detector. 36
3.4 Representation of the parallel plate detector with approximately 1 cm of dead xenon surrounding the detection region. 36

3.5 Simulated ^{137}Cs spectrum for the parallel plate detector. 37
3.6 Illustration of the theorized exponential shape of the Compton continuum for high pressure xenon spectra. 38
3.7 Illustration of the technique used to calculate the electron cloud diameter. In this example, the red dashed line indicates the cloud diameter to be assigned to this particular event. The sinusoidal arrows represent photons whereas the straight arrows indicate the path of a secondary electron created through various interactions. 40
3.8 Schematic of the helical detector as simulated by Coulomb. 42
3.9 Calculated potential along the surface of the anode rod for various values of ΔV and a cathode bias of -5 kV. 42
3.10 Schematic of the boundary conditions used to solve for the potential distribution within the helical detector. 44
3.11 Calculated value of ΔV_{min} as a function of cathode bias for the helical detector. 45
3.12 Calculated potential of the helical detector as a function of distance directly beneath the non-collecting anode for the case where $\Delta V = \Delta V_{min}$. 46
3.13 Calculated three-dimensional potential of the helical detector for the case where $\Delta V = \Delta V_{min}$ for one pitch (4 mm) of the detector. 46
3.14 Schematic of the parallel plate detector used for the calculation of ΔV_{min}. 47
3.15 Calculated value of ΔV_{min} as a function of cathode bias for the parallel plate detector. 49

4.1 Drawing of anode configuration of the helical detector. The solid and dashed lines represent two different wires wound about the ceramic core comprising the collecting and non-collecting anodes. The pitch of the wires is 4 mm. 51
4.2 Schematic of the complete helical detector. The outer walls of the pressure vessel (not shown) are made of stainless steel. 52
4.3 Calculated weighting potential for the helical detector. 54
4.4 Spiral pattern used for the planar HPXe detector. The inner electrode strip and gap widths are 1 mm creating a total pitch of 4 mm. The "y direction" is considered to be in the vertical direction. 56
4.5 The calculated potential 4 mm below the anode surface along a vertical line through the center of Figure 4.4 with 1000 V applied to the anode of interest. 56
4.6 The calculated difference in weighting potential expressed in percentage between the two ideal anode designs. 57
4.7 Schematic of the gas purification system used for the xenon in this work. 59

5.1 Sample pulses obtained with cathode bias of -5 kV and ΔV = 800 V on a time scale of 200 μs/division. 63

5.2 ^{137}Cs spectrum for the helical detector with a cathode bias of -5 kV and ΔV = 1500 V. 63
5.3 Initial spectra from the collecting anode and subtraction circuit for ^{137}Cs with ΔV = 900 V and a cathode bias of -3 kV. 64
5.4 Representation of the possible problem associated with electrodes submerged beneath an insulating surface. One possible electric field line is shown. 65
5.5 Helical detector spectra for the original and new anode wires, obtained with a cathode bias of -3 kV and ΔV = 700 V. 67
5.6 ^{137}Cs spectrum obtained with the anode wire refit with a cathode bias of -3 kV and ΔV = 600 V. 68
5.7 Measurement of the bulk leakage current contribution to the electronic noise of the helical detector. 71
5.8 Measurement of the surface leakage current contribution to the electronic noise of the helical detector. 72
5.9 Schematic of initial anode rod simulation experiment. Charge is injected through a 2 pF capacitor on the upper left. The dashed lines indicate the electrode the induced signal is expected to appear on. The signal is measured through a charge-sensitive preamplifier. . . . 75
5.10 Sample data for the inductive coupling measurement where a 58 mV voltage pulse (yellow) is injected as a charge pulse on one anode while observing the coupled signal (green) on the other anode. 75
5.11 Schematic of initial anode rod simulation experiment, similar to that shown above. In this case, the charge is injected from the opposite side of the rod. 76
5.12 Output of the inductive test with a 58 mV pulse injected with the leads reversed. 77
5.13 Setup for the measurement of capacitive coupling. In the first case, the pulse height of a test pulse is measured with the anode floating. In the second case, one anode is connected to the preamplifier while the other is grounded. 78
5.14 Calculated potential resulting from varying charge densities on the anode rod surface. 80
5.15 Experimental setup used for the IV curve measurements. The current was measured with a Keithley 6514 System Electrometer. 82
5.16 Current stability profile between anodes of the helical detector with ΔV = 500 V. 84
5.17 Current stability profile between anodes of the helical detector with ΔV = 1000 V. 84
5.18 IV curve between anodes for the helical detector using the sixth data point and a time delay of 300 s for 0 V $\leq$ V $\leq$ 1000 V. 85
5.19 IV curve between anodes for the helical detector using the sixth data point and a time delay of 300 s for -1000 V $\leq$ V $\leq$ 0 V. 86
5.20 Current fluctuations observed with the electrometer not connected to the detector using the sixth data point and a time delay of 300 s. . 86

5.21 IV curve between anodes for the helical detector when the electrometer was recalibrated after the first leg. 87
5.22 Representation of current flow with two dissimilar metals in contact where $\Phi_1 > \Phi_2$. 88
5.23 IV curves taken with the cathode floating, cathode biased at -5 kV, and cathode bias with a gamma-ray source. 90
5.24 Schematic representation of the movement of electrons created by a gamma-ray source as ΔV is increased. 91

6.1 Example of the baseline fluctuation problem for ΔV = 300 V with no triggering at a time scale of 20 ms/division. 96
6.2 Sample coplanar pulses obtained with a cathode bias of -4 kV and ΔV = 300 V on a time scale of 100 μs/division. 98
6.3 Sample coplanar pulses at a time scale of 10 μs/division, illustrating the slow rise as the electrons drift within the bulk and then the deviation between the collecting and non-collecting anode signals as the electrons are diverted to the collecting anode. 99
6.4 ^{137}Cs spectrum for a cathode bias of -4 kV and ΔV = 300 V. 100
6.5 ^{137}Cs spectrum for a cathode bias of -3 kV and ΔV = 300 V. 100
6.6 Comparison of the ^{137}Cs spectra for the parallel plate detector operated in the classical ionization chamber mode versus coplanar mode. 101
6.7 Measurement of the electronic noise of the parallel plate detector as a function of ΔV for various cathode biases. 102
6.8 Measurement of the electronic noise of the parallel plate detector as a function of cathode bias for various values of ΔV. 103
6.9 Schematic of the electronic circuit equivalent of the various detector capacitances. Here, C_{A-A} is the anode-anode capacitance, C_{A-PV} is the anode-pressure vessel capacitance, and C_{BE-PV} is the boundary electrode-pressure vessel capacitance. 105
6.10 ^{137}Cs spectra with ΔV = 300 V for various cathode biases. 109
6.11 ^{137}Cs spectra with ΔV = 400 V for various cathode biases. 109
6.12 Results demonstrating the effect of electron trapping as a function of cathode bias. 110
6.13 Weighting potential of the coplanar anode detector. The additional purple line indicates the summed weighting potential of the collecting and non-collecting anodes. P is the depth one pitch width from the anode surface. 111
6.14 Sample pulse waveforms used to determine variations in the shaped pulse amplitude. 112
6.15 Pulse amplitudes for a series of pulses originating near the cathode. . 113

List of Tables

1.1 Selected properties of high pressure xenon 5

4.1 Comparison of area-weighted difference in weighting potential . . . 58

5.1 Results of inductive coupling measurement 76
5.2 Results of capacitive coupling measurement between the two anodes 79
5.3 Values of the work function for several of the metals used in this experiment [68] 89

6.1 Measurements of the various capacitances of the parallel plate detector (all units in pF) 103
6.2 Calculated contributions to the broadening of the photopeak with a cathode bias of -3 kV and ΔV = 300V 106
6.3 Summary of data from ^{137}Cs spectra for the parallel plate detector as a function of cathode bias and ΔV. 108

Chapter 1

INTRODUCTION

Many areas of science including astrophysics, nuclear medicine, nuclear non-proliferation, and waste management rely on the efficient and accurate detection of gamma rays. Frequently it is necessary to be able to detect gamma rays with a high efficiency and determine what isotope is emitting them by identifying the energy of this emission. By measuring the energy of the gamma ray emitted by a source, one is able to determine the isotope of emission. In waste management, knowing what isotope is being detected can be an important piece of information for the remediation process. In nuclear medicine, being able to efficiently detect the gamma rays can lead to the minimization of the dose of radiation to a patient.

While the locations and source strengths of the radioisotopes can differ significantly based on the application, the need for good efficiency and energy resolution is important for proper discrimination of different sources. Several different types of radiation detectors exist that are capable of achieving this to some level. However, many of these detectors suffer from poor energy resolution. Those that achieve good energy resolution frequently require some sort of cooling mechanism such as the use of liquid nitrogen. These cooling mechanisms are generally quite bulky and difficult to handle. Thus a detector with good energy resolution capable of operating at room temperature would be a great advantage.

A great deal of work has been done on developing semiconductor radiation detectors such as CdZnTe, CdTe, and HgI_2 for high resolution spectroscopy. Through the development of techniques for single polarity charge sensing, these detectors have achieved excellent energy resolution. However, to date it is very difficult to grow semiconductors larger than about 1 cm^3 with good material properties, thus

limiting their efficiencies. Gas ionization chambers, on the other hand, are capable of comparable energy resolutions with much larger volumes. They suffer from various limitations based on how they achieve single polarity charge sensing, such as energy resolution degradation due to vibrations of the Frisch grid. This dissertation involves the development of a high pressure xenon ionization chamber using the method of coplanar anodes to perform gamma-ray spectroscopy in the energy range of 0.1–2 MeV.

1.1 Gas Detectors as used in Gamma-Ray Spectroscopy

Gas chambers have long been used as a detector for gamma ray spectroscopy due to their simple design and construction, and the ability to create chambers of a large volume thus improving their efficiency. The simplest of the gas detectors is the ion chamber. In this design, a gamma ray enters the active volume of the detector where it ionizes gas molecules creating electron-ion pairs. By the application of an electric field, the electrons drift towards the positively biased anode while the ions move towards the negatively biased cathode. In an ideal detector, the output signal is directly proportional to the induced charge on the electrodes of the detector, which is directly proportional to the deposited energy within the detecting medium. One consideration in the use of ion chambers is that the total amount of charge created within the gas is typically quite small, on the order of 10^{-15} C, thus requiring significant amplification. However, ion chambers are more suited for gamma-ray spectroscopy as their energy resolution is the best among the gas detectors since the ultimate limit is only the Poisson statistics governing the number of electron-ion pairs created in a single event.

When gas detectors are operated at high electric fields, gas multiplication can occur as is the case with proportional counters. In this case, the electrons created within the gas are greatly accelerated by the strong electric field. Their kinetic energy can exceed the binding energy of the electrons in the gas. Thus, a collision with a gas molecule can free another electron. This process will continue until all of the charge has been collected. One of the advantages of the proportional

counter is that there is a significant increase in the amount of charge produced within the detector due to the gas multiplication process. Hence, less amplification is required relative to ionization chambers. However, this multiplication adds additional sources of fluctuation in the number of charge carriers and thus yields worse energy resolution. Eventually as the electric field is increased further, the gas multiplication becomes an avalanche of charge, as is the case with Geiger-Mueller (GM) counters. With GM counters, each event results in an avalanche of the same size, making it impossible to perform spectroscopy since all pulses are of equal amplitude.

There are problems inherent to radiation detectors that rely on the collection of the positive charge carrier for the generation of a pulse of full amplitude. When an electron is released from an atom, the result is an electron-ion pair. Consider a detector that is made up of two parallel plates with the ion pair formed at some arbitrary point in between the two. The electron and ion are prevented from recombining by an applied electric field which draws the two apart from each other. In the simplest description, it is the collection of both the electron and ion that result in a signal. If we consider the detector to be a capacitor, the full voltage will only develop over that capacitor once all of the charge has migrated to each electrode. Hence, we require the complete collection of both the electrons and ions in order to determine the amount of energy deposited within the detector.

This process is complicated by the fact that electrons and ions travel at different velocities through the gas. Their velocities are directly proportional to the electric field within the detector as well as the mobility of each of these charge carriers. However, the electron and ion have vastly different mobilities. The electron mobility can be as great as 1000 times that of the ions. Hence, the ions move exceptionally slowly within the gas. This situation is further complicated by the fact that these gases have impurities which easily trap slow-moving particles such as the ions. If these particles are trapped, the full charge cannot develop between the two electrodes and the signal is not as strong as it should be. This results in the worsening of the spectral resolution of the system. So it is clear that a method by

which the signal due to the ions would not be required would be ideal. This leads to the idea of single polarity charge sensing which was historically developed for gas detectors by means of the Frisch grid.

The Frisch grid was developed as a means of allowing for single polarity charge sensing within a gas detector. The grid is made of a wire mesh that is located close to the anode at an intermediate potential electrostatically shielding the anode from the cathode. The resulting signal only develops on the anode once the electrons have passed between the grid and the anode, but is not a function of interaction location or movement of the ions to the cathode.

1.2 High Pressure Xenon Gamma-Ray Detectors

With any type of gamma-ray detector, the ideal interaction process is the photoelectric effect since all of the energy of the gamma ray is deposited within the detector. The probability of a photoelectric interaction within a material increases as a strong function of the atomic number, Z, of the material. Hence, it is desirable to use detection media that have as high a value of Z as possible.

Xenon (Z=54) poses an attractive possibility for gamma-ray spectroscopy due to its relatively high Z value. In addition, it is a noble gas making it exceptionally stable. Xenon also has thermodynamic properties that make it very compressible around its triple point thus increasing the probability of interaction by increasing the density through minimal changes in pressure to the containment vessel. Since the probability of interaction within the detection medium is also strongly dependent on the density of the medium, a material that permits operation at high pressures is advantageous. Some of the properties of high pressure xenon are indicated in Table 1.1.

The initial work that made xenon a viable detection medium involved a detailed analysis of the electron mobilities in xenon as a function of density. [56] It was found that electron mobility was not a function of temperature, thus making it a good candidate for room-temperature radiation detectors. Additionally, the electron velocity as a function of xenon density was observed to saturate at a given

Table 1.1: Selected properties of high pressure xenon

Atomic Number	54
Usable Density	0.3–1 g/cm^3
Triple Point	57 atm, 16.6 °C, 1.09 g/cm^3
Fano factor	0.14
Statistical Limit of Energy Resolution	0.5% for 662 keV photons
Average ionization energy	21.9 eV/ion pair

drift field.

Early research into using high pressure xenon for radiation detectors was performed by Dmitrenko et al. who created a cylindrical ionization chamber 50 cm in length and 6 cm in diameter filled to a pressure of 60 atm (1 g/cm^3). [37] In this preliminary work, the detector did not have a Frisch grid, however energy resolutions of 5.4% were obtained for 662 keV gamma rays. This detector also displayed excellent energy linearity. Other detectors built by this group in the same era exhibited similar results. [38] It was also presented that the addition of a slight amount of H_2, typically 0.5-1.5%, to the xenon decreased the electron thermalization time and hence the drift time thus further improving the energy resolution.

However, the energy resolutions obtained by Dmitrenko et al. differ greatly from the Fano-factor predicted value of 0.5% at 662 keV. Bolotnikov et al. demonstrated that the energy resolution is a strong function of xenon density. [19] For densities greater than 0.6 g/cm^3, it was shown that recombination of the electron-ion pairs on delta-electron tracks dominated the energy resolution. For densities less than 0.6 g/cm^3, the resolution was found to be dependent only on the fluctuation in the number of electron-ion pairs and not a function of density. Also, it was shown that the energy resolution was not a function of electric field for fields greater than approximately 2 kV/cm, corresponding to the saturation of the electron drift velocity. [16] Further studies confirmed that there was no significant degradation in energy resolution for drift field strengths above 1.3 kV/cm at these densities. [65] This work also demonstrated that there was no increase in the average charge collected as a function of density for densities greater than 0.5 g/cm^3.

Hence, the only drawback for operating at a lower density than 1 g/cm^3 is a loss of detection efficiency. However, this can be minimized by creating a detector with a larger sensitive volume to increase the probability of interaction.

Since it was shown that the primary means of resolution degradation is due to fluctuations in the number of electron-ion pairs, it is necessary to eliminate any non-Poisson sources of deviation such as electron recombination with electronegative impurities within the gas. Contamination less than one part per million is required for adequate spectroscopy in HPXe. [98] It is also necessary to ensure that the detector be constructed of parts that do not outgas these impurities. All materials in contact with the gas must be rated for ultra-high vacuum conditions. Additionally, they must also be capable of withstanding the extremely high pressures involved when the xenon is added to the chamber.

Much work was done to optimize xenon purification techniques to minimize the concentration of electronegative impurities such as H_2O, CO, and CO_2. [42] [14] [16] Two techniques have been reported for gas purification. The first involves the use of oxisorbs, molecular sieves, and high-temperature getters. In this technique, the gas is passed through material such as titanium that, at elevated temperatures, adsorbs water easily. Typically this process requires several passes in order to obtain sufficient purity. This technique has been widely used with xenon detectors of lower pressures for low-energy x-ray detection and is useful for obtaining an initial level of gas purity. However, it is a slow process requiring many iterations to obtain good purity. [87] [74] The second method utilizes a spark discharge to break apart large molecules. [15] Usually the discharge is created with electrodes of metals that water readily adsorbs to. So any dust created in the sparking process acts as a getter that prevents the water from remaining in the gas to be used in the detector. While this technique requires an initial high level of gas purity, it is a relatively fast purification process capable of attaining higher levels of purity. For the work described herein, the spark chamber purification process was used.

In addition to the purification techniques, measuring the level of impurity is

of concern. Some work has been conducted to measure gas impurity using mass spectroscopy, however this can be an expensive option. [98] Instead, a simple technique involving pulse waveform analysis has been used as an indication of gas purity. [14] In this technique, an electron cloud created within the gas is monitored as it drifts under the influence of an electric field. The shape of the pulse can indicate the electron lifetime within the gas. Dense electron clouds are created by highly-ionizing cosmic muons and the drift time of such clouds is an indication of the lower limit on the gas purity. Using these techniques, it was reported that no degradation in energy resolution was observed until the electron lifetime was less than 0.5 ms.

The best energy resolution to date with HPXe detectors has been obtained with either large, gridded chambers or through pulse rise-time compensation. [74] [15] [61] [102] In both of these cases, the energy resolution obtained was 2.0–2.2 % at 662 keV, however the pulse rise-time compensation method eliminates many events from the overall spectrum resulting in a low count rate unless exceptionally large shaping times are used. Yet these results still differ significantly from the predicted energy resolution for HPXe. One widely-cited explanation for this is due to vibrational instabilities of the Frisch grid, especially at vibration frequencies less than approximately 100 Hz. [35]

In addition to its ionization properties, xenon gas is also a scintillator with the wavelength of emission in the UV region at about 170 nm. Collecting the scintillation light from HPXe can be technically difficult as it requires creating an optically-transparent window in the pressure vessel to couple a light-collecting device such as a photomultiplier tube or a photodiode. Later detectors reported by Tepper and Losee used the scintillation light as a means of triggering the charge-sensitive preamplifier, however no improvement in energy resolution over previously-reported values was obtained. [99]

Later work demonstrated that HPXe is a viable detector for field work. It has been shown that the energy resolution for a gridless detector does not significantly degrade as a function of temperature. [104] As a result, this makes them an in-

teresting candidate for well-logging applications where the elevated temperature rules out the use of most semiconductors and scintillators. A small, cone penetrometer HPXe detector has been reported with comparable energy resolutions of approximately 3.1%. [81] Most notably, HPXe detectors have demonstrated long-term stability under the harsh conditions of space onboard the Mir space station. [18]

Most recently, different detectors have been constructed to attain good energy resolution with designs that have branched away from the traditional gridded detectors. For example, one hemispheric detector has been reported with a small anode pixel to perform single polarity charge sensing through the "small pixel effect" used in semiconductors. [62] Due to a design flaw, this detector has not yet recorded spectra, however it poses an interesting alternative to the Frisch grid. Other detectors have been constructed to form an array of chambers for imaging purposes using resistive cathode wires between each detector to determine the two-dimensional position of interaction within the array. [5]

Despite nearly two decades of research and several advances to the knowledge in the field, no high pressure xenon detector has been built demonstrating better than 2% energy resolution. This is still much worse than the Fano factor-predicted minimum of 0.5% for 662 keV gamma rays. This suggests other methods of single polarity charge sensing should be considered for these detectors.

1.3 Single Polarity Charge Sensing in Semiconductor Spectrometers

Semiconductors such as CdZnTe gained popularity as a medium for gamma-ray detection due to their high density and wide band gap energy (1.70 keV) making them a good prospects for room-temperature spectroscopy. However, the first results for CdZnTe obtained resolutions much greater than the predicted minimum of 0.2% (assuming the only peak broadening is due to statistical fluctuations in the number of charge carriers) for 662 keV due to the limitations of severe hole trapping. [72] Similar problems had been overcome by gas detectors by the im-

plementation of the aforementioned Frisch grid to perform single polarity charge sensing. A means of Frisch grid operation was thus desirable for semiconductors.

In 1994, Luke discovered the technique of coplanar anodes to achieve this goal. [69] [70] This method, based on the Schockley-Ramo theorem for the calculation of induced charge on an electrode is the theory behind the true operation of a Frisch grid. [48] The technique involves the use of interdigitized strip electrodes as anodes that are biased at alternating potentials. One set of strips, called the "collecting anode," is placed at a higher potential relative to the other set of strips or "non-collecting anode", thus collecting all of the electrons. Through the Schockley-Ramo theorem, it can be proven that the difference in induced charge between the anodes is directly proportional to the charge deposited within the detector and not based on the movement of the positive charge carriers or the position of interaction within the detector. [47] This is equivalent to the function of a Frisch grid in gas-filled ionization chambers. Energy resolutions obtained with the first coplanar anode detectors were initially approximately 5% and improved with later generations of coplanar detectors to 2.4% for 662 keV gamma rays. [69] [72]

As a result of this preliminary study, work was conducted to optimize the coplanar anode design. It was determined that the majority of the broadening of the photopeak occurred from interactions near one pitch width of the anode surface where deviations in the normalized induced charge, or weighting potential, would be most detrimental. [51] To correct this, emphasis was placed on developing coplanar anode designs that would balance the weighting potential in this crucial region as much as possible. This was achieved by the incorporation of a boundary electrode, whose purpose was to balance the weighting potential of the two anodes on the edge of the detector. Further improvements in the energy resolution were observed when the widths of the outermost strips were altered in size so the difference in the weighting potentials of the two anodes was minimized. The result was an improvement in energy resolution to 1.79% for 662 keV gamma-rays. [52] When this design was incorporated, it was also demonstrated that the broadening of the photopeak was, in fact, not from poor electron collection due

to material defects, but the result of small imbalances of the weighting potential across the detector. [51]

The concept of single-polarity charge sensing was also achieved through the use of small, pixel anodes whose size is much smaller than the detector thickness. It was determined that the "small pixel effect" could attain similar weighting potentials to the Frisch grid or coplanar anodes. [9] Through the use of small pixels, it is possible to attain three-dimensional position sensing. The two-dimensional interaction location is determined by the pixel of maximum signal amplitude. Depth information is obtained by taking the ratio of the signals from the cathode to anode pixel. By doing so, energy resolutions as good as 1.51% have been reported for CdZnTe. [53] It has also proven a successful technique for other semiconductors such as HgI_2 where the resolution has been improved from several percent to 1.4% for 662 keV photons. [8] [7] This same technique has also been applied to obtain spectra from multiple-pixel events. If the timing of the multiple interactions can be accurately measured, it is possible to determine through coincidence measurement techniques which events correspond to a single incident gamma ray. Using a 1x1x1 cm detector energy resolutions of 3.8% were initially obtained for two interactions separated by more than one pixel distance. [67] This was later improved to 2.7% with a 1.5x1.5x1.0 cm CdZnTe detector. [107]

1.4 Objectives and Contributions of this Work

This thesis attempts to enhance the basic high pressure xenon ionization chamber by replacing the Frisch grid with a coplanar anode system similar to those used in semiconductor spectroscopy research. The work presented here represents the first time the coplanar anode design has been used in a gas ionization chamber. The result of this research is a series of detectors, both parallel plate and cylindrical in design, that lack a classical Frisch grid but are still capable of single polarity charge sensing. While the detectors did not demonstrate energy resolutions comparable with other high pressure xenon detectors, it was intended that they simply prove that the concept of single polarity charge sensing with coplanar anodes can work

in a gas detector. A detailed analysis of the factors limiting the energy resolution has been performed to aid in future designs.

1.5 Overview of Dissertation

The goal of this dissertation is to answer the basic question of whether or not it is possible to operate a high pressure xenon detector in coplanar anode mode. This was achieved through the simulation, design, and testing of two different designs of high pressure xenon detector. The first detector constructed was of a cylindrical geometry with helical anode wires. The second detector built was a parallel plate design. Though neither detector functioned perfectly, it will be shown that the method of coplanar anodes works with high pressure xenon and offers an improvement over classic ionization chamber operation.

This dissertation contains six subsequent chapters discussing the development, testing, and results of two different coplanar anode high pressure xenon detectors. The second chapter focuses on the theory behind the coplanar anode design for single polarity charge sensing. The main concept presented here is the Schockley-Ramo theorem, which is the basis for the coplanar anode. In the third chapter, simulations will be presented as to the expected results of these detectors. These simulations can be divided into two distinct sections: electromagnetic simulations of the anodes and complete detector to establish optimal designs and Monte Carlo simulations to determine the expected resulting spectrum. Chapter 4 describes the designs themselves and how they were selected. The techniques used to purify and fill the xenon used in these detectors is presented here. The fifth chapter focuses on the results and analysis from the helical detector. This detector exhibited unusual results which are described and used as the motivation for the construction of the parallel plate detector. This detector was meant to be a simple design to prove the principle of coplanar anode operation in high pressure xenon. The results from this detector are presented in Chapter 6. Lastly, the seventh chapter states the conclusions of this research and poses suggestions for future work.

Chapter 2

THEORY

The fundamental process to be examined in this work is the creation of a signal by the motion of electrons created within the detector. First, the induction of charge on an electrode is introduced as a means to developing an understanding of the Schockley-Ramo theorem to calculate the induced charge from the motion of charge carriers. This formalism will be applied to the idea of single-polarity charge sensing through two different cases involving Frisch grids and coplanar anodes. Last it is important to consider different processes such as electron trapping that would result in deviations from the expected ideal cases developed by the Schockley-Ramo theorem.

2.1 Charge Induction as a Means of Signal Creation

In order to calculate the induced charge on an electrode, it is convenient to use the Schockley-Ramo theorem for induced charges. [48] This theorem applies the tool of weighting potentials or normalized induced charge and fields in order to calculate the instantaneous induced current on an electrode. Based on this theorem, the current is given by

$$i = q\vec{v} \cdot \vec{E_w} \tag{2.1}$$

where q is the charge with a velocity of $\vec{v}$ and $\vec{E_w}$ is the weighting field. The total induced charge on an electrode is

$$Q = q\Delta\phi_w \tag{2.2}$$

where $\Delta\phi_w$ is the change in the normalized induced charge or weighting potential. The weighting potential and field are not the same as the operating potential and

electric field within the detector. The operating potential and field are established by the bias applied to the detector. However, this bias does not determine the nature of the induced charge on each electrode. Instead, the weighting potential and field are used as a tool for calculating the induced charge on any given electrode.

The weighting potential of Equation 2.2 is determined by solving the Laplace equation

$$\nabla^2 \phi = 0 \tag{2.3}$$

with the following artificial boundary conditions:

1. The potential on the electrode of interest is set to an arbitrary value of 1.
2. All other potentials are set arbitrarily to zero.
3. Even if trapped charges exist within the detector, they are ignored. This permits the use of Equation 2.3 instead of a more difficult calculation via the Poisson equation.

For the applications of interest in this work, it is simple to use the Schockley-Ramo theorem to determine the normalized induced charge on an electrode. For example, consider the case of a simple, parallel plate detector with an anode and cathode separated by a distance, d with a negative bias applied to the cathode. In this case, the operating electric field established between the cathode and anode will be constant. The operating potential will simply be a function of distance from the cathode established as

$$V(x) = Ex \tag{2.4}$$

where x is the distance from the cathode and E is the electric field.

However, when using the Schockley-Ramo theorem, the operating potential and field are not calculated. Instead the total normalized induced charge on one of the electrodes is determined. In this case, consider the induced charge on the anode. As shown in Figure 2.1, a value of one is assigned as the normalized induced

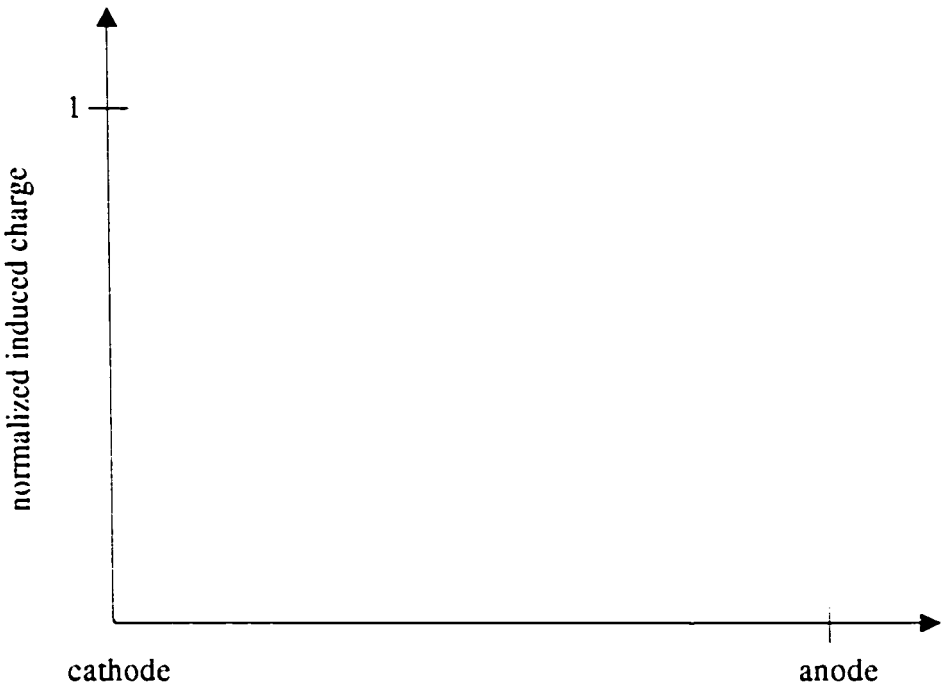

Figure 2.1: Normalized induced charge as a function of position within a planar detector.

charge on the surface of the anode and a value of zero to the cathode. The induced charge on the anode will increase linearly as a charge carrier moves between the cathode and anode. Thus a linear relationship is obtained between the total normalized induced charge on the anode as a function of distance to the anode.

This case represents the simplest use of the Schockley-Ramo theorem, however its true impact will be realized in future sections as more complicated cases are presented.

2.2 Single-Polarity Charge Sensing with Frisch Grids

Due to the fact that the ions move so slowly within the gas and easily recombine, the Frisch grid was developed to allow for single polarity charge sensing with a

gas detector. In this case, a physical grid is built within the chamber between the anode and cathode kept at an intermediate potential as demonstrated in Figure 2.3 (neglecting the effects of the walls of the detector). As the electron and ion move apart due to the influence of the drift field, the Frisch grid electrostatically shields the anode from any movement of charge. However, once the electron passes the grid, it begins to induce a signal on the anode. As the electron moves closer to the anode, the induced charge increases. In order to calculate the charge induced on a conductor due to a point charge elsewhere, the following equation must be solved:

$$V(x,y,z) = \frac{1}{4\pi\epsilon_0}\left[\frac{q}{\sqrt{x^2+y^2+(z-d)^2}} - \frac{q}{\sqrt{x^2+y^2+(z+d)^2}}\right] \tag{2.5}$$

where q is the charge and d is the distance of the charge from the conducting surface. This problem is illustrated in Figure 2.2. The potential on the surface is then given by

$$\sigma = -\epsilon_0 \frac{\partial V}{\partial n} \tag{2.6}$$

where $\frac{\partial V}{\partial n}$ is the normal derivative at the surface. By taking the derivative of Equation 2.5, it can be shown that

$$\sigma(x,y) = \frac{-qd}{2\pi(x^2+y^2+d^2)^{\frac{3}{2}}}. \tag{2.7}$$

Since the total induced charge, Q, is the integral of the induced surface charge,

$$Q = \int \sigma da \tag{2.8}$$

using plane polar coordinates where $r^2 = x^2 + y^2$ and $da = rdrd\theta$, then

$$Q = \int_0^{2\pi}\int_0^{\infty} \frac{-qd}{2\pi(r^2+d^2)^{\frac{3}{2}}} rdrd\theta = -qd\frac{-1}{\sqrt{r^2+d^2}}\Big|_0^{\infty} = -q. \tag{2.9}$$

Based on this formalism, it is clear that if there is a a charge q at a distance d, there will be an opposite charge of $-q$ induced on the electrode. For the purpose of calculations, this mirror charge is considered to also be a distance d from the electrode surface. As d decreases, the charge induced on the electrode increases. However, in the case of a detector with a Frisch grid, charge is not induced on the

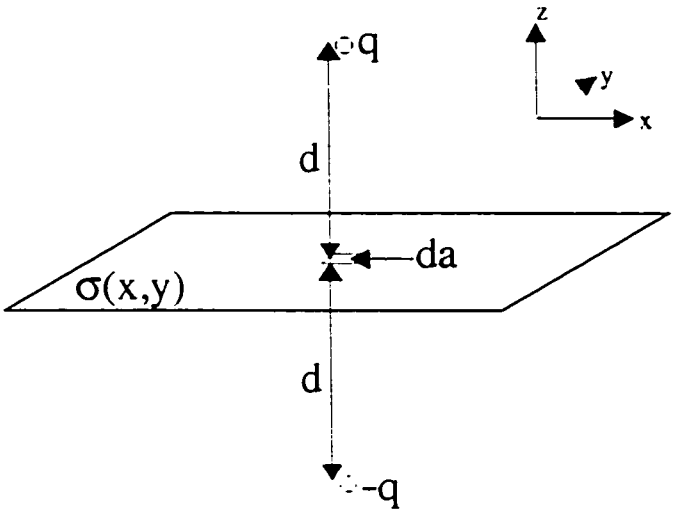

Figure 2.2: Representation of the method of mirror charges where the potential, V(x,y,z), is determined by Equation 2.5 and the surface charge, σ(x,y), is calculated by Equation 2.7.

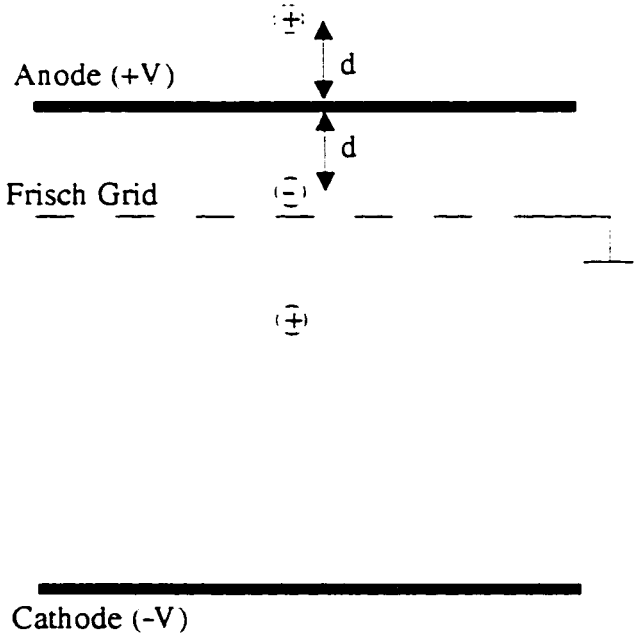

Figure 2.3: General schematic of a detector with a Frisch grid.

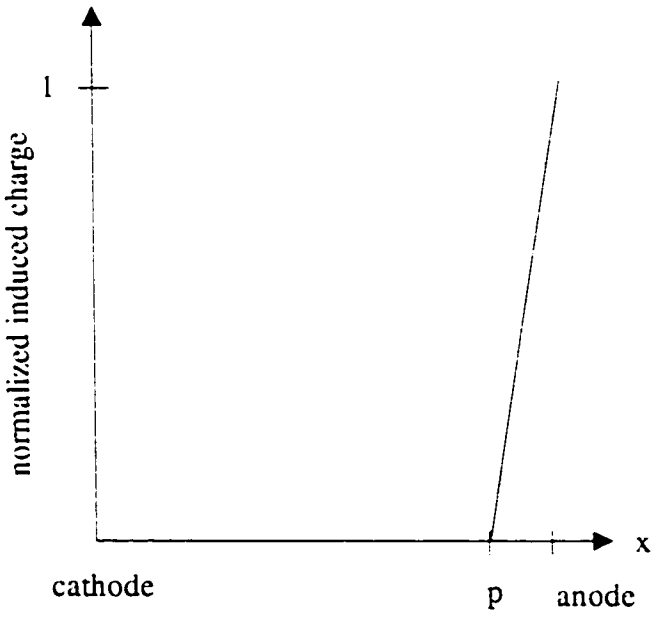

Figure 2.4: Normalized induced charge as a function of position in the detector for a planar detector with a Frisch grid.

anode until it passes the grid, which shields the anode from any other charges in the bulk of the detector.

It is important to note here that for a gridded detector, at no point does the motion or collection of the ions contribute to the signal, assuming the region between the grid and the anode is small enough that interactions within this region are rare. Charge is induced on the anode only once the electrons have crossed the Frisch grid and the signal develops only based on the motion and collection of the electrons. Hence, the Frisch grid is an effective way of doing single-polarity charge sensing in a gas detector. This development greatly improved the spectral response of these detectors since they were previously limited by the slow, easily-trapped ions.

While the general principles behind the Frisch grid are simple, understanding the formation of the output can be quite complicated, especially for more elaborate geometries. However, if one uses the Schockley-Ramo theorem, determining the signal generated by the motion of the electrons is quite simple.

In this example, the signal that is developed on the anode is to be calculated. A weighting potential value of unity is assigned to the electrode of interest – the anode. All other electrodes receive a value of the weighting potential of zero, including the Frisch grid. From basic electromagnetism, the electric field between two parallel electrodes kept at constant potential difference is given by

$$|E| = \frac{V}{d}. \tag{2.10}$$

where d is the cathode-anode separation. As the electron passes the grid, the charge induced on the anode will begin to increase as the electron moves closer to the anode. The maximum value the weighting potential is unity. So normalized induced potential on the electrode will increase linearly (since Equation 2.10 is linear) from zero to unity as the electron drifts between the Frisch grid and anode.

It should be noted that the region between the Frisch grid and anode is typically small. This means that the probability of an ion pair being created between the

grid and anode is much smaller than the probability of generation elsewhere in the detector. Should an interaction occur in this small region a distance x from the surface, then the signal would be at a decreased amplitude proportional to 1-x. It also means that, assuming the electrons are created in the main volume of the gas and migrate into this region, the signal induced on the anode will have the same rise time, regardless of where the ion pair was initially created. This is because the rise time would only be a function of the distance the electron travels across the distance between the grid and the anode in order to be collected. However, since the rise time is constant and not a function of the depth of interaction within the detector, it is not possible to obtain the time of interaction. This would ordinarily be done by observing the drift of the electrons through the detector, however in the case of a gridded detector, the movement of the electrons is only observed once they have passed the grid.

2.3 Single-Polarity Charge Sensing with Coplanar Anodes

A great deal of work has been done in the field of semiconductors to improve their resolution. Semiconductors such as CdZnTe and CdTe have long posed attractive detection media, however their resolutions were limited due to the poor collection of holes. While the mobility of holes is much greater than that of ions produced in a gas detector, they still suffer from trapping problems within the crystal. Without single polarity charge sensing, the movement (and thus the trapping) of holes contributes to the signal. This creates a source of fluctuation in the pulse height resulting in a loss of energy resolution.

The difficulty in making a Frisch grid for semiconductors is that it is not possible for the crystal to grow properly around the standard wire mesh used for Frisch grids. Instead, the mathematical formalism of the Schockley-Ramo theorem was applied. Through this theorem, a new type of anode design involving a coplanar anode was created for semiconductors to allow for single-polarity charge sensing. This design improves on the classic parallel plate design by making the anode, instead of a solid plate, a series of parallel interdigitized strips as illustrated in Figure

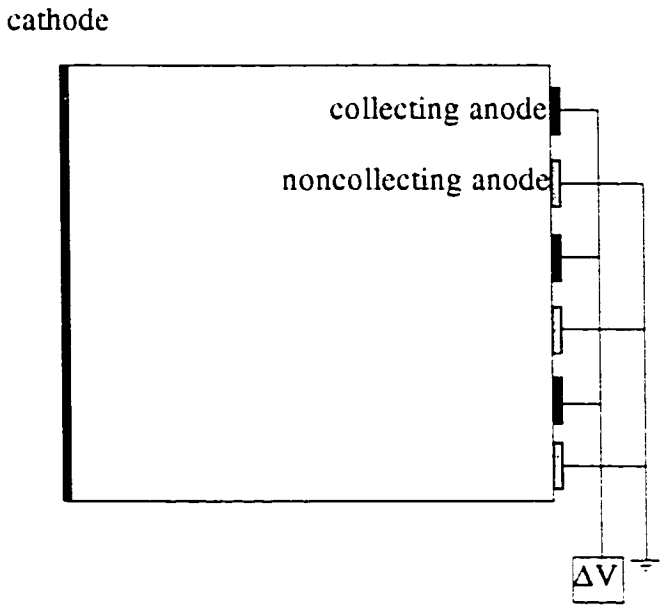

Figure 2.5: General schematic of a coplanar anode device. A potential difference, $\Delta V > 0$, is established between the collecting and non-collecting anodes.

2.5. Through the application of a potential ΔV, the collecting and non-collecting anodes are established.

In order to determine the weighting potential of the detector, the potential of the collecting anode is assigned a value of unity while setting that of the non-collecting anode and cathode to zero. There are three cases to be examined: an electron-hole pair created near the cathode surface underneath the collecting anode, an electron-hole pair created near the cathode surface underneath the non-collecting anode, and an electron-hole pair created somewhere in the middle of the detector at position ξ as shown in Figure 2.6.

In the first case (ignoring the motion of the positive charge carrier, which induces no signal since the weighting potential for the cathode is set to zero), the electron will drift toward the anode surface until it is collected by the collecting anode. The signal on the collecting anode increases to a normalized induced charge

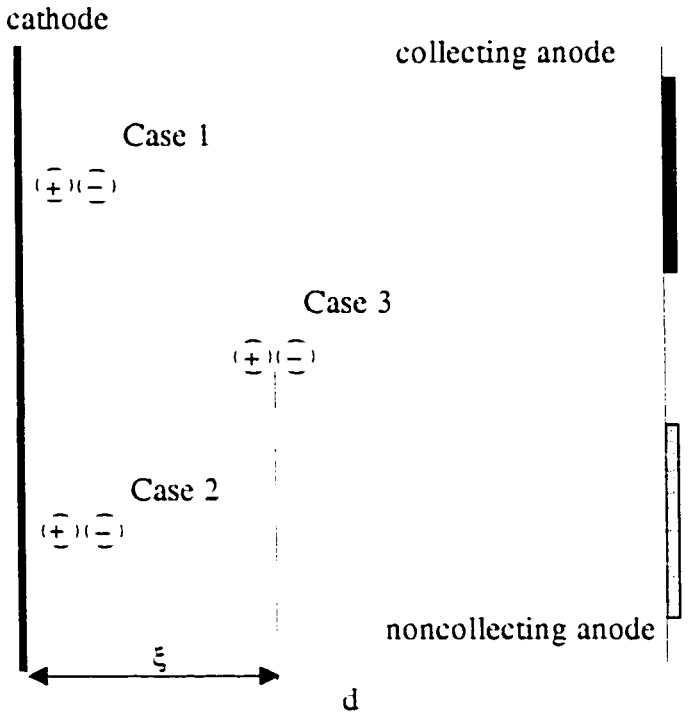

Figure 2.6: An examination of the Schockley-Ramo theorem as it applies to establishing the total normalized induced charge on each anode as a function of the location of charge carrier creation.

of unity. However, the signal on the non-collecting anode will also increase to a point. This point corresponds approximately to one pitch width below the anode surface where the normalized induced charge on the non-collecting anode returns to zero. This is because, based on the method of mirror charges, the electron and its mirror charge on the collecting anode appear to be in electrostatic neutrality relative to the non-collecting anode. This is shown in Figure 2.7.

In the second case, the electron drifts towards the anode surface similar to the first case. However, at point P, the electron moves towards the electrode at a higher potential, the collecting anode. Thus the normalized induced charge on the non-collecting anode will decrease because the electron is moving away from it while the induced signal will increase on the collecting anode as a function of decreasing proximity.

The third case demonstrates the most practical example of the charge pair being created at some arbitrary point in the detector, ξ. As in the previous two cases, the electron moves first in the direction of the anode surface and is then at P diverted towards the collecting anode. However, as shown in Figure 2.7, the induced charge on the collecting anode is 1-η. This is demonstrated by the placement of the supplemental axes in the figure at x=ξ. Additionally, the induced signal on the non-collecting anode decreases when x>P and becomes negative. This is also clear in Figure 2.7.

In order to apply these principles to the detection of the gamma rays, it is necessary to consider the difference between the two anodes. It is clear that for the first two cases, the difference in induced charge on the two anodes will always be equal to since, based on Equation 2.2, $\Delta\phi_w$ must be equal to unity. Thus the total induced charge would simply be the amount created within the detector. In other words, the difference in induced charge between the two anodes, ΔQ, is given by

$$\Delta Q = q\Delta\phi_{w,c} - q\Delta\phi_{w,nc} = q(1-\eta) - q(0-\eta) = q \tag{2.11}$$

where q is the amount of charge initially produced within the detector, $\Delta\phi_{w,c}$ is the change in the weighting potential on the collecting anode, and $\Delta\phi_{w,nc}$ is the change

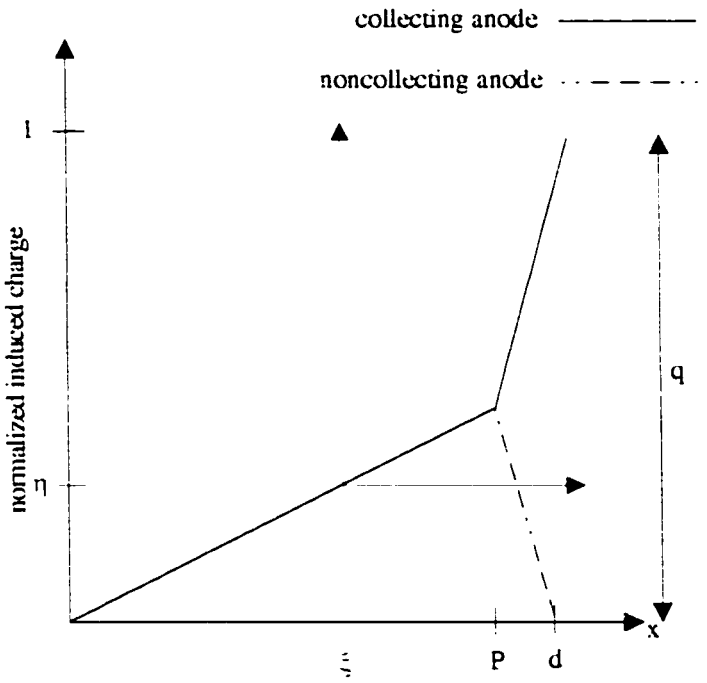

Figure 2.7: The normalized induced charge for coplanar anodes as determined by the Schockley-Ramo theorem. The first and second case are shown in black while the third case is shown in red.

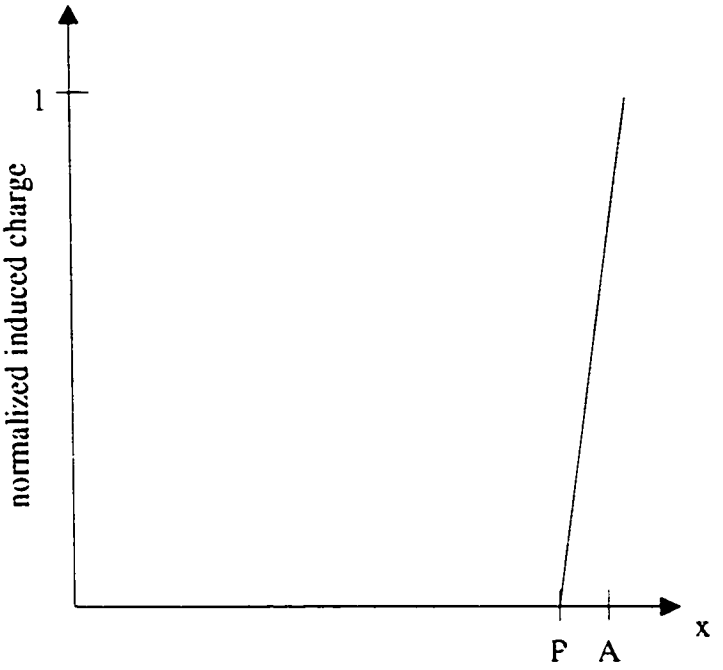

Figure 2.8: The subtracted normalized induced charge for coplanar anodes calculated by subtracting the signal of the non-collecting anode from that of the collecting anode.

in the weighting potential on the non-collecting anode. This is clearly demonstrated in Figure 2.8. By subtracting the signal of the non-collecting anode from that of the collecting anode, the resulting normalized induced charge is exactly like that of the classical Frisch grid as illustrated in Figure 2.4.

There are some important implications of Equation 2.11. First, the total induced charge is not dependent on the location that the ion pair was created. This matches well with the operation of a classical Frisch grid. The second implication is that the signal generated in this type of detector is not dependent on the movement of the ions. This is reflected by the fact, as demonstrated in Figure 2.8, that the subtracted weighting potential for the two anodes has a value of zero for the majority of the detector. So there is no change in the weighting potential as the ions move towards the cathode. Therefore, they do not contribute to the spectrum.

2.4 Problems Associated with Single-Polarity Charge Sensing

There are several potential problems associated with single-polarity charge sensing through the coplanar anode approach which can result in a worsening of the energy resolution. These include the use of insufficient potential, ΔV, between the two anodes, imbalances in the weighting potential between the anodes, and electron trapping both within the bulk of the detector and in the region within one pitch width of the anodes.

2.4.1 Insufficient Potential Between the Anodes for Coplanar Mode Operation

In order to operate in the coplanar mode, it is necessary to completely collect all of the electrons on the collecting anode. If some of the electrons are collected on the non-collecting anode, this would have the effect of having a non-zero value of the weighting potential on this electrode. As a result, the difference signal between the two anodes will be less than unity. This effect is a function of the size of the electron cloud and its location relative to the pitch of the anodes, assuming only lateral size and no charge diffusion. For example, if the electron cloud size is large relative to the pitch, there will be a significant probability that some electrons will be generated beneath the non-collecting anode and will only be drawn to the collecting anode if ΔV is sufficient. Otherwise there will be significant charge sharing between the anodes and the non-collecting anode will not reach a state of zero induced charge, as predicted by Figure 2.7. This is illustrated schematically in Figure 2.9. In this case, cloud A is created directly over the collecting anode and is small enough relative to the pitch to not be collected by the non-collecting anode. However, cloud B has some electrons that overlap the non-collecting anode. In this case, ΔV must be large enough to draw them to the collecting anode or the method of coplanar anodes will not work. As this example demonstrates, the effect of insufficient ΔV is different for each example electron cloud. For cloud A there may be no unwanted signal on the non-collecting anode, but this would not be the case for cloud B if ΔV was not high enough. Hence, this effect is a function

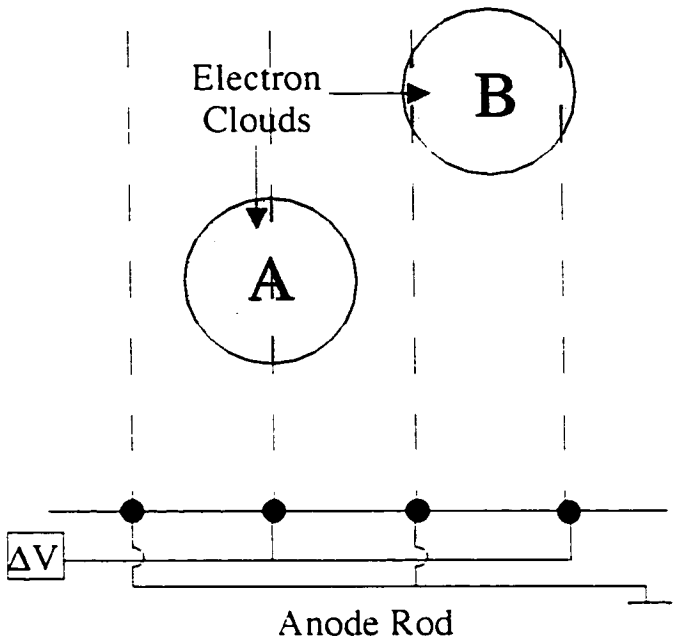

Figure 2.9: Drawing of possible electron cloud scenarios. Cloud A is created directly over the collecting anode and thus there is no charge sharing on the non-collecting anode. Cloud B is shared between both the collecting and non-collecting anodes.

of the interaction position within the detector.

2.4.2 Non-equal Gain Between the Anodes and Other Nonuniformities of the Weighting Potential

In order to obtain a weighting potential like a true Frisch grid, it is necessary that the normalized induced charge of each anode be equal in the bulk of the detector. The result is a subtracted signal with a value of zero in this region of the detector as shown in Figure 2.8. If this is not the case, there will be a non-zero component of the difference signal in the bulk. This is represented in Figure 2.10 where the collecting anode is at a slightly higher gain than the non-collecting anode by a value of Δ. (Note that this gain imbalance could also increase the normalized induced charge of the non-collecting anode.) The resulting difference signal, shown

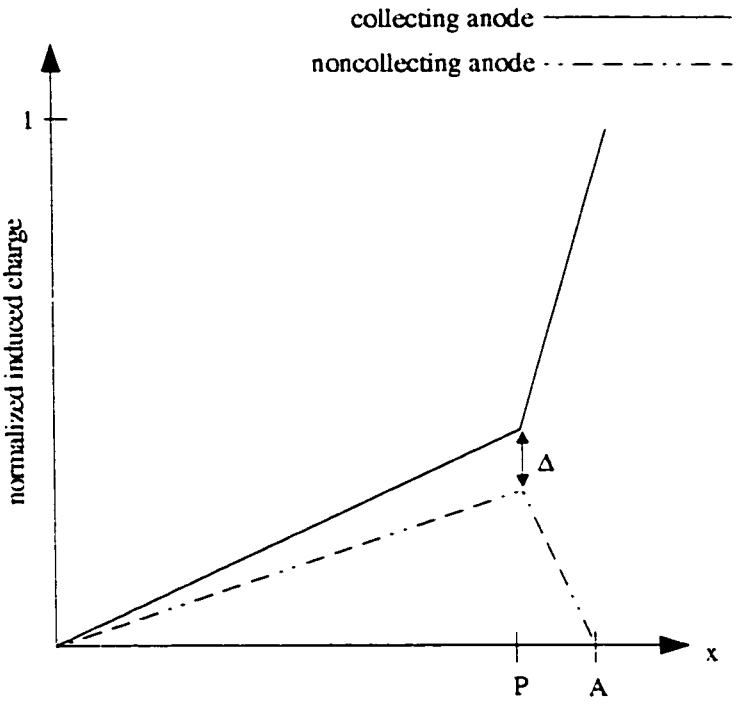

Figure 2.10: An example of the normalized induced charge on each electrode with the collecting anode at a gain that is slightly higher (Δ) than that of the non-collecting anode.

in Figure 2.11, indicates the non-zero component in the bulk with an increase of the weighting potential by the value $1+\Delta$ at the anode surface. This would have the effect of a high energy shoulder on the photopeak of the spectrum. Similarly, if the non-collecting anode was at a higher gain, the difference signal at the anode surface would be offset to a value of $1-\Delta$ resulting in a low energy shoulder on the photopeak. Additionally, since the difference signal is non-zero in the bulk, this implies that the signal on the anode is a function of position within the detector.

It is possible to create situations like those presented in Figure 2.10 through more complicated processes than simple gain differences between the anodes. For instance, suppose there was a significant difference in weighting potential between the two anodes in a particular region of the detector. This can lead to a significant degradation in the energy resolution as well as the fact that the pulse amplitude is

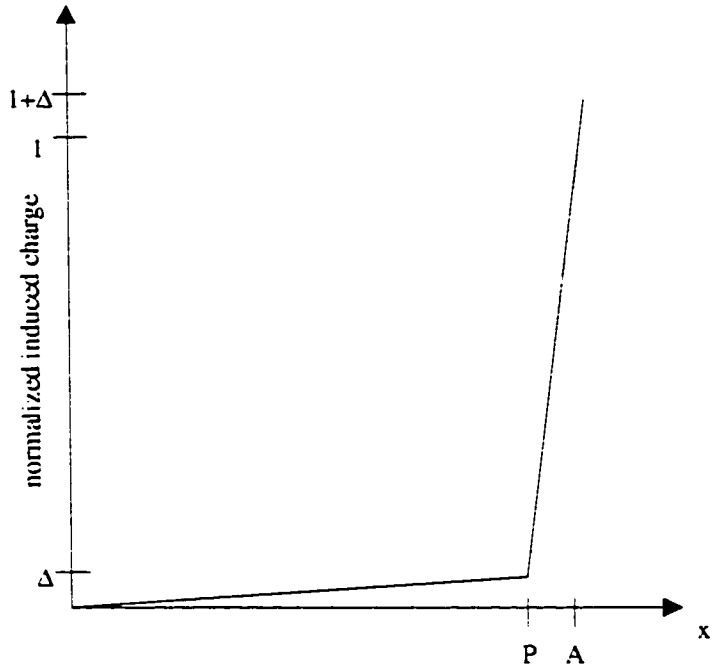

Figure 2.11: The subtracted induced charge resulting from the case where the collecting anode is at a higher gain as shown in Figure 2.10.

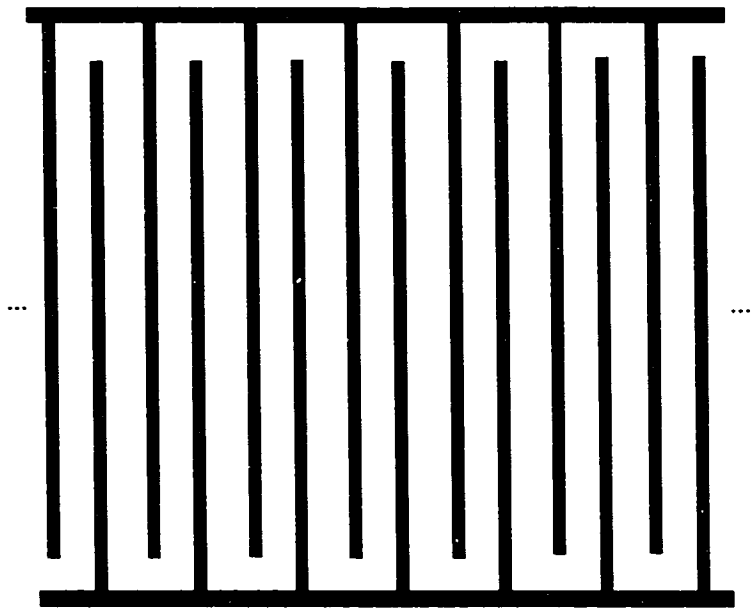

Figure 2.12: Typical coplanar anode design for semiconductors.

a function of the position of interaction within the detector.

The reason for the weighting potential nonuniformity originates in the anode design itself. When the coplanar designs were originally created for CdZnTe detectors, consideration was given as to how to best connect a series of parallel electrodes. A symmetric design was established that would allow the collecting and non-collecting anodes to be one continuous electrode as shown in Figure 2.12. Based on the symmetry of the design, one of each of the electrodes must be on the outer edge of the semiconductor. In this region, the boundary conditions will not be the same for the the two anodes. Hence, simply by the design of the coplanar anodes, a nonuniformity is introduced into the weighting field. It was found that if the weighting potential between the two anodes in this region differed by $\pm$ 20%, this would cause nearly a 40% variation in the pulse amplitude for gamma rays of equal energy. [51] Hence, attention needs to be paid to the anode design as it can significantly impact the resulting spectrum.

2.4.3 Electron Trapping

Trapping of the charge carriers in any portion of the detector will destroy the proportionality between the charge collected and the energy deposited. While the trapping may come from anywhere in the detector, the overall result is similar. Any loss of charge carriers will decrease the pulse amplitude, yielding more events in the low energy portions of the spectrum instead of in the true photopeak. However, unlike parallel plate or Frisch grid detectors, it is possible to compensate for this in a coplanar system. In the previous section, differences in gain between the two anodes were described as problematic. However, with detectors where charge trapping is a problem, it is desirable to create situations like those depicted in Figure 2.10. In this case, by placing the non-collecting anode at a lower gain relative to the collecting anode, difference signal pulses that are abnormally large will be produced thus artificially compensating for electron trapping. This can also be solved through compensation by depth sensing whereby the ratio is taken between the cathode and anode signals to determine the depth of interaction. The depth information is used to adjust the pulse amplitude of the anode to the expected value.

2.4.4 Signal Degradation due to Other Influences

There are many other possible sources of signal degradation including high detector capacitance, inductive coupling, and electric field optimization. Detectors with high capacitance can be quite noisy and effort must be made to minimize this effect. Also, some of the detectors to be presented in this work involve coiled wires around a cylindrical rod as their anode design. In this case, the possible contributions due to inductive coupling between the anodes must be considered. If the inductance is too high, a charge that is induced on the collecting anode can be inductively shared to some extent on the non-collecting anode making the difference between the two smaller than expected resulting in charge collection that is less than ideal.

2.5 Summary

In this chapter the method of coplanar anode detection has been presented. The Schockley-Ramo theorem has been introduced as a useful tool for determining the normalized induced charge on any electrode. While the use of this tool was demonstrated on the classical Frisch grid ionization chamber, additional applications were found in the field of coplanar anode design to simulate Frisch grids with semiconductors. A few of the problems associated with the use of coplanar anodes have also been discussed.

These principles will be used in the following chapters to discuss the anode designs to be used in the high pressure xenon detectors that are the focus of this work. Optimization of the anodes and detectors as a whole in terms of their weighting potentials will be considered.

Chapter 3

SIMULATIONS AND CALCULATIONS

In order to design the coplanar high pressure xenon detector, there were several calculations and simulations that were required. These fell into two categories – Monte Carlo simulations and electrostatic calculations. High pressure xenon was studied using both EGS4 and Geant4 to determine the expected spectrum for the detector and various properties such as as the expected electron cloud diameter. [77] [26] Consideration will be given to the effect of Compton scatter both within the detecting volume and any dead region of xenon. The electrostatic results to be presented were both numerical calculations and electrostatic simulations performed with the Coulomb 4.0 package. [28] The primary purpose of these electrostatic calculations is to determine the minimum required potential between the anodes for complete charge collection on the collecting anode, ΔV_{min}, and any factors that could affect this value.

3.1 Monte Carlo Simulations

In order to determine if the detectors associated with this research were functioning optimally, it was necessary to develop an understanding of what the the energy spectrum would look like. This was achieved by the use of Monte Carlo techniques using EGS4 and Geant4.

First, high pressure xenon with a density of 0.5 g/cm^3 was simulated using the PEGS package of EGS4 to determine its material properties. For example, Figure 3.1 is the calculated mean free path for photons as a function of energy. As is seen in the figure, 662 keV gamma rays will travel on average greater than 20 cm without interacting with the xenon. Additionally, the relative contribution of the

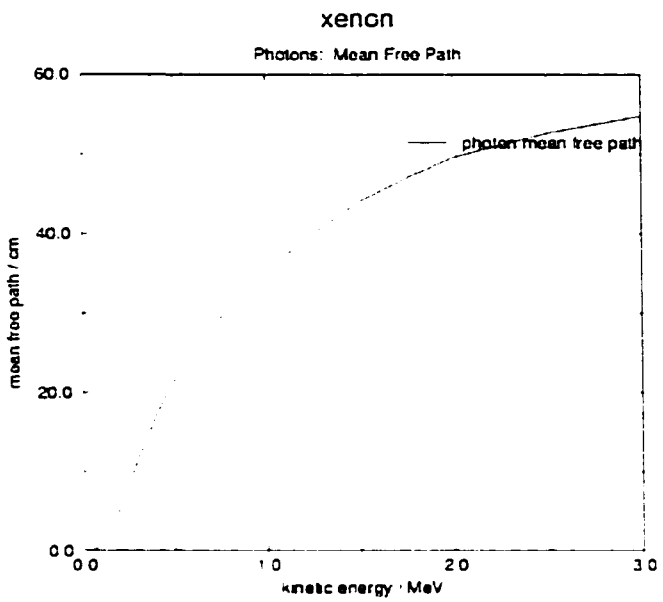

Figure 3.1: Calculated mean free path in 0.5 g/cm^3 xenon using the PEGS component of EGS4.

photoelectric effect, Compton scatter, and pair production for 0.5 g/cm^3 xenon is shown in Figure 3.2. This shows that for 662 keV gamma rays, Compton scatter will dominate the interactions with about 70% probability.

A simulation of the expected spectrum for high pressure xenon can provide a useful tool for the diagnosis of problems with the detector. For the case of a simple calculation, the spectrum is comprised of the energy deposited within the xenon. Figure 3.3 illustrates the calculated energy deposition within a 10 by 10 cm cylinder of xenon with a 1 mm thick iron cylindrical shell about the detection region to simulate the pressure vessel. The simulated detector is uniformly irradiated along its axis. This spectrum does not take into account the output of pulses resulting from this energy deposition. So neither effect of the movement of charges by an applied bias nor the measurement of those charges with coplanar anodes are considered in this calculation. To represent photopeak broadening of 2% by electronic noise, a Gaussian sampling routine has been applied to vary the energy of the incident gamma ray slightly. For the above simulation, 10^6 gamma rays were incident on

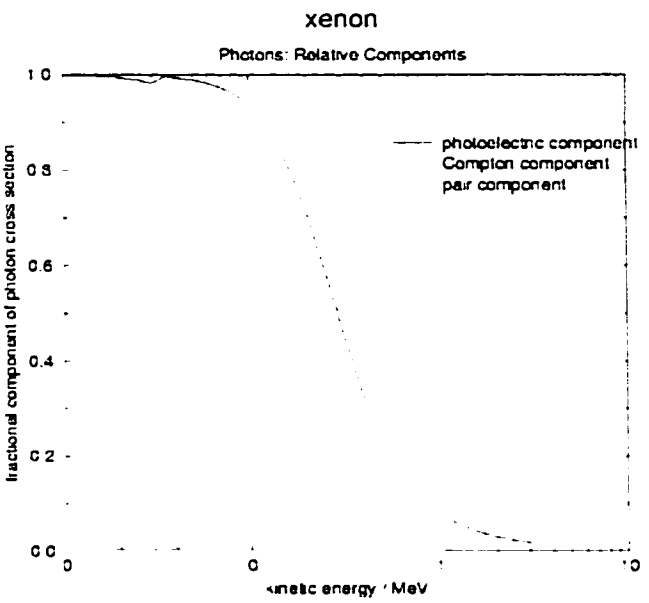

Figure 3.2: The relative probability of photoelectric effect, Compton scatter, and pair production for 0.5 g/cm^3 xenon.

the detector. Based on the above results, the photopeak efficiency was calculated to be 5.66%.

The spectrum presented in Figure 3.3 is representative of the geometry of the helical detector. However, a second detector of parallel plate geometry was also built for this work. The parallel plate detector poses some additional differences that require consideration. First, the detector has a smaller active volume, with a radius of 5 cm and a thickness of 3 cm. However, in addition to the active volume, there is a dead region of xenon that is not directly between the anode and cathode that is about 1 cm thick. This is shown schematically in Figure 3.4. It is possible that a gamma ray could undergo Compton scatter within this region and deposit the remaining energy in the active region of the detector. So a second simulation was conducted with this additional region of dead xenon surrounding the detection region. The simulated spectrum representing this second case is shown in Figure 3.5. In this case, the photopeak efficiency is 4.67%, which is expected since the active volume of the detector is less than the previous case.

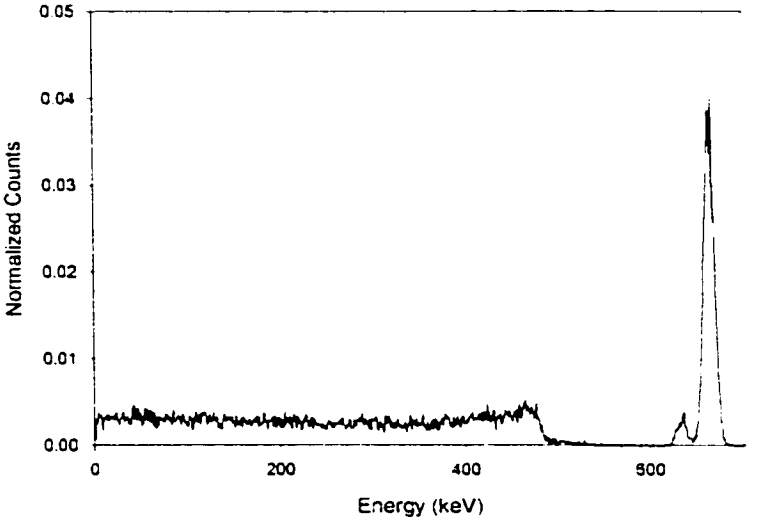

Figure 3.3: Simulated ^{137}Cs spectrum for helical detector.

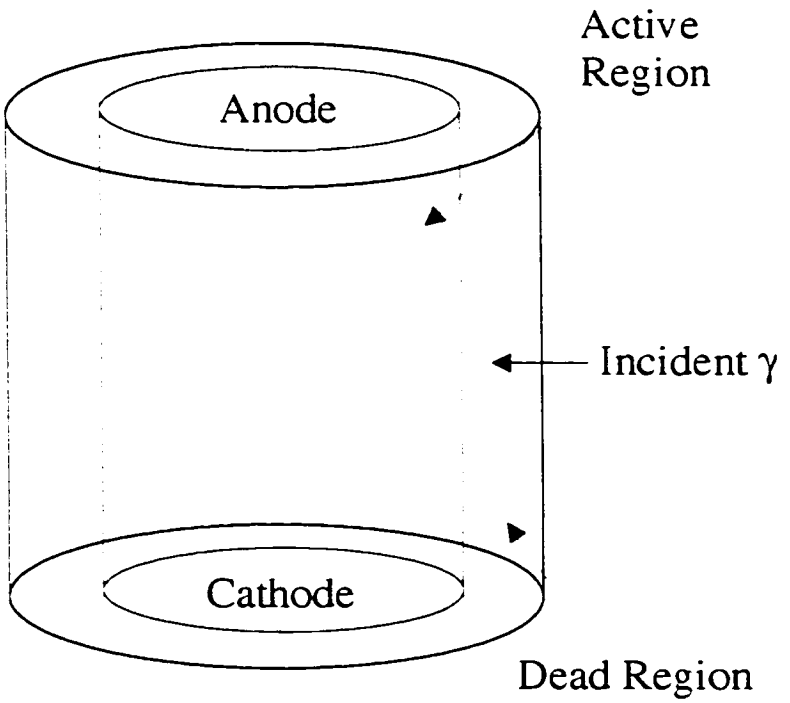

Figure 3.4: Representation of the parallel plate detector with approximately 1 cm of dead xenon surrounding the detection region.

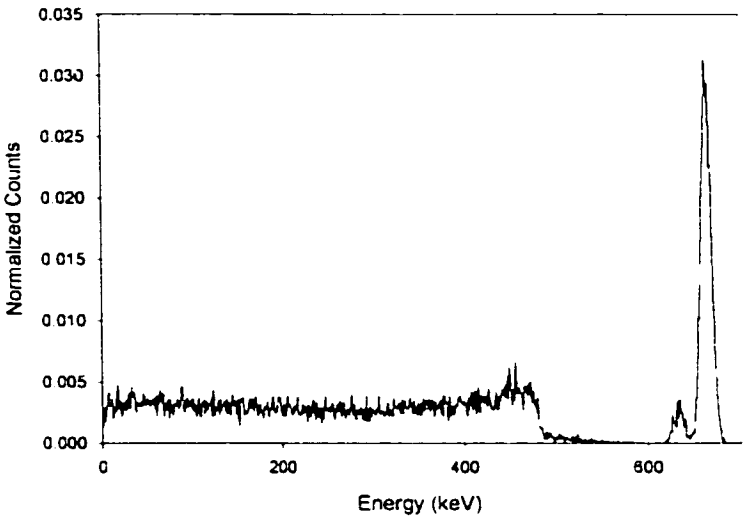

Figure 3.5: Simulated ^{137}Cs spectrum for the parallel plate detector.

3.1.1 Considerations on the Compton Continuum of High Pressure Xenon Spectra

One point worth noting is in reference to the shape of the Compton continuum in the simulated spectra. As expected, the continuum is relatively flat and featureless. However, this disagrees with prior high pressure xenon spectra and the spectra to be shown as a result of this work. [74] [15] In these spectra, the Compton continuum has an exponential shape with many more counts in the lower energy portion than the higher energy.

One possible explanation of this artifact is through a consideration of the size of these detectors, the shaping time, and the drift velocity of the electrons. High pressure xenon detectors tend to be quite large with several centimeters between the anode and cathode. If the electrons travel with a velocity of 1 mm/μs, it can take them tens of microseconds to reach the anode if they are created near the cathode. Suppose a gamma ray undergoes Compton scatter near the cathode and then a photoelectric event near the anode as depicted in Figure 3.6. These two events can be separated in time by the tens of microseconds it takes for the cathode-side event to reach the anode. If this time, Δt, is greater than the shaping time, τ, then the

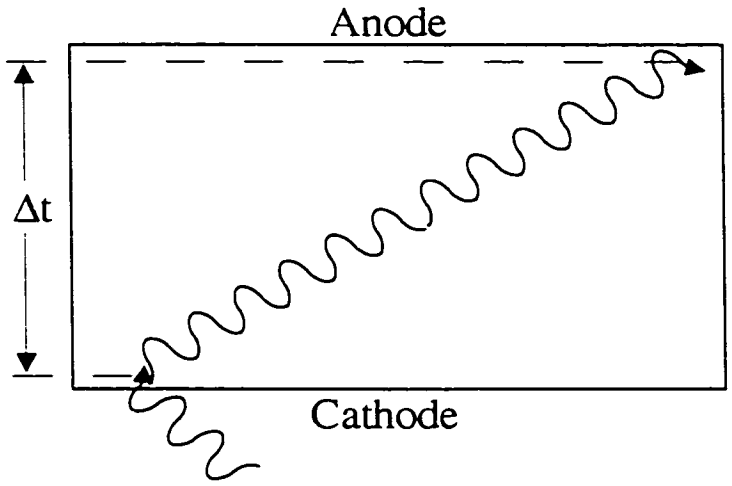

Figure 3.6: Illustration of the theorized exponential shape of the Compton continuum for high pressure xenon spectra.

two events will be treated as individual interactions with neither depositing the full gamma-ray energy. This is not reflected in the simulated spectra shown in Figures 3.3 and 3.5, which are simple calculations of the energy deposited within the gas. In practice, the contribution of this effect could be determined by observing the change in the Compton continuum as a function of τ using a shaping amplifier with a maximum shaping time greater than the maximum expected electron drift time for a given bias. However, for the high pressure xenon detectors used in this work, the maximum electron drift times were 30–50 μs. Using a shaping time this large can be detrimental to high resolution spectroscopy as there will be a great deal of noise in this long time that will be shaped into the overall pulse amplitude.

3.1.2 Electron Cloud Diameter Calculation

In addition to the energy deposited within the detector, an important parameter to consider is the size of the electron cloud within the gas. If the electron cloud diameter is large relative to the pitch of the anodes, it is then vital that the anodes be operated at a potential difference large enough to collect all of the electrons. Otherwise, strictly based on the location of the ionizing event, there is a significant probability that charges will be collected by the non-collecting anode, as previously detailed in Figure 2.9.

To determine the severity of this problem for the detectors constructed for this work, the secondary electrons created as a result of gamma-ray interactions within the xenon were studied using Geant4. In this simulation, if a gamma ray were to undergo an event creating secondary electrons, the location of each secondary is monitored relative to the original location of interaction as shown in Figure 3.7. The largest distance that a secondary electron reached relative to the starting position was recorded as the diameter of the electron cloud for that event. This diameter was then averaged over 10^6 incident gamma rays. For xenon with a density of 0.5 g/cm^3, the average initial electron cloud diameter was calculated to be approximately 3.2 mm. The detectors in this work have a 4 mm pitch with anode strip widths of 0.01 inches and 1 mm for the helical and parallel plate designs respectively. This means that, simply by considering the ratio of the calculated electron cloud diameter to the pitch and width of the anodes and neglecting the effects of electron diffusion, 100% of the events with the parallel plate detector and approximately 85% of events for the helical detector will have a portion of the electron cloud created above the non-collecting anode.

3.2 Electrostatic Simulations and Calculations

The predominant calculation required for both the helical and parallel plate detectors involved the determination of ΔV_{min}, the minimum potential difference between the two anodes such that all of the electrons would be collected by the col-

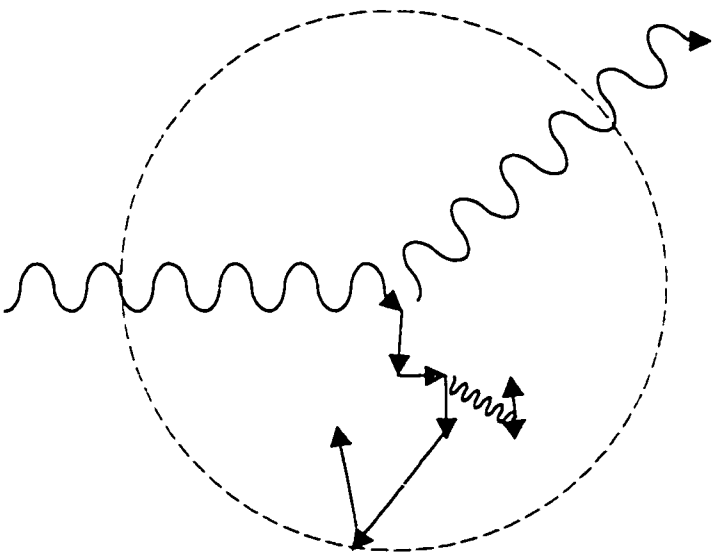

Figure 3.7: Illustration of the technique used to calculate the electron cloud diameter. In this example, the red dashed line indicates the cloud diameter to be assigned to this particular event. The sinusoidal arrows represent photons whereas the straight arrows indicate the path of a secondary electron created through various interactions.

lecting anode. The results for the helical detector, as will be described in Chapter 5, indicated a disagreement between the value of ΔV_{min} as predicted by Coulomb and the experimental results, thus motivating the work to develop an analytic solution for the potential within this detector. As a result, Coulomb was only used for creating the design of the parallel plate detector. Once this design was established, numerical methods were used to determine ΔV_{min} for this detector.

3.2.1 Coulomb 4.0 Simulation of Helical Detector

A simplified model of the helical detector was created with Coulomb 4.0. In this model, the anode wires for simplicity were modeled as conducting strips located on the cylindrical surface of the rod. In the real detector, the wires sat in a groove in the ceramic. Figure 3.8 shows the geometry used for this simulation. Once the helical detector was drawn, a cathode bias of -5 kV was applied and the potential along a line on the anode rod surface was calculated as a function of ΔV. The purpose of this calculation was to determine an approximate value for ΔV_{min} by determining the value of ΔV along this line such that there would be no local maxima in the potential near the non-collecting anode. The results of this calculation are shown in Figure 3.9. As a result of this calculation, it was determined that for the helical detector operating at a cathode bias of -5 kV, ΔV_{min} = 340 V.

3.2.2 Calculation of ΔV_{min} for the Helical Detector

Since the results of the helical detector, as will be described in Chapter 5, did not agree with the above calculated value of ΔV_{min}, an analytic solution was determined for the helical detector. Unlike previous results presented for coplanar detectors in rectangular coordinates, the solution for the cylindrical case is more complicated and a solution has not been published. [47] As is done for the solution in rectangular coordinates, a separable solution is assumed.

Beginning with the Laplace equation,

$$\nabla^2 \phi = 0 \tag{3.1}$$

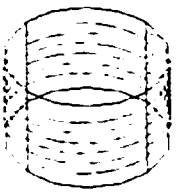

Figure 3.8: Schematic of the helical detector as simulated by Coulomb.

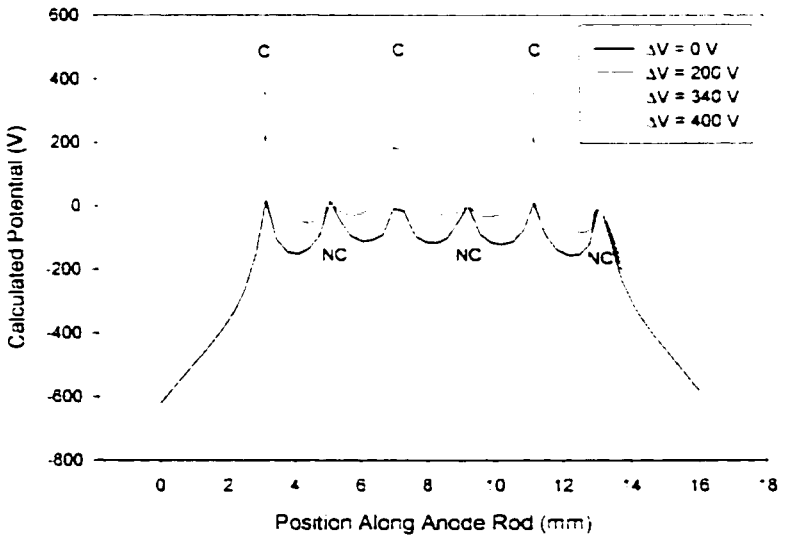

Figure 3.9: Calculated potential along the surface of the anode rod for various values of ΔV and a cathode bias of -5 kV.

where ϕ is the potential. For the sake of simplicity, the anode wires will be treated as circular resulting in angular symmetry. So the solution will have a form where $\phi = \phi(r, z)$ or

$$\phi = \phi(r, z) = R(r)Z(z) \tag{3.2}$$

where $R(r)$ is the radial component of the potential and $Z(z)$ is the axial component. In cylindrical coordinates, the Laplacian can be shown to be

$$\nabla^2 = \frac{1}{r}\frac{\partial}{\partial r}r\frac{\partial}{\partial r} + \frac{\partial^2}{\partial \theta^2} + \frac{\partial^2}{\partial z^2}. \tag{3.3}$$

Assuming angular symmetry, the second term of Equation 3.3 can be neglected and hence the Laplace equation is stated as

$$\nabla^2 V(r, z) = \frac{1}{rR(r)}\frac{\partial}{\partial r}r\frac{\partial R(r)}{\partial r} + \frac{1}{Z(z)}\frac{\partial^2 Z(z)}{\partial z^2} = 0. \tag{3.4}$$

There are two solutions to Equation 3.4, one for the case where both terms are equal to zero and the other for the first term and second terms being equal to a constant, k^2. The first solution will have the form

$$\phi(r, z) = (C_1 + C_2 \ln r)(C_3 + C_4 z) \tag{3.5}$$

while the second solution will be

$$\phi(r, z) = (C_5 J_0(kr) + C_6 Y_0(kr))(C_7 e^{ikz} + C_8 e^{-ikz}) \tag{3.6}$$

where J_0 and Y_0 are the zero-th order Bessel and Neumann functions. The complete solution will be the sum of these two solutions or

$$\phi(r, z) = (C_1 + C_2 \ln r)(C_3 + C_4 z) + (C_5 J_0(kr) + C_6 Y_0(kr))(C_7 e^{ikz} + C_8 e^{-ikz}) \tag{3.7}$$

whose constants must be determined by the application of the boundary conditions.

The boundary conditions are similar to those used in the calculation of the solution in rectangular coordinates:

1. $\frac{\partial \phi(r,z)}{\partial z}|_{r=a} = 0$

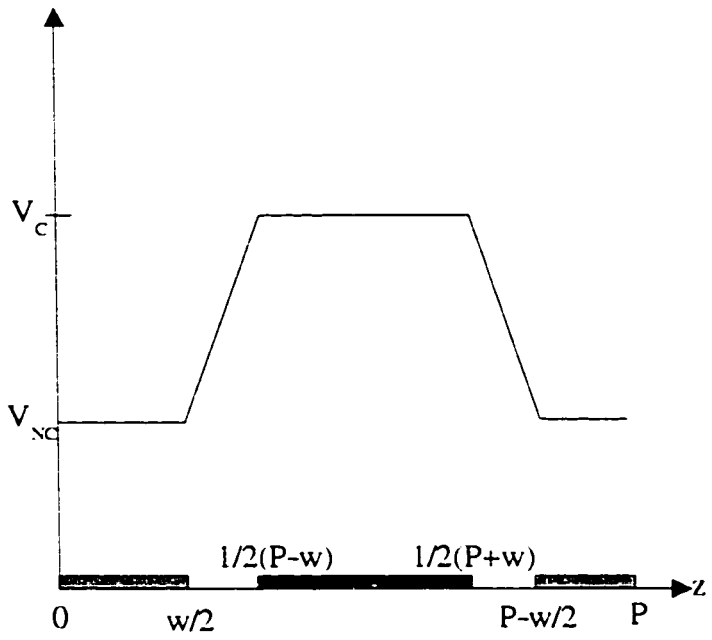

Figure 3.10: Schematic of the boundary conditions used to solve for the potential distribution within the helical detector.

2. The period along the z axis is P

3. $\phi(b, z) = 0$

4. $\phi(a, z) = \phi_a(z)$

where a is the anode radius and b is the cathode radius. The final boundary condition represents the fact that the potential will be periodic along the surface of the anode, given by some function, $\phi_a(z)$. In reality, this function is quite complex, but is shown in Figure 3.10.

Through extensive calculation, the potential can be solved for the boundary conditions to obtain

$$\phi(r,z) = \frac{V_C + V_{NC}}{2}\frac{\ln\frac{b}{a}}{\ln\frac{b}{a}} + \frac{4(V_C+V_{NC})}{\pi^2(2\frac{w}{P}-1)}\sum_{n=1}^{\infty}\frac{\cos\frac{n\pi w}{P}}{n^2}\cos(\frac{2n\pi}{P}z)\frac{\frac{J_0(\frac{2n\pi}{P}b)Y_0(\frac{2n\pi}{P}r)}{Y_0(\frac{2n\pi}{P}b)} - J_0(\frac{2n\pi}{P}r)}{\frac{J_0(\frac{2n\pi}{P}b)Y_0(\frac{2n\pi}{P}a)}{Y_0(\frac{2n\pi}{P}b)} - J_0(\frac{2n\pi}{P}a)} \tag{3.8}$$

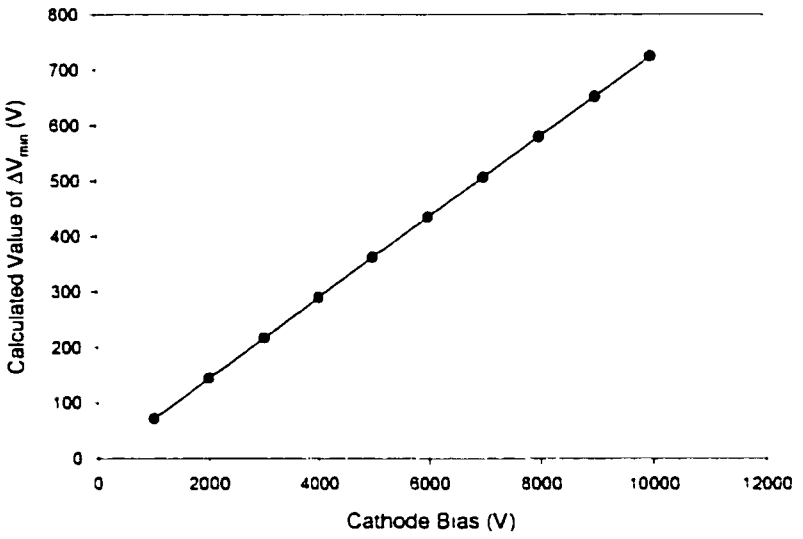

Figure 3.11: Calculated value of ΔV_{min} as a function of cathode bias for the helical detector.

where w is the width of the anode. If the Bessel functions are expanded for large x, the final solution is approximated to be

$$V_C = V_{NC}\left[\frac{-\frac{1}{2\ln(\frac{a}{b})} + \frac{8}{\pi(2w-P)}\sum_{n=1}^{\infty}\frac{\cos(\frac{n\pi w}{P})}{n}\frac{(1+\frac{3P}{16\pi na})}{(1-\frac{P}{16\pi na})}}{\frac{8}{\pi(2w-P)}\sum_{n=1}^{\infty}\frac{\cos(\frac{n\pi w}{P})}{n}\frac{(1+\frac{3P}{16\pi na})}{(1-\frac{P}{16\pi na})}\frac{1}{2\ln\frac{a}{b}}}\right], n = 1, 3, 5, \ldots \quad (3.9)$$

A code was written using Matlab to determine for a given value of V_C the necessary value of V_{NC} to have a slope of zero directly beneath the non-collecting anode. So if this value of ΔV_{min} is determined for a given cathode bias, any value of ΔV greater than this should result in complete collection of the electrons by the collecting anode. The results of the calculation of ΔV_{min} as a function of cathode bias are shown in Figure 3.11 with an example of the critical case demonstrated in Figures 3.12 and 3.13.

3.2.3 Simulation of the Parallel Plate Detector

The majority of the electrostatic simulations performed on the parallel plate detector involved the optimization of the coplanar anode design, which will be discussed in detail in Chapter 4. However, the analytic solution for ΔV_{min} was solved

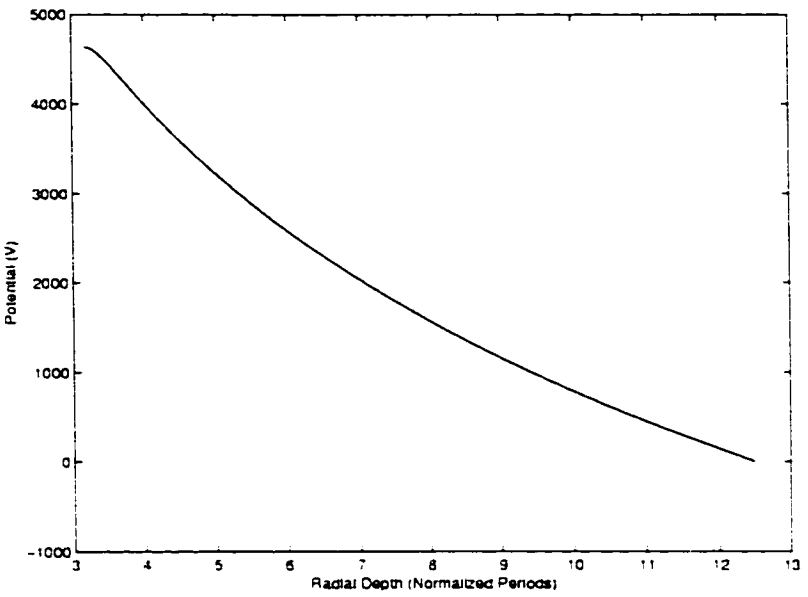

Figure 3.12: Calculated potential of the helical detector as a function of distance directly beneath the non-collecting anode for the case where $\Delta V = \Delta V_{min}$.

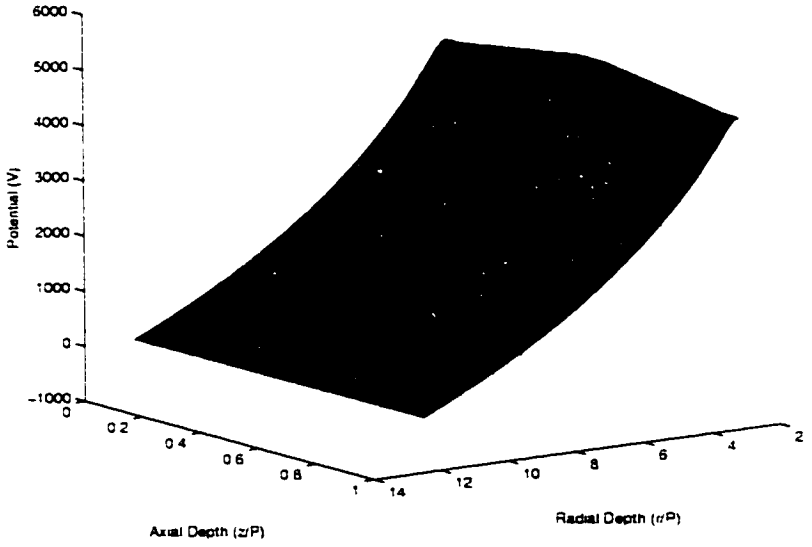

Figure 3.13: Calculated three-dimensional potential of the helical detector for the case where $\Delta V = \Delta V_{min}$ for one pitch (4 mm) of the detector.

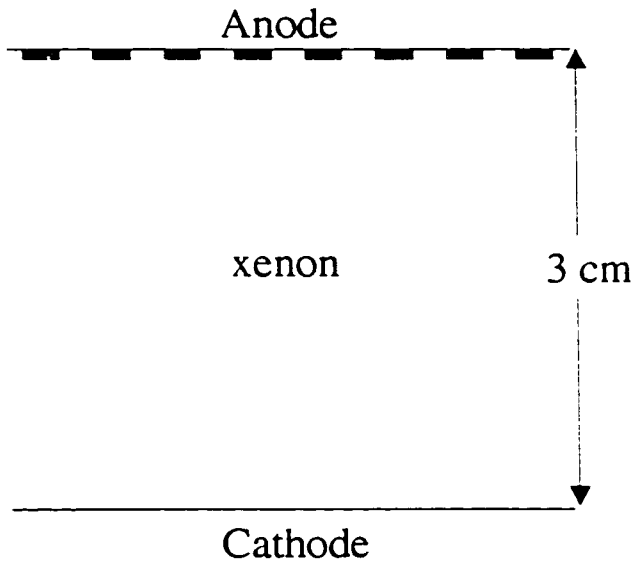

Figure 3.14: Schematic of the parallel plate detector used for the calculation of ΔV_{min}.

for this detector based on previously reported derivations and so the derivation will only be highlighted here. [47] [49] These calculations were performed for a 4 mm pitch detector with 1 mm strip and gap widths and a 3 cm cathode separation as shown in Figure 3.14.

As with the helical detector, the solution of ΔV_{min} involves solving the Laplace equation for the potential, $\phi(x, y)$, and then calculating the value of ΔV where the slope of the potential equals zero at the non-collecting anode surface. If the potential is assumed to solve the Laplace equation

$$\nabla^2 \phi(x, y) = 0 \tag{3.10}$$

and the following boundary conditions are assumed

1. $\frac{\partial \phi(x,y)}{\partial x}|_{x=0} = 0$

2. The period along the x-axis is P

3. $\phi(x,0) = 0$

4. $\phi(x,D) = \phi_D(x)$

where D is the detector thickness, then it has been shown that the solution to the Laplace equation is given by [47]

$$\phi(x,y) = a_0\frac{y}{D} + \sum_{n=1}^{\infty} a_n \cos\frac{2\pi n}{P}x\left(\frac{\sinh\frac{2\pi n}{P}y}{\sinh\frac{2\pi n}{P}D}\right) \tag{3.11}$$

where

$$a_0 = \frac{1}{P}\int_0^P \phi_D(x)dx \tag{3.12}$$

and

$$a_n = \frac{2}{P}\int_0^P \phi_D(x)\cos(\frac{2\pi n}{P}x)dx. \tag{3.13}$$

For the case where the pitch is much smaller than the detector thickness, Equation 3.11 can be approximated as

$$\phi(x,y) \approx a_0\frac{y}{D} + \sum_{n=1}^{\infty} a_n \cos(\frac{2\pi n}{P}x)e^{-2\pi n\frac{D-y}{P}}. \tag{3.14}$$

By taking the derivative of Equation 3.14, ΔV_{min} is solved for as the case when the derivative is zero at the surface of the non-collecting anode. [49] The solution is

$$V_{NC} = \left[\frac{\frac{8D}{\pi(P-2w)}\ln(\cot\frac{\pi w}{2P}) - 1}{\frac{8D}{\pi(P-2w)}\ln(\cot\frac{\pi w}{2P}) + 1}\right]V_C \tag{3.15}$$

where w is the width of the anode strip and

$$\Delta V = V_C - V_{NC}. \tag{3.16}$$

Based on these equations, ΔV_{min} was calculated for several biases for the parallel plate detector. These results are shown in Figure 3.15. Hence, for a cathode bias of -6 kV resulting in the desired electric field of 2 kV/cm, a potential difference between the anodes of 348 V is required for coplanar mode operation.

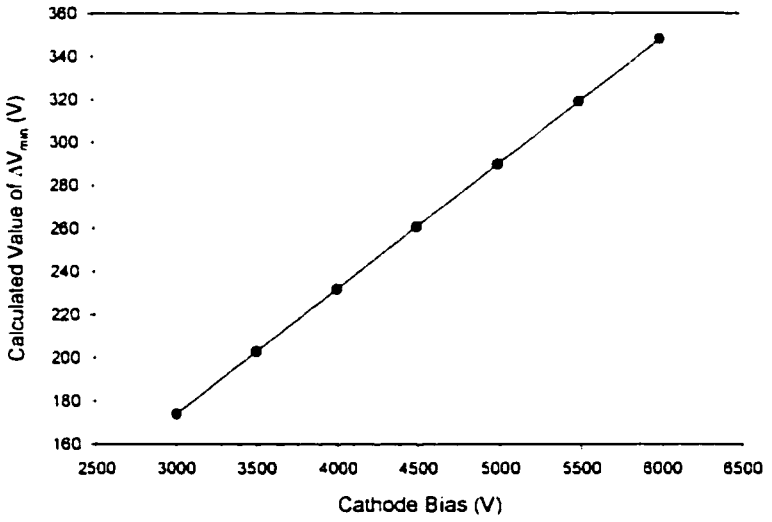

Figure 3.15: Calculated value of ΔV_{min} as a function of cathode bias for the parallel plate detector.

Chapter 4

DESIGN

As described in previous chapters, a coplanar high pressure xenon detector was constructed of a cylindrical geometry. This detector consists of two wires helically wound about a central anode rod made of Macor ceramic. As will be detailed in the following chapters, this detector exhibited strange results that initially could not be explained. As a result, a second detector was designed and constructed involving a planar configuration in order to simplify the electric fields within the detector. In addition, this design would eliminate the possible contributions due to magnetic inductance from the coiled anodes of the helical detector. Each design will be discussed here as well as the electrostatic simulation results of each.

4.1 The Helical Design

Of the detectors built for this work, the helical detector was built first. Its design poses a simple solution to the problem of creating a cylindrical coplanar anode detector. However, the design of a coplanar high pressure xenon detector poses a problem uncommon to semiconductor coplanar detectors. For a semiconductor, the electrodes are photodeposited directly to the surface of the detecting medium and all connections are made on the back of the electrodes. The means that the wires that carry any bias or charge are not within the detecting region of the detector resulting in distorted fields. However, with a gas detector, it is necessary to provide some sort of support mechanism for the anodes. So consideration was required in the design in order to eliminate the need for connection wires within the gas that would distort the field.

As a result, a design was developed to create a simple coplanar detector using

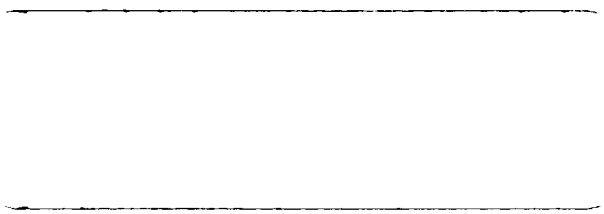

Figure 4.1: Drawing of anode configuration of the helical detector. The solid and dashed lines represent two different wires wound about the ceramic core comprising the collecting and non-collecting anodes. The pitch of the wires is 4 mm.

two wires helically wound about a central Macor ceramic rod that is one inch in diameter and 10 cm long as shown in Figure 4.1. The anode rod was placed in a pressure vessel with cylindrical shell and endcaps comprised of Macor. The cathode is made of a cylindrical shell lined with a silver foil. The wires for the cathode bias as well as the two anode wires connect to Kings Electronics 5kV high pressure bulkhead connectors. A complete schematic of the detector is shown in Figure 4.2.

The strongest influence to the design was electronic noise considerations. Many high pressure xenon detectors have reported higher than acceptable values for capacitance, which increases the electronic noise. Hence, the detector was designed to minimize the contribution of detector capacitance on the overall electronic noise while maximizing the detector efficiency.

The result is a detector with a pitch of 4 mm. It was calculated via electrostatic simulation with the Coulomb 4.0 package that this pitch width resulted in a capacitance between the anodes of less than 50 pF while also not requiring a very high potential between the two anodes to ensure complete charge collection on the collecting anode. Macor was chosen for the core due to its excellent properties as an insulator (Macor has a bulk resistivity of $10^{17}\Omega$·cm), thus minimizing the leakage current between the anodes. Additionally, Macor is commonly used with high

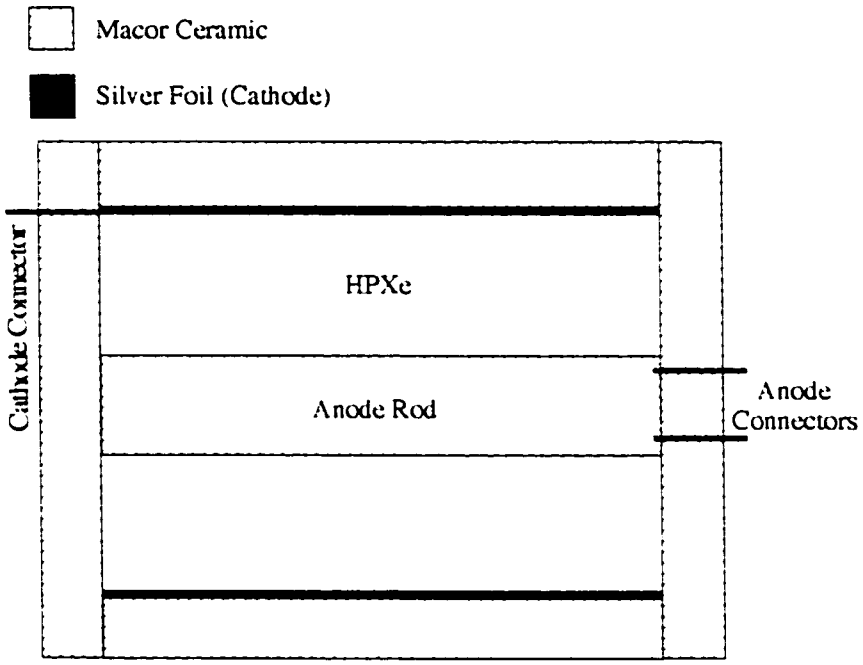

Figure 4.2: Schematic of the complete helical detector. The outer walls of the pressure vessel (not shown) are made of stainless steel.

pressure xenon detectors due to its minimal outgassing to prevent contamination of the xenon.

4.1.1 Electric Field Considerations

In order to design a detector for coplanar mode operation, it is also necessary to consider the electric field within the detector. Before construction, it is necessary to know if it is possible to attain the required value of ΔV for complete charge collection on the collecting anode.

The formalism in Chapter 3 developed a solution for the required ΔV as a function of cathode bias:

$$V_C = V_{NC}\left[\frac{-\frac{1}{2\ln(\frac{a}{b})} + \frac{8}{\pi(2w-P)}\sum_{n=1}^{\infty}\frac{\cos(\frac{n\pi w}{P})}{n}\frac{(1+\frac{3P}{16\pi na})}{(1-\frac{P}{16\pi na})}}{\frac{8}{\pi(2w-P)}\sum_{n=1}^{\infty}\frac{\cos(\frac{n\pi w}{P})}{n}\frac{(1+\frac{3P}{16\pi na})}{(1-\frac{P}{16\pi na})}\frac{1}{2\ln\frac{a}{b}}}\right] \tag{4.1}$$

where V_C is the critical bias of the collecting anode, V_{NC} is the bias of the non-collecting anode, P is the pitch, w is the anode width, a is the anode radius, and b is the cathode radius. For a cathode bias of -5 kV, the critical potential difference, ΔV_{min}, was determined to be 362.6 V. It is also important to develop an understanding for the weighting potential within the detector. The weighting potential is calculated by applying 1000 V to the collecting anode with 0 V applied to both the cathode and non-collecting anode. The results of this calculation can be seen in Figure 4.3.

4.2 The Planar Detector

As previously discussed, the planar detector was built to simplify the design and to be used as a "proof-of-principles" detector. The first consideration made was for the pressure vessel of this detector. It is easier to construct a pressure vessel in a cylindrical shape as this minimizes the stresses on the joints of the vessel. It was decided that a previously-constructed vessel of cylindrical geometry would be used temporarily and, should the principle of coplanar operation be demonstrated,

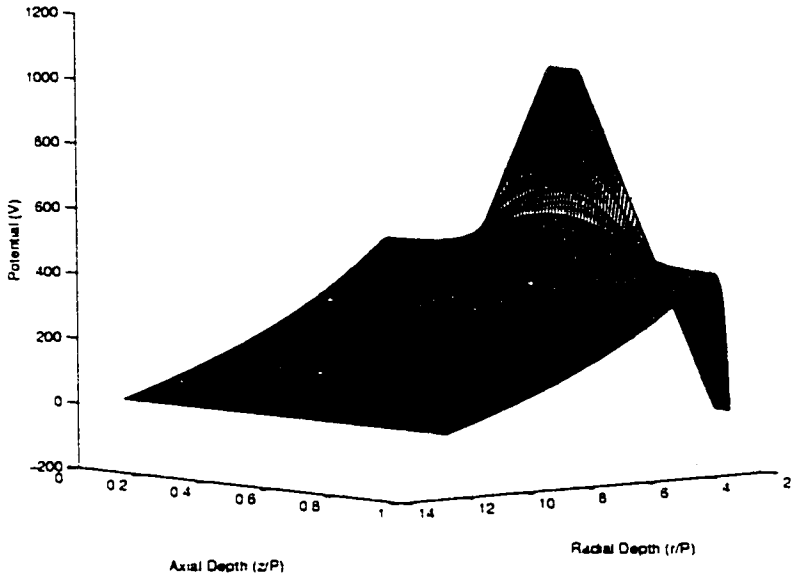

Figure 4.3: Calculated weighting potential for the helical detector.

a more permanent housing could be constructed in the future. The pressure vessel used for this detector is described in [98].

Additional considerations were placed on the cathode to anode separation. Previous results have shown that an electric field greater than or equal to 2 kV/cm is required for high pressure xenon detectors in order to minimize the probability of electron trapping within the drift field. [65] As such, it was decided that the separation between the cathode and anode would be 3 cm. With a cathode bias of -6 kV, this would adequately provide the necessary electric field.

The final design consideration involved the anode itself. In order to minimize the region of dead space around the anode in a cylindrical pressure vessel, a circular pattern was required. There are several ways that this could be achieved. First, a series of rings could be made with many wires connecting them on the back side of the surface. Another possibility is to make two interdigitized spiral patterns to achieve the same result. The later was the decided pattern since it would require the least number of wires floated behind the anode surface. This reduced problems in anode construction while also minimizing the possible contributions

to the electric field and capacitance of these wires.

4.2.1 Balancing the Weighting Field

Considerable attention to the design of the anode pattern was required in order to minimize the difference in weighting potentials between the two anodes. The difference between weighting potentials of the two anodes needs to be as small as possible across the entire detector. This is because, as previously stated, any difference in the weighting potential will result in a difference in the measured induced charge, which would create a variation in the measured total energy deposited. The outcome of such variation would be a fluctuation in the position of the photopeak and an overall loss of energy resolution. [51]

In the work on CdZnTe coplanar anode detectors, it was discovered that a balanced weighting function resulted from a detector with varying strip widths on the outer portion of the detector, referred to in the literature as the "generation 3 design." [51] Hence, it was decided that the high pressure xenon spiral anode should follow similar behavior. To maintain design similarity with the helical detector, the pitch of the parallel plate detector was chosen to be 4 mm. A peripheral electrode was added to the boundary of the anode structure to further balance the weighting field. A sample of the spiral pattern can be seen in Figure 4.4.

Simulations of the anode grid pattern were conducted using Coulomb 4.0. The width of the outer portion of the anode strips was varied and the resulting weighting potentials were examined for several strip widths. This was done by applying a bias of 1000 V to the anode whose weighting potential was to be calculated and the other electrodes received a bias of 0 V. The weighting potentials were examined along a line located at one pitch width (4 mm) below the anode surface where the difference in weighting functions between the two anodes most dramatically affects the spectra. Figure 4.5 shows the data for the case where the width of the thick portion of the anode is 1.5 mm and that of the thin anode is 0.75 mm.

In order to ascertain the ideal anode dimensions, it was necessary to examine the difference in weighting potentials between the two anodes for a variety of ra-

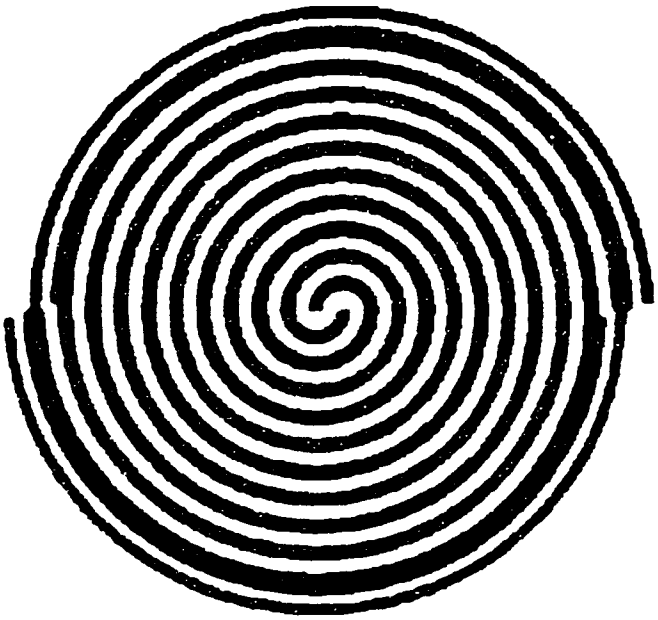

Figure 4.4: Spiral pattern used for the planar HPXe detector. The inner electrode strip and gap widths are 1 mm creating a total pitch of 4 mm. The "y direction" is considered to be in the vertical direction.

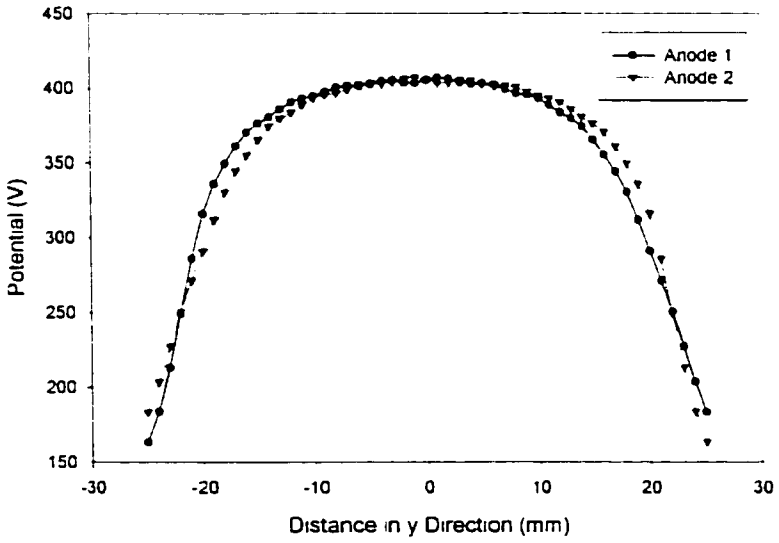

Figure 4.5: The calculated potential 4 mm below the anode surface along a vertical line through the center of Figure 4.4 with 1000 V applied to the anode of interest.

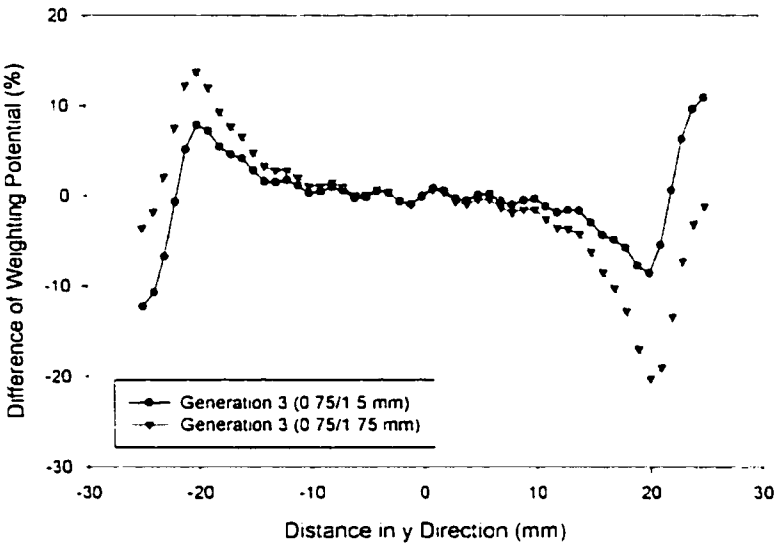

Figure 4.6: The calculated difference in weighting potential expressed in percentage between the two ideal anode designs.

tios between the thick and thin strips. By this analysis, it was determined that the two optimal values, expressed as a ratio of narrow to wide strip thicknesses, were 0.75/1.5 mm and 0.75/1.75 mm. The difference in weighting potential for these two cases can be seen in Figure 4.6.

While it appears from initial inspection that the ratio of 0.75/1.5 mm yields the smallest difference in weighting potential, it is also important to consider these variations as a function of area of the anode surface. Hence, the results presented in Figure 4.6 were weighted as a function of anode area by

$$\sigma^2 = \sum \frac{\pi(r_i^2 - r_{i-1}^2)}{\pi(r_{total}^2)} \cdot (\Delta\phi_w)_i^2 \tag{4.2}$$

where σ is the area-weighted difference in weighting potential, r_{total} is the total area of the anode surface, and $\Delta\phi_w$ is the calculated difference in weighting potential at the given radius. Based on the results demonstrated in Table 4.1, it was decided that the ratio of 0.75/1.5 mm was optimal.

The anode structure was initially made by depositing a thin layer of gold onto an alumina (Al_2O_3) ceramic with copper wires brazed to the surface for the three electrode connections.

Table 4.1: Comparison of area-weighted difference in weighting potential

Thickness Ratio (mm)	σ (%)
0.75/1.5	8.41
0.75/1.75	12.40

4.2.2 Calculated Values for the Minimum Potential Difference Required for Complete Charge Collection

As previously stated, the drift electric field should be at least 2 kV/cm in order to minimize the probability of electron trapping within the bulk of the gas. It is also necessary to determine the minimum required potential difference between the two anodes for the planar detector for complete charge collection on the collecting anode. Unlike the case with the helical detector, it is much easier to solve this problem for the planar detector. If the anode surface is approximated as an infinite surface with parallel anode strips, it has been shown that the minimum potential difference, ΔV_{min}, can be calculated using Equation 4.1. It was found that ΔV_{min} = 348 V when the cathode bias is -6 kV or $\Delta V_{min} = 232V$ when the cathode bias is -4 kV.

4.3 Preparation of the HPXe Fill Gas

In addition to the electrical requirements on the anode structure, there is also significant emphasis that must be placed on the xenon itself. "Research grade" xenon is not sufficiently pure for use in high pressure xenon spectrometers, requiring several phases of purification to meet this requirement. Most purification techniques involve spark chamber purification, the use of an oxisorb, and a high temperature getter, or some combination of all of these. For the xenon used in this experiment, the gas was sparked in a titanium spark purifier for approximately three days before being introduced to the pressure vessel.

Prior to the release of the xenon from the spark chamber, it is necessary to remove all of the air from the regions of the fill station where the xenon will pass. This is done first by establishing a preliminary vacuum with a roughing pump

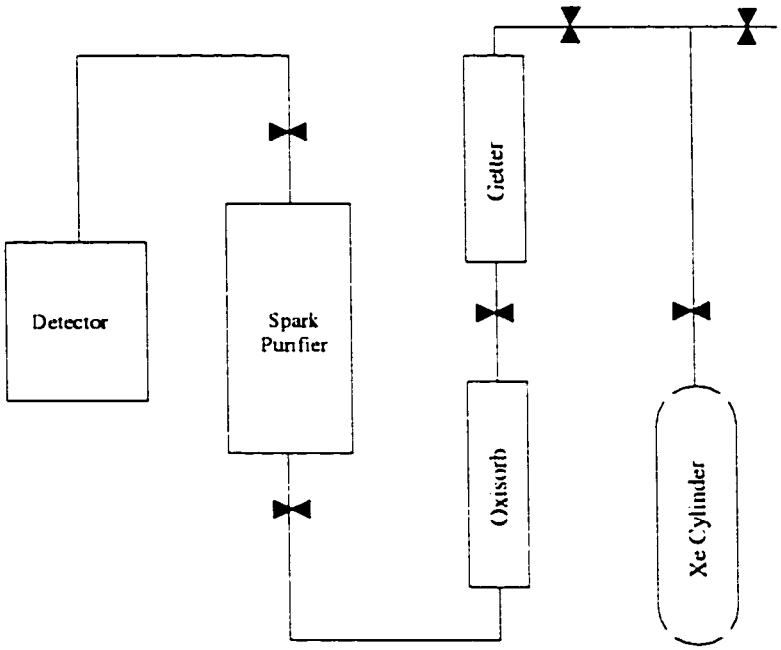

Figure 4.7: Schematic of the gas purification system used for the xenon in this work.

and then further decreasing the pressure with a turbo pump. Once a pressure of approximately 10^{-7} Torr is achieved, the pressure vessel and all fill station components exposed to air are heated to 200 °C. This temperature is sufficiently high to prevent the water vapor from adsorbing onto any metal within the system. By baking these parts at this temperature for three days, the water is evaporated and removed from the system. Once the bake is completed, the xenon can be introduced into the pressure vessel without fear of contamination. Based on the isotherms presented in [74], a pressure of approximately 750 psi at room temperature was introduced into the vessel to provide a density of approximately 0.5 g/cm^3.

Chapter 5

RESULTS AND ANALYSIS OF THE HELICAL DETECTOR

Two helical detectors were initially of identical design with a volume of 735 cm^3. The two detectors, made of stainless steel pressure vessels, were filled to densities of 0.4 and 0.6 g/cm^3. However, while the second detector was being completed, an important discovery was made about the anode wire size that will be described later in this chapter. As a result, the first detector received replacement anode wires of a larger diameter before the completion of the second detector. The second helical detector has the original wires for the anodes and thus was not used for extensive experimentation. The following sections describe the experiments performed either to obtain the initial results of each detector or to diagnose the problems with the detectors.

5.1 Initial Results

The helical detector was initially connected and charge pulses were observed from the AmpTek A250 charge-sensitive preamplifiers at a cathode bias of -5 kV with no potential difference between the two anodes. Pulses of 3–5 mV were observed, most of them shared between both anodes. This indicated that the xenon was pure enough to conduct the experiments.

Based on the calculations presented in Chapter 4, the minimum potential difference of approximately 363 V was expected in order to ensure complete collection of the electrons on the collecting anode. Once it was verified that the gas was sufficiently pure, ΔV was increased in small increments and the spectrum was observed as a function of this increase. However, at the calculated anode potential

difference of ΔV = 363 V, the pulses did not appear to be coplanar. For a detector operating in coplanar mode, there should be an initial increase in the signal on both anodes corresponding to electrons moving in the bulk of the detector. When they move away from the non-collecting anode towards the collecting anode, the signal on the non-collecting anode should become of opposite polarity to the collecting anode, as demonstrated by the weighting potential shown in Figure 2.7. However, at ΔV = 363 V, the pulses on the non-collecting anode looked identical to the collecting anode. This suggests that ΔV was not large enough to collect all of the electrons on the collecting anode, thus not achieving coplanar mode operation. Even at ΔV = 800 V, coplanar mode operation had not been achieved – even at this bias of more than twice ΔV_{min}, there were still pulses on the non-collecting anode of the same polarity as the collecting anode. Sample pulse waveforms are shown in Figure 5.1 where the output of the collecting anode is in yellow, that of the non-collecting anode is in green, the subtraction signal is in purple, and the shaping amplifier output is in pink. As a result, ΔV was further increased in order to observe the changes in the spectrum. Even at ΔV = 1500 V, there was no photopeak observed in the difference signal nor had the pulses started to appear to be coplanar. Additionally, no clear photopeak was evident in the spectra, as shown in Figure 5.2.

Since coplanar mode operation had not been achieved at such high values of ΔV, the cathode bias was decreased by 40% to -3 kV so it would be possible to run with a lower ΔV to collect the electrons without sparking. For a cathode bias of -3 kV, the minimum potential was calculated to be ΔV_{min} = 217.6 V. At this bias setting, ΔV was again increased while observing the results on the spectra. When ΔV = 600 V, a photopeak became evident in the spectrum, which became a clear photopeak at ΔV = 900 V. Spectra were taken for both the collecting anode and the output of the subtraction circuit as shown in Figure 5.3. Is it evident from the figure that the pulses from the subtraction circuit were larger than those of the collecting anode, as shown by an increase in channel number of the photopeak. This indicates that the pulses on the non-collecting anode were opposite in polarity of the

Figure 5.1: Sample pulses obtained with cathode bias of -5 kV and ΔV = 800 V on a time scale of 200 μs/division.

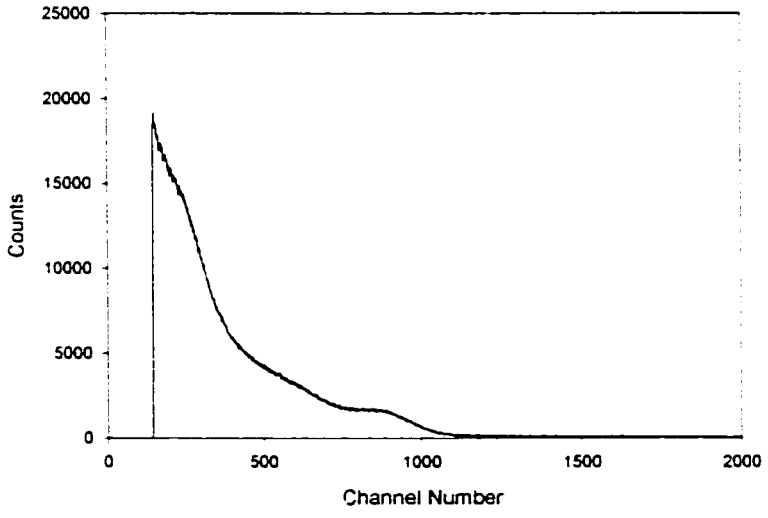

Figure 5.2: ^{137}Cs spectrum for the helical detector with a cathode bias of -5 kV and ΔV = 1500 V.

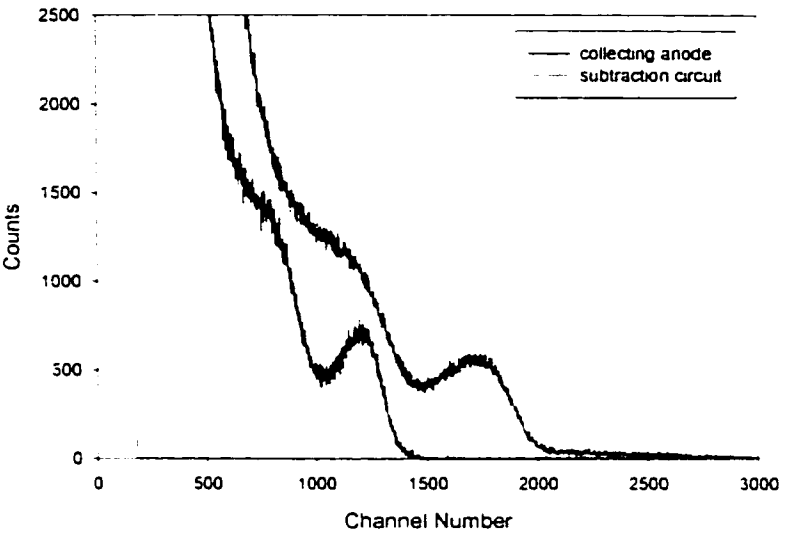

Figure 5.3: Initial spectra from the collecting anode and subtraction circuit for ^{137}Cs with ΔV = 900 V and a cathode bias of -3 kV.

collecting anode, at least some of the time. However, when the pulse waveforms of the two anode were observed on the oscilloscope, only about 10% of the pulses on the non-collecting anode were, in fact, of opposite polarity and these tended to be very small in amplitude. The remaining 90% of the pulses were of the same polarity or pulses on the collecting anode. So while a photopeak was visible at ΔV = 900 V, the collecting anode was still not collecting all of the electrons. As ΔV was increased to even higher values, there was no improvement in the photopeak of the spectrum.

Based on the initial spectra and the observations made on the pulse waveforms of the non-collecting anode, it was clear that there was a problem collecting all of the electrons on the collecting anode. The design of the anode rod was considered as one possible means of failure.

5.2 Anode Wire Replacement

The anode rod itself was machined out of Macor ceramic with a bulk resistivity of $10^{17}\Omega$·cm. During the machining process, a groove was cut into the ceramic to hold

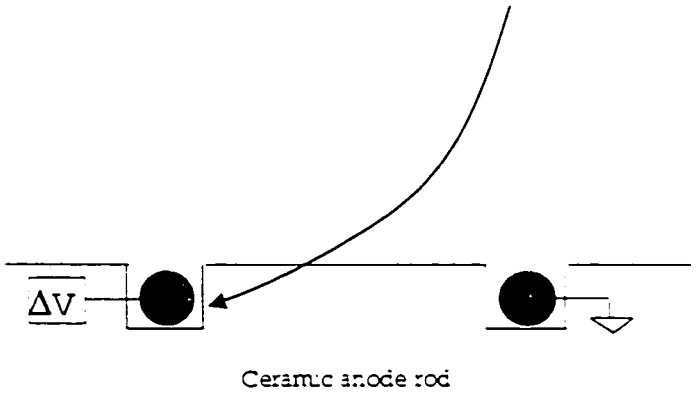

Figure 5.4: Representation of the possible problem associated with electrodes submerged beneath an insulating surface. One possible electric field line is shown.

the anode wires. However, the question arose as to how the weighting potential would be affected if the wires were so far into the groove that they did not have a direct line-of-sight path to the other wire. A schematic representing this possible problem is shown in Figure 5.4.

As detailed in Chapter 2, the normalized induced charge or weighting potential can be understood in a few different ways. For this problem, consider the calculation of induced charge by means of the method of mirror charges. Based on the formalism as presented in Chapter 2, it is clear that the charge induced on the conducting surface is equal in magnitude but opposite in polarity to the charge located a distance d from the surface. This has important consequences to the weighting potential on the non-collecting anode. From this derivation, it is important to also consider the induced charge on the non-collecting anode assuming the real charge is drifting towards the collecting anode. As the charge is far away from the col-

lecting anode, the non-collecting anode has a similar mirror charge induced on it determined also by the method of images. However, at a point as the charge drifts very close to the anode surface, the effect of the induced surface charge of the collecting anode is also perceived by the non-collecting anode. The result is that the effects of the real and induced surface charges are both observed on the non-collecting anode. In other words, the sum of both q and $-q$, or electrostatic neutrality, is induced on the non-collecting anode. So the non-collecting anode no longer has any induced charge on it from this situation and returns to a normalized induced charge of zero.

An alternate way of considering this problem is to examine the field lines associated with the anode rod as illustrated in Figure 5.4. When the anode wires are submerged in the ceramic rod, it is possible that the field lines could penetrate through the ceramic in order to terminate on the collecting anode. However, electrons will follow the field lines. In this case, it could be that some of the electrons are following the field lines until they impact the surface of the anode rod where they are trapped on the surface for a time greater than the charge collection time. If this occurs at a region such that the normalized induced charge on the non-collecting anode has not yet returned to zero, the detector will not be able to function in coplanar mode. By increasing the wire diameter such that the wires protrude from the surface, the percentage of the field lines penetrating the ceramic surface decreases.

The helical detector was opened and the anode was investigated under a microscope. The wires used were 0.01 inches in diameter. Under the microscope, it appeared that they did not protrude from the groove, thus potentially causing the aforementioned problem. They were replaced with wires that were 0.015 inches in diameter, large enough to protrude about half-way from the groove. A comparison of the spectrum resulting from this change is presented in Figure 5.5 with a second spectrum presented in Figure 5.6 with a pulser peak to demonstrate the significance of electronic noise on the results. In Figure 5.6, taken at ΔV = 600 V, the pulser FWHM is 166.63 channels, corresponding to 6.8% FWHM of electronic

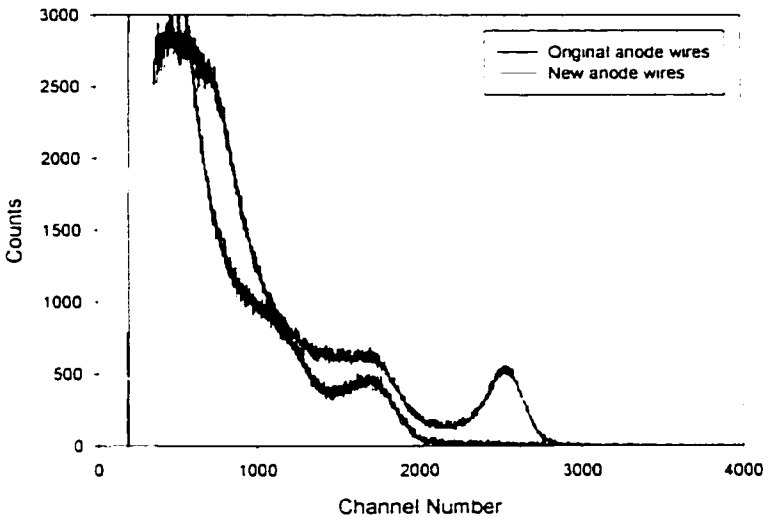

Figure 5.5: Helical detector spectra for the original and new anode wires, obtained with a cathode bias of -3 kV and ΔV = 700 V.

noise for the photopeak. As is evident, the quality of the photopeak demonstrated a clear improvement, even at a lower value of ΔV. This indicates that the slight change of wire diameter made a significant improvement on the weighting potential of the detector.

After the above spectrum was obtained, ΔV was increased to try to obtain coplanar mode operation. As it was increased, the pulse waveforms were monitored to look for signs of the non-collecting anode pulses becoming of opposite polarity as the collecting anode. However, as ΔV was increased, the pulses on the non-collecting anode did not all become negative in polarity. At ΔV = 1500 V, approximately 30% of the pulses on the non-collecting anode were positive in polarity, just like the collecting anode, but still smaller in amplitude. They did not equal the amplitude predicted by Figure 4.3. Approximately 40% of the pulses seen on the collecting anode had no corresponding pulse on the non-collecting anode. The remaining 30% of the non-collecting anode pulses were negative, but much smaller in amplitude than the pulses on the collecting anode. This demonstrated that, despite the fact that the calculations showed the required value to be ΔV = 217.6 V for a cathode bias of -3 kV , the helical detector was still not capable of op-

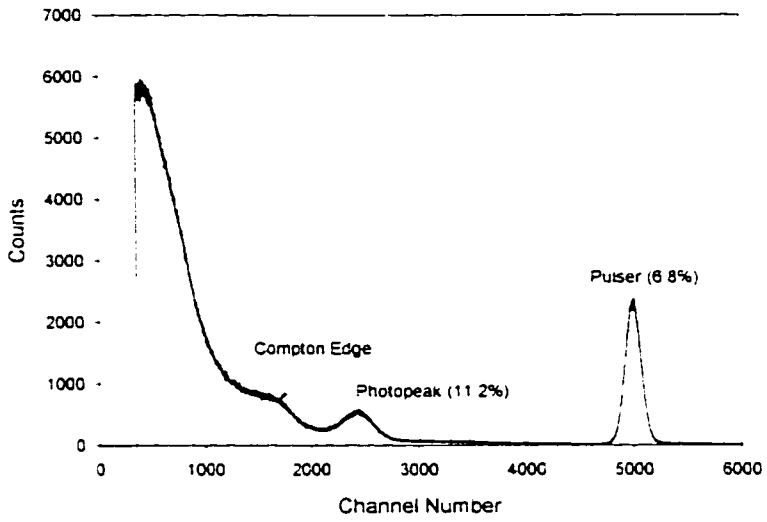

Figure 5.6: ^{137}Cs spectrum obtained with the anode wire refit with a cathode bias of -3 kV and ΔV = 600 V.

erating in full coplanar mode, as defined by the potential difference between the anodes such that 100% of the pulses on the non-collecting anode were of opposite polarity to the collecting anode. As ΔV was increased beyond 700 V, the resolution of the photopeak did not improve, as would be expected for a detector reaching coplanar mode operation. When ΔV was increased to 1750 V, the detector sparked, indicating that ΔV could not be increased further.

There are a few other important features to note about the spectrum shown in Figure 5.5. First, the photopeak is clear, but the resolution is quite poor: 9.03% FWHM. A second feature is the spectrum at energies less than the Compton edge. Instead of a flat continuum, an exponential is present. In fact, this shape is present in other works on high pressure xenon detectors that do not use coplanar anodes. [104] [74] [15] This feature is reduced for the case where the anode wires are larger, indicating more of the low energy events of the original wires were at a larger pulse amplitude since the detector was closer to attaining coplanar mode operation.

This effect can be explained by considering the drift velocity of the electrons in a large detector. The drift velocity of electrons in high pressure xenon at biases sufficient to collect all of the electrons is approximately 1 mm/μs. So if an

electron was created near the cathode and traveled the entire distance to the anode to be collected (a total of 37.3 mm), it would take approximately 37.3 μs to travel this distance, neglecting any lateral movement required to be collected by the collecting anode. However, most of the interactions within the xenon will not be single-event interactions such as from the photoelectric effect. Compton scatter dominates at the energies of interest in this work. If some charge was created by a Compton scatter near the cathode and the scattered gamma ray deposited the rest of its energy near the anode, these two events could be separated by a maximum of 37.3 μs. The maximum shaping time of the shaping amplifiers used in this work (Ortec model 672 or Canberra model 243) was 16 μs. So if the gamma ray events were separated by more than the shaping time, they would be recorded in the spectrum as two lower energy events instead of two events depositing the full gamma-ray energy. The drawback to using a larger shaping time is that more noise is included in the shaped peak. This concept has been described in Chapter 3 and poses a possible reason for the shape of the Compton continuum seen here.

5.2.1 Electron Cloud Considerations

Despite the fact that the complete electron collection on the collecting anode had not occured, for a single electron created in the detector, there should occasionally be pulses observed of the proper waveform since ΔV should have been high enough to completely collect at least some of the electrons on the collecting anode. In other words, there should have been observed a few cases where the pulses on the non-collecting anode were equal in magnitude yet opposite in polarity of the collecting anode.

This argument assumes, however, that the electrons are confined to a single point in space. This is not an accurate assumption since the energy deposition of a gamma ray creates an electron cloud of finite size. If the cloud size was reasonably large relative to the anode pitch and ΔV was not sufficient to collect all of the electrons on the collecting anode, there would be charge sharing between the two anodes. The result would be a pulse seen on the non-collecting anode that had

some positive pulse contribution due to the collection of electrons there.

In order to determine the severity of this potential problem, the electron cloud size was calculated using Geant4 for high pressure xenon as a function of gamma-ray energy and gas pressure as detailed in Chapter 3. For a gamma-ray energy of 662 keV with a xenon gas density of 0.5 g/cm^3, the resulting electron cloud diameter is approximately 3.28 mm. The pitch of the helical detector, on the other hand, is 4 mm with 2 mm in between any two electrodes. The ratio of the electron cloud diameter to the pitch would indicate the probability of there being electrons created directly above the non-collecting anode where the field lines would not bend enough to allow for their collection. So for a cloud diameter of 3.2 mm and a pitch of 4 mm, only 20% of the time would there be no overlap of the cloud directly over the non-collecting anode, as demonstrated in Figure 2.9. So if ΔV was not sufficient to completely pull the electrons to the collecting anode, there would always be some contribution due to charge sharing on the non-collecting anode.

Since the pitch and the electron cloud diameter are comparable, then 80% of the time if ΔV is zero or less than ΔV_{min}, there will be some contribution due to charge sharing. This further requires that ΔV needs to be sufficiently large to collect all electrons on the collecting anode.

5.2.2 Electronic Noise Analysis

While there were not significant coplanar pulses observed, there was still a photopeak evident in the spectra as shown in Figure 5.5. It is important to consider what the contributions are to the photopeak broadening in this spectrum to determine if they may be eliminated or minimized by a redesign of the system. The possible sources of noise internal to the detector include bulk leakage current, surface leakage current, and detector capacitance. The later can come from many sources including anode-cathode capacitance, anode-anode capacitance, capacitance between the anodes and the pressure vessel, and stray capacitance between the connectors and overall detector structure.

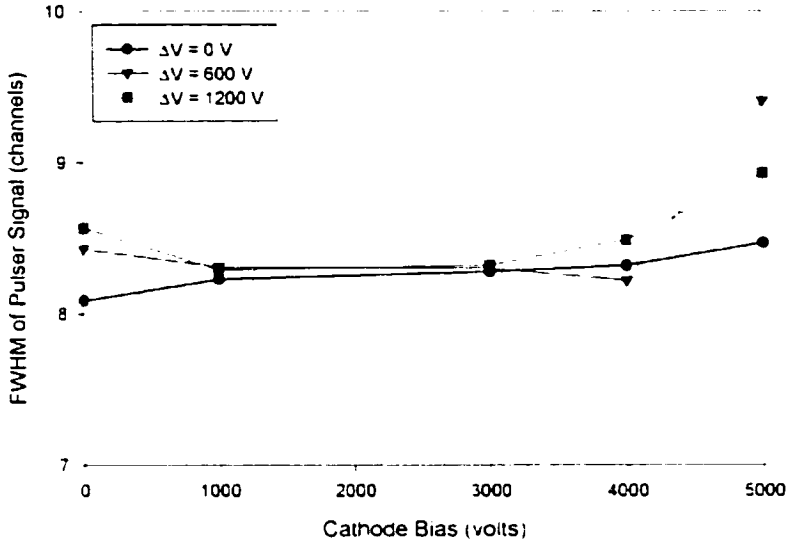

Figure 5.7: Measurement of the bulk leakage current contribution to the electronic noise of the helical detector.

In order to determine whether bulk or surface leakage currents were the source of significant electronic noise, a test pulse signal was used and the electronic noise was measured in terms channels of the full width at half maximum of the pulser peak. In order to determine the influence of bulk leakage current, the noise was measured as a function of cathode bias for a few different values of ΔV. This is shown in Figure 5.7. It is clear based on this data that there is not significant fluctuation in the electronic noise as a function of cathode bias, thus indicating that the bulk leakage current is not a significant source of the noise. The same measurement was repeated measuring the pulser FWHM as a function of ΔV as presented in Figure 5.8. Here again there is no significant change in the electronic noise, which suggests that surface leakage current is not contributing significantly to the photopeak broadening.

Finally, the capacitance between the anodes should be considered as a possible source of photopeak broadening. With 0 V applied to both the cathode and between the anodes, the pulser peak width was measured to be 8.09 channels FWHM. The main contribution to this noise would be detector capacitance. The

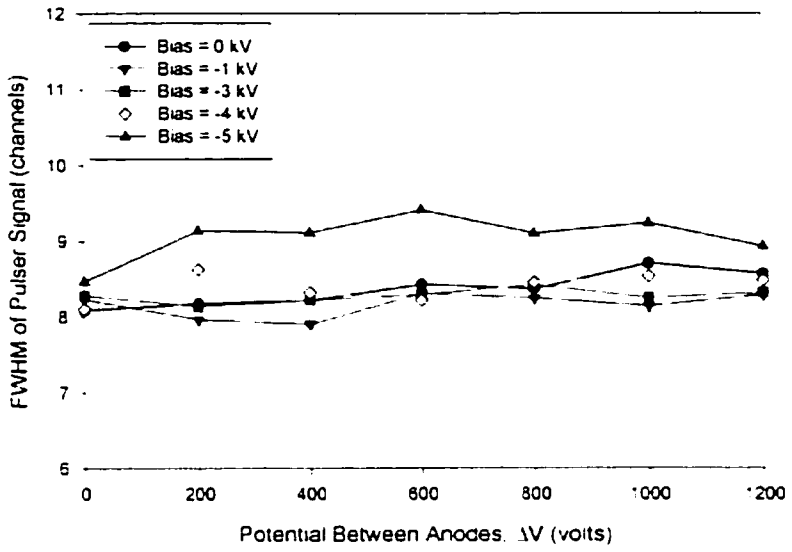

Figure 5.8: Measurement of the surface leakage current contribution to the electronic noise of the helical detector.

source of this capacitance was assumed to the be largest measured capacitance in the detector – the capacitance between the two anodes. This was measured with an Agilent 4263B LCR Meter to be 48 pF. This value is near the design goals for this detector and is not very large for a high pressure xenon detector. [97]

Additionally it is important to note the selection of preamplifier for high pressure xenon detectors. The preamplifiers used in this work were AmpTek A-250 charge-sensitive preamplifiers, a common choice for semiconductor spectrometers. These were chosen so more direct comparisons could be made between a coplanar xenon and coplanar CdZnTe device. Using the default feedback loop employing a 1 pF capacitor, C_F, we would expect a pulse amplitude given by

$$V = \frac{Q}{C_F} = \frac{n_0 e}{C_F} = \frac{WEe}{C_F} \tag{5.1}$$

where Q is the charge created in the detector created by n_0 electrons of unit charge e, determined by gamma-ray energy E and W, the mean number of electrons per unit energy. In the case of 662 keV photons in xenon with a W-value of 21.9 eV/ion pair, this would create a 5 mV pulse, assuming a 1 pF capacitor. CdZnTe, on the other hand, has a W-value of 4.7 eV/electron-hole pair resulting in a 22.6 mV pulse.

Hence, the signal-to-noise ratio for xenon using the default feedback loop and the same base electronic noise as a CdZnTe detector will be decreased from 11.3 to 2.5 assuming a constant 2 mV of electronic noise. However, the width of the pulser peak is less than that of the photopeak, so the problems cannot be entirely attributed to electronic noise.

5.3 Possible Coplanar Mode Failure Mechanisms

It is clear based on the fact that coplanar pulses were not seen at the predicted value of ΔV, or even several times that value, that there must be some process prohibiting the coplanar mode operation from working. There are several possible causes of this that will individually be considered. These include signal coupling from inductance or capacitance between the anodes, charge sharing due to an insufficient potential difference between the two electrodes, and the effects of stationary surface charge on the surface of the anode rod.

5.3.1 Mutual Inductance Between the Anodes

Since the helical detector was comprised of two coiled wires carrying current, the possible effects of mutual inductance must be considered. This occurs as a result of a change in charge flow between the two coils which creates a magnetic field. This magnetic field can then induce a signal on the opposite coil. The voltage of the induced signal, V_{in}, is determined by

$$\Delta V_{in} = \oint_l \vec{E} \cdot d\vec{l} = -\frac{d}{dt} \int_S \vec{B} \cdot d\vec{S} \tag{5.2}$$

where l is the path, $\vec{B}$ is the magnetic field, and S is the cross-sectional surface area. Hence, a change in the current on an electrode will create a changing magnetic field. This field will then induce a current on the neighboring electrodes.

Coupling of any kind can have detrimental effects to the operation of any coplanar anode detector. It is possible, based on Equation 5.2, that there could be an inductively-coupled signal. So for any change in magnetic field, which would be the result of changing current on the anode coils, a signal would be induced on

the opposite anode. If this system is considered to be an RL circuit, the induced current will have an angular frequency that is inversely proportional to the square root of the inductance. Additionally, the induced current will be 90 degrees out of phase of the charge. This implies that an inductively-coupled anode coil could also exhibit a delay between the measured signals on each anode.

It was not possible to make a measurement of the inductive coupling with the detector itself since the anode rod was not accessible. In order to determine if the mutual inductance could be the dominating factor, a test rod was constructed identical to the rod in the detector. Using a tail pulse generator, a charge was injected at various points along the rod and the output signal of each electrode was observed on an oscilloscope. The experimental setup is shown in Figure 5.9. A sample of the resulting pulses is shown in Figure 5.10 for a 58 mV input pulse (shown in yellow). This figure illustrates that there is some coupling between the two anodes, as evidence by the induced pulse on the non-collecting anode (shown in green). The results of similar measurements for various input pulse amplitudes and charge injection locations are presented in Table 5.1.

As is demonstrated by Figure 5.10 and Table 5.1, there is some sort of crosstalk between the two anodes. When a signal is generated on an anode, a signal is induced on the other anode. At small output voltages comparable to the expected voltages resulting from the deposition of 662 keV, this effect is quite small, if apparent at all. However, it becomes more prominent as the pulse amplitude is increased and could be an important clue to the failure of the helical detector. To determine if the magnitude of this crosstalk was related to the position on the anode rod, experiments were performed with the point of injection changing. A change in the magnitude of the coupling would suggest inductive coupling, since the inductance would increase with the number of turns of the inductor. Hence, the same test was repeated for the 18 and 58 mV pulse with the point of injection midway down the rod. Based on the data presented in Table 5.1 where the output was observed as a function of charge injection location, the magnitude of the induced signal did not change with test pulse injection position. However, this is not conclusive evidence

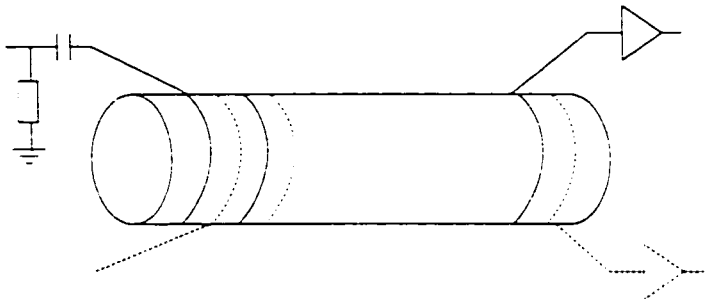

Figure 5.9: Schematic of initial anode rod simulation experiment. Charge is injected through a 2 pF capacitor on the upper left. The dashed lines indicate the electrode the induced signal is expected to appear on. The signal is measured through a charge-sensitive preamplifier.

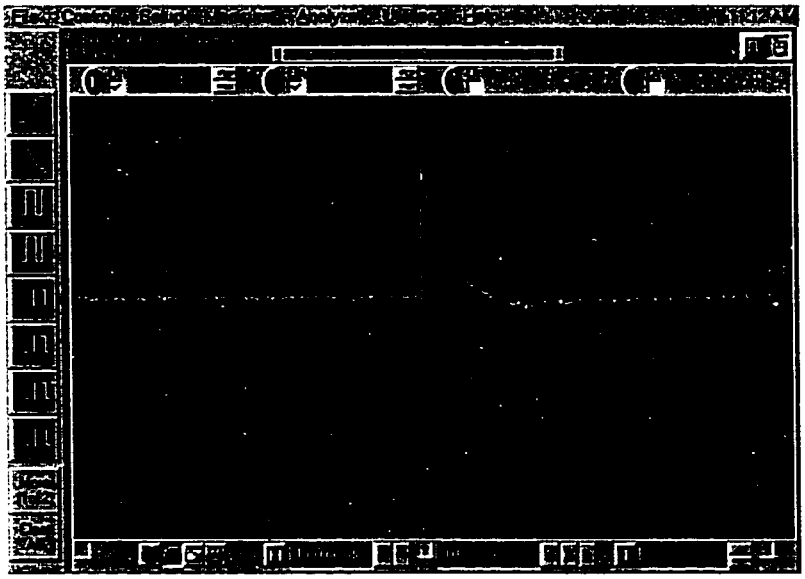

Figure 5.10: Sample data for the inductive coupling measurement where a 58 mV voltage pulse (yellow) is injected as a charge pulse on one anode while observing the coupled signal (green) on the other anode.

Table 5.1: Results of inductive coupling measurement

Input Pulse Amplitude (mV)	Charge Injection Location	Coupled Pulse Amplitude (mV)
2.5	end of rod	0
18	end of rod	2
58	end of rod	5
18	midway down rod	2
58	midway down rod	5
18	3/4 of the way down the rod	2
58	3/4 of the way down the rod	5

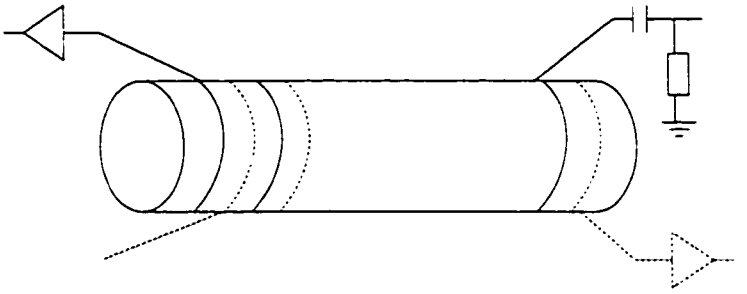

Figure 5.11: Schematic of initial anode rod simulation experiment, similar to that shown above. In this case, the charge is injected from the opposite side of the rod.

that the coupling is inductive.

In order to determine this, the input signal was moved to the opposite side of the test rod. This is analogous to flipping the leads of the circuit. The setup for this experiment is shown in Figure 5.11. If the induced signal originated from inductive coupling, the polarity of the induced pulse should be the opposite as the first case since the magnetic field creating the induced current has changed direction. The results of this experiment are shown in Figure 5.12. As is clear from the figure, the polarity of the induced signal did not change. Therefore it was concluded that inductive coupling could not explain the failure of this detector design.

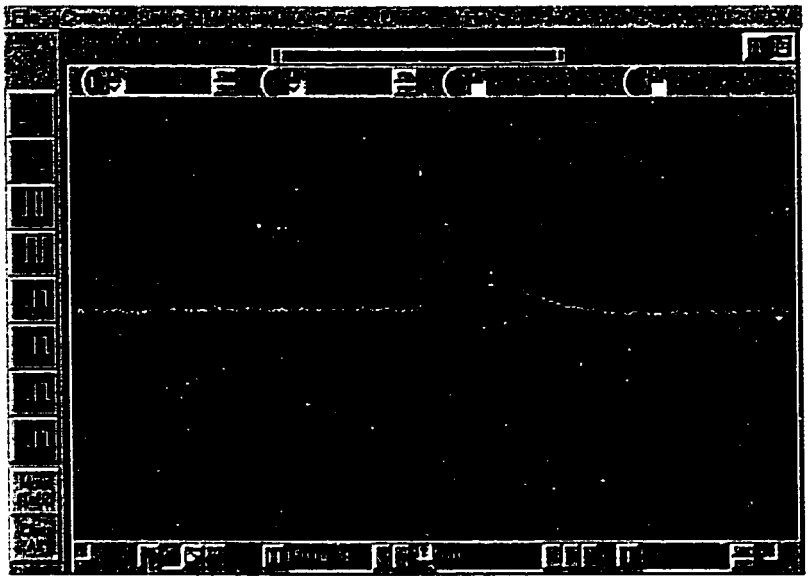

Figure 5.12: Output of the inductive test with a 58 mV pulse injected with the leads reversed.

5.3.2 Capacitive Coupling of the Anodes

Another possibility for the failure of the coplanar technique on the helical detector is capacitive coupling between the anodes. If the capacitance between the anodes of 48 pF was too high, charge induced on the collecting anode would be shared on the non-collecting anode. So both anodes would measure a signal of the same polarity. Since some crosstalk was observed in the previous experiment, an additional experiment was conducted to explore these effects further.

In order to ascertain if the capacitance was a problem, an experiment was performed with the preamplifiers as shown in Figure 5.13. The output of the preamplifiers was observed on the oscilloscope to determine if there were any variations in pulse height between the two cases. Such a variation would indicate the ratio of capacitive coupling between the anodes. If one considers the equivalent circuit, it should be noticed that the capacitance between the anodes and the AC coupling capacitor are parallel capacitances. In this case, the charge should go to the higher capacitance. So this experiment will provide a qualitative measure of the anode-to-anode capacitance relative to the 2 nF AC coupling capacitor. It was expected

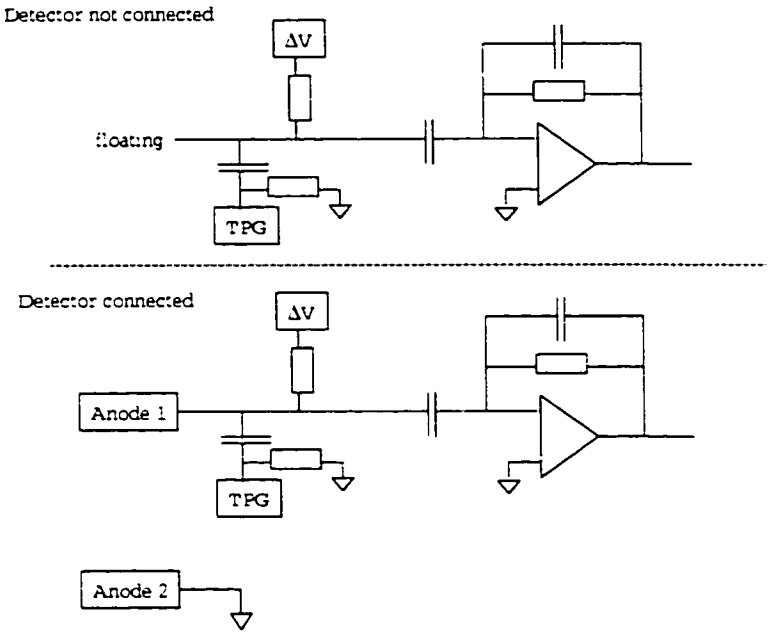

Figure 5.13: Setup for the measurement of capacitive coupling. In the first case, the pulse height of a test pulse is measured with the anode floating. In the second case, one anode is connected to the preamplifier while the other is grounded.

that, should there be excessive capacitive coupling, the pulse height without the detector connected should be greater than the case where the detector was connected. The results of this experiment are shown in Table 5.2. As is clear in the table, a difference of 0.25% between centroid locations for the two cases is measured. Therefore it was concluded that the anode-to-anode capacitance was small relative to the coupling capacitor. The electronic noise, shown as the FWHM of the shaped gaussian peak obtained on the multichannel analyzer, did increase significantly in these two cases. This is expected since the electronic noise should increase with even a slight increase in input capacitance such as from the addition of the 48 pF between the anodes. Therefore, it was assumed that capacitive coupling was not the cause of the coplanar mode operation failure.

Table 5.2: Results of capacitive coupling measurement between the two anodes

	Shaped Pulse Height	Centroid Channel	FWHM
Detector not connected	4.969 V	2013.69	4.89
Detector connected	5.000 V	2018.72	8.99

5.3.3 Surface Charge Considerations

It is clear from the results presented in previous sections that the helical detector was incapable of reaching voltages high enough for complete charge collection on the collecting anode. One possible cause of this is that the minimum potential difference required between anodes, ΔV_{min}, was not high enough, however it has been stated that this violates the calculated prediction. Another possibility to consider is the distortion of the electric field within the detector must be considered. One possible means of field distortion would be from a buildup of significant charge on the anode rod surface such that the electric field along a line perpendicular to both anodes was significantly distorted. For example, if the surface resistivity of the Macor ceramic was too high, electrons on the surface might not be able to move towards the collecting anode. If the surface charge density was high enough, the field could be distorted enough that the non-collecting anode was at a higher potential than the ceramic surface creating a local maximum of the potential at the non-collecting anode. In this event, any electrons created by interactions above the non-collecting anode would not be able to reach the collecting anode since it might require that they travel through a lower potential region in order to get there.

In order to determine what charge density would be required in order to create this problem, a simulation was performed using Coulomb 4.0. The helical detector was simulated with a cathode bias of -5 kV and ΔV = 1000 V. The potential along the anode was plotted along a line of constant radius on the anode rod surface for varying surface charge density. The results of this calculation are presented in Figure 5.14.

As seen in the figure, for charge densities less than -1×10^{-12} C/mm^2 (approximately 6.25×10^6 e$^-$/mm^2) the non-collecting anode, simulated at 4 and 8

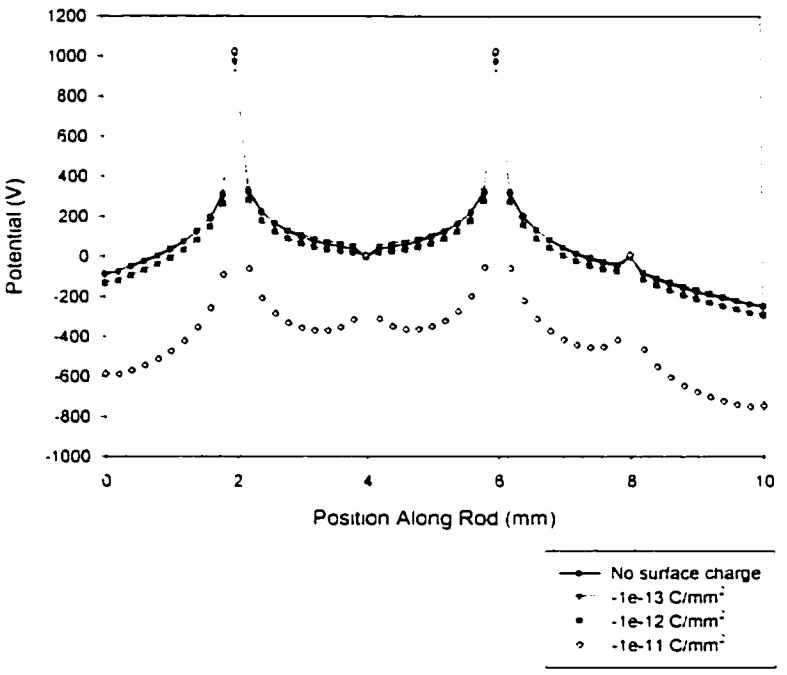

Figure 5.14: Calculated potential resulting from varying charge densities on the anode rod surface.

mm along the rod surface, shows a local minimum in potential. However, as the surface charge density increased to -1×10^{-11} C/mm^2 (approximately 6.25×10^7 e$^-$/mm^2), the potential at the non-collecting anode was at a local maximum. In this case, an electron near the non-collecting anode would not be able to reach the collecting anode since it would have to travel through a region of lower potential.

This can also be approximated using the following equation for surface charge density:

$$\sigma = \epsilon E \tag{5.3}$$

where ϵ is the permittivity and E is the magnitude of the applied electric field. In the case of cylindrical geometry,

$$E(r) = \frac{V}{r \ln(\frac{b}{a})} \tag{5.4}$$

where V is the applied bias, a is the anode radius, and b is the cathode radius. For the dimensions of the helical detector and a cathode bias of 5000 V, the electric

field when $r = a$ is calculated by Equation 5.4 to be approximately 2873 V/cm. If this value is used in Equation 5.3 approximating ϵ with ϵ_0, the permittivity of free space, a space charge of 2.54×10^{-12} C/mm^2 is obtained. This value agrees well with the results obtained by Coulomb.

This, however, raises the question of whether or not this is a realistic amount of charge. In other words, how likely is it to reach electron surface charge densities this high?

Coulomb, like other electrostatic simulation packages, calculates the potential using finite element analysis. For example, when a voltage is applied to a particular surface, that potential is converted to a surface charge and then calcuations are performed using the Poisson equation for surface charge densities. The same can be thought of in reverse – if a surface charge density has been supplied to the code, what is the voltage equivalent if the anode rod is assumed to be a conductor?

In order to calculate this, a simple simulation was conducted involving a sheet of area 400 mm^2 at a potential of 1000 V. The resulting calculated surface charge was 5.7×10^{-10} C or 1.43×10^{-12} C/mm^2. Hence, a surface charge density on the order of 10^{-12} C/mm^2 would correspond to a potential of 10^3 V. This surface charge would establish an electric field that would be in the opposite direction as the cathode and anode biases. So at the critical value of the surface charge density shown in Figure 5.14, the electric field of the detector would be disrupted by the counteracting influence of the surface charge field. It was, therefore, important to experimentally determine if this was happening, which could be done by measuring the current flowing through the detector.

5.3.4 IV Curves

In order to experimentally verify that the build up of surface charge was not a problem, current versus voltage profiles, also referred to as IV curves, were obtained. The experimental setup can be seen in Figure 5.15.

With systems operating normally, as the potential difference is increased between two electrodes, the current should also increase. If ohmic considerations are

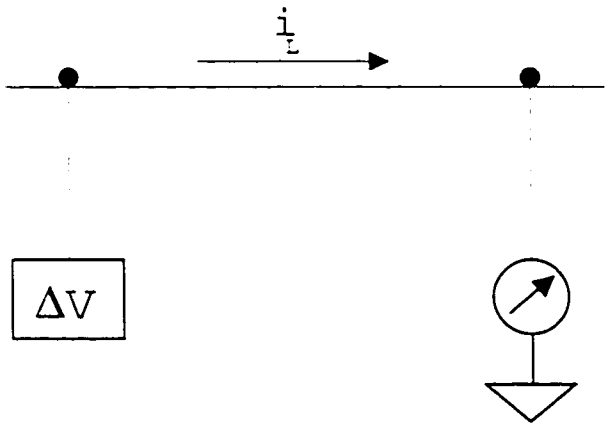

Figure 5.15: Experimental setup used for the IV curve measurements. The current was measured with a Keithley 6514 System Electrometer.

assumed, the current should increase linearly with voltage as given by Ohm's law:

$$I = \frac{V}{R} \tag{5.5}$$

where R is the resistance between the two electrodes.

IV curves were obtained for the helical detector for several different conditions. The voltage was varied between 0 V to 1000 V and 0 V to -1000 V. In both cases, the initial voltage was 0 V and then increased to 1000 V (or decreased to -1000 V) and then returned to 0 V. The current was measured six times at each voltage in order to allow the measurement to settle with time. Each of the six measurements was an average of four values of the current obtained in a short time span. For the data shown here, the last measurement value of the six values is presented since it was taken at the longest difference in time from the initial change in voltage, ΔV.

In order to ascertain the minimum required amount of time for the current to reach a steady state, the voltage was rapidly increased from 0 V to 500 V and the current was monitored for 4000 s. The results of this measurement are shown in Figure 5.16. Based on these measurements, it was determined that waiting for a minimum of 150 s would be an adequate amount of time to allow the current to settle. The same measurement was repeated for a rapid increase in potential from 0 V to 1000 V, as shown in Figure 5.17. These results agreed with Figure 5.16. To be safe, it was decided that the detector would be allowed 300 s in between voltage changes for which the current to settle.

Once the minimum acceptable time difference between measurements was established, the IV curves could be obtained. The first measurement involved measurements from 0 V to 1000 V and then returning to 0 V. The results of this measurement can be seen in Figure 5.18. There are several interesting observations that can be made based on these results. While the curves show the positive slope predicted by Ohm's law, the current should always be greater than zero if ΔV is greater than zero. However, as is shown in Figure 5.18, the current was negative when ΔV was below a certain value. Similarly, if ΔV is negative, the current should also be negative. This is similarly contradicted by the data for this experiment, shown in

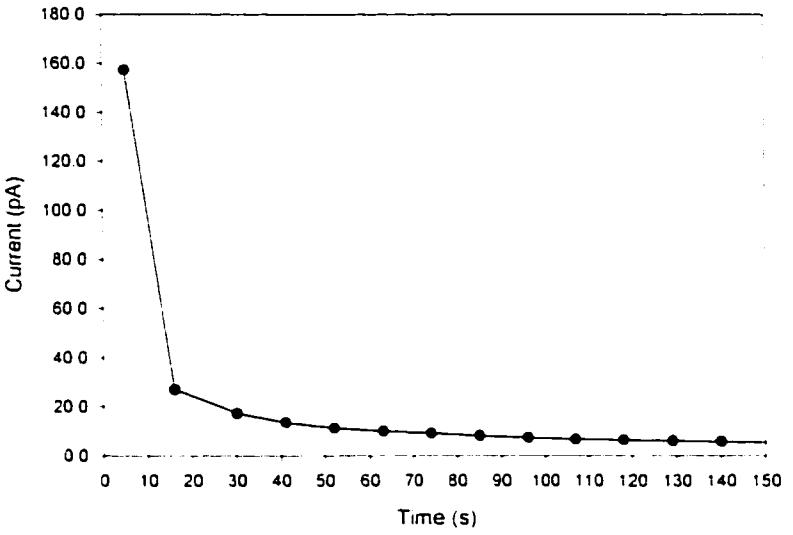

Figure 5.16: Current stability profile between anodes of the helical detector with ΔV = 500 V.

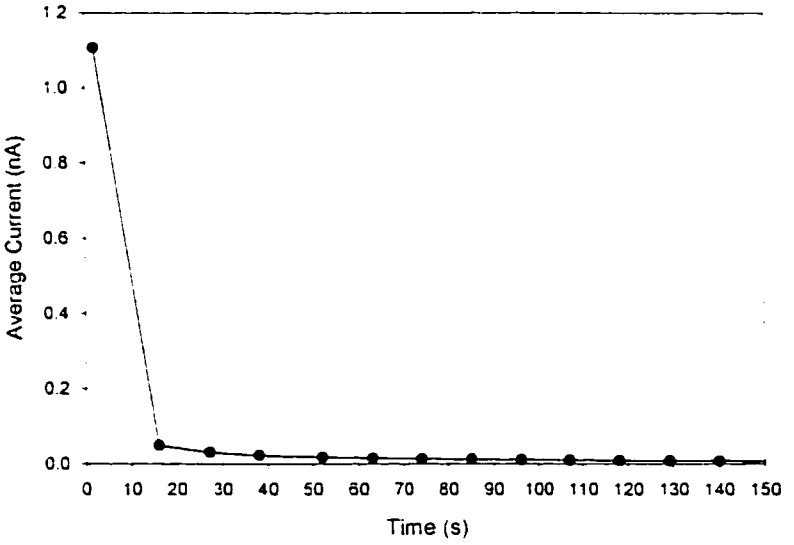

Figure 5.17: Current stability profile between anodes of the helical detector with ΔV = 1000 V.

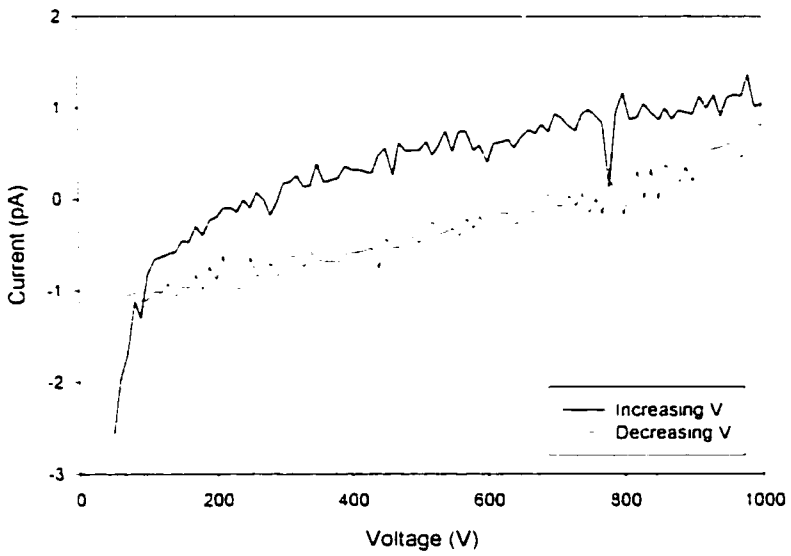

Figure 5.18: IV curve between anodes for the helical detector using the sixth data point and a time delay of 300 s for 0 V $\leq$ V $\leq$ 1000 V.

Figure 5.19.

Another observation to be made on this data is that the currents measured were quite small, on the order of 10^{-12} amperes. However, it was not known if this was within the noise of the electrometer used for these measurements. Data was then taken for the case where the electrometer was not connected to the detector in order to ascertain the fluctuations in the measurements. These results are presented in Figure 5.20. It is clear from the figure that the electrometer demonstrated fluctuations on the order of 10^{-15} amperes, three orders of magnitude smaller than the measurements presented in Figures 5.18 and 5.19. Thus it was concluded that the data shown in these IV curves were above the noise of the system.

One possibility that was considered was the drift of the current measurements over the time required to complete the IV curve. Several hours was required to complete one leg of the measurement. The electrometer could have drifted over this time thus distorting the results. To rule out this possibility, another curve was obtained where the voltage was increased from 0 V to 1000 V. At this point, the measurement was paused while the electrometer was recalibrated. Then the

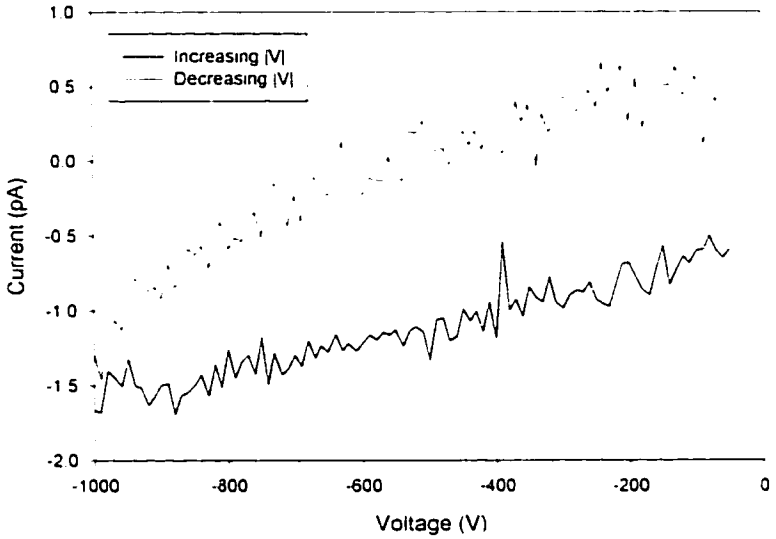

Figure 5.19: IV curve between anodes for the helical detector using the sixth data point and a time delay of 300 s for -1000 V $\leq$ V $\leq$ 0 V.

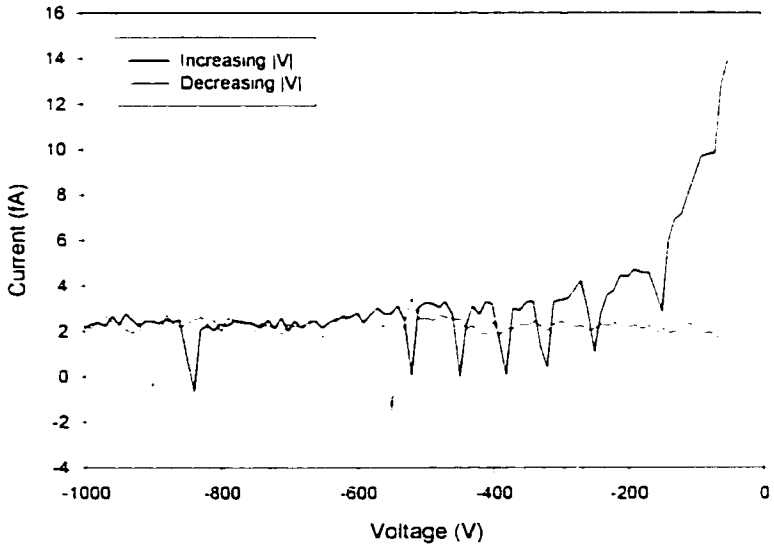

Figure 5.20: Current fluctuations observed with the electrometer not connected to the detector using the sixth data point and a time delay of 300 s.

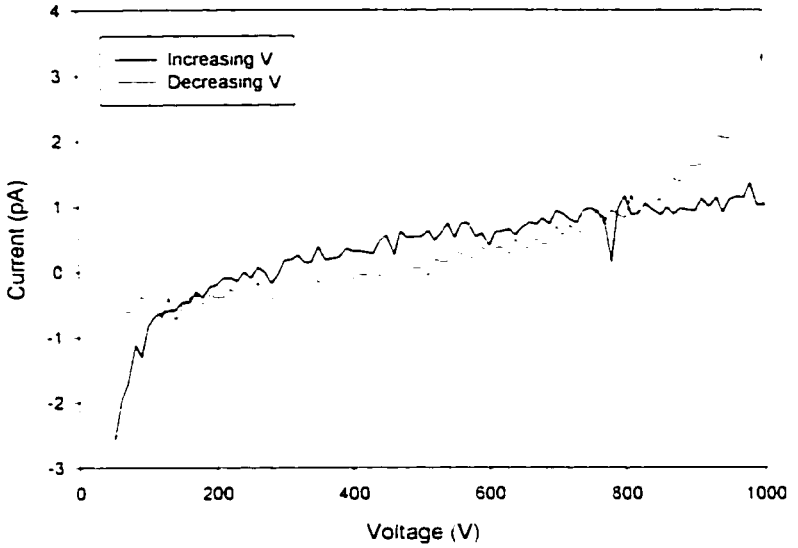

Figure 5.21: IV curve between anodes for the helical detector when the electrometer was recalibrated after the first leg.

voltage was decreased back to 0 V. This was also performed for the case where ΔV was decreased to -1000 V. The IV curves obtained from this experiment are shown in Figure 5.21. It is clear from these figures that the current appears to flow in the wrong direction for cases where $|\Delta V| < 400$ V.

While these results initially seemed peculiar, they can be explained by considering the work function of the metals involved in this measurement. There are several dissimilar metals in contact with each other in this setup. The anode wire, made of nickel, connects to the high-voltage feed-through, made of steel, which is connected to by a gold connector pin that is soldered to a copper wire that is soldered to a triaxial connector to the electrometer. The work functions for several of these metals is presented in Table 5.3. Although the actual analysis of this system is difficult since there are so many dissimilar metals involved, a simple solution is possible. If the situation is considered where there are two dissimilar metals in contact with work functions given by Φ_1 and Φ_2 where Φ_1 is greater than Φ_2 (shown in Figure 5.22), a current will automatically be established. The flow of electrons will be in the direction of the metal with the lower work function. So any current to be

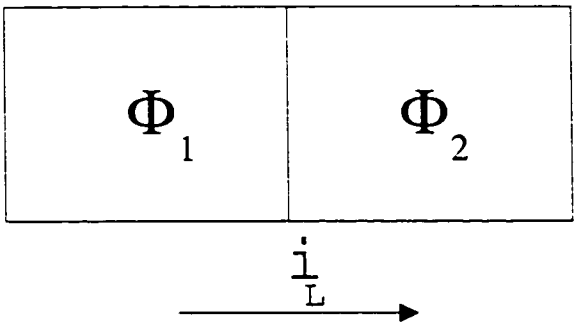

Figure 5.22: Representation of current flow with two dissimilar metals in contact where $\Phi_1 > \Phi_2$.

measured outside of this system must first increase to the point where it is greater than this pre-established current before its polarity will make sense. Given the fact that the currents measured in this experiment were so low, it is possible that the current generated by the different work functions established a current of opposite direction than expected. So when the magnitude of ΔV increased above 400 V, the current along the surface of the ceramic was able to overcome that established by the contact of the dissimilar metals.

Finally, IV curves were obtained for the same cases as those presented above, however with a gamma-ray source present. The purpose of this experiment was to determine if the electrons generated by the gamma-ray interactions within the gas were capable of reaching the collecting anode or if they were accumulating on the surface since the leakage current was so low.

In order to conduct this experiment, the potential between the two anodes was

Table 5.3: Values of the work function for several of the metals used in this experiment [68]

Element	Plane	Φ (eV)
Au	100	5.47
	110	5.37
	111	5.31
Ni	100	5.27
	110	5.04
	111	5.35
Fe	100	4.67
	111	4.81

increased to 1000 V and then decreased back to 0 V (without stopping for recalibration at the endpoints). First the same procedure was followed as previously described to obtain the IV curves with the cathode floating. Then, the procedure was repeated with the cathode at a bias of -5 kV. Finally, the IV curves were obtained with a ^{137}Cs gamma-ray source present. The results from this experiment are presented in Figure 5.23.

As can be seen in the figure, the IV curves for the first two steps in the experiment look similar to those previously shown. There should be no appreciable difference between the two since there is a negligible change in current between the two. However, when the gamma-ray source was added, there was a dramatic change in the IV curve slope. The measured current saturated to the levels seen in the first two parts of the experiment at approximately 1000 V.

This result is easily understood by considering what the expected result would be in a functional coplanar anode system. With no potential difference between the anodes, the electrons created within the gas, assuming an adequate drift field is established by the cathode, should move towards both anodes with some probability. Thus, the grounded electrode attached to the electrometer should see a large current as a result of these electrons. This is illustrated in Figure 5.24. As the potential difference, ΔV, is increased, more and more of the electrons will be collected by the collecting anode until a value is reached when they all go there. At this point, the current measured on the non-collecting anode should return to

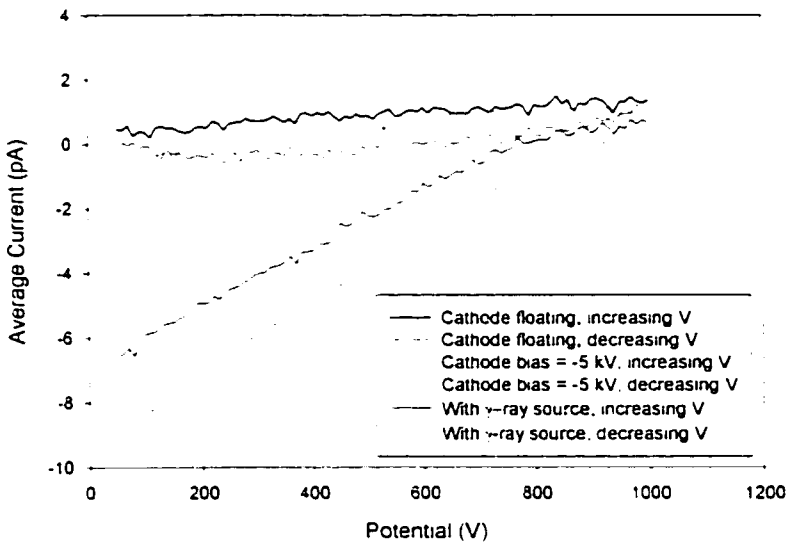

Figure 5.23: IV curves taken with the cathode floating, cathode biased at -5 kV, and cathode bias with a gamma-ray source.

the value that would have been measured if the only source of current was from the leakage across the ceramic surface.

As it can be seen in Figure 5.23, the current behaves as would be expected for a properly-functioning coplanar anode device. The current is initially large and negative illustrating the motion of the electrons towards the non-collecting anode. However, as ΔV increased, fewer and fewer electrons go to the non-collecting anode until the current begins to level off for values of ΔV greater than 800 V. This demonstrates that the build up of surface charge on the anode rod did not distort the electric field significantly since, had this been the case, the current would not have properly flown to the collecting anode when the electrons created from gamma-ray interactions built up on the surface of the Macor. These results are puzzling since they indicate the helical detector should have been able to function in the coplanar mode assuming ΔV was set greater than 1000 V. However, this was not supported by the pulse waveforms seen at this low potential.

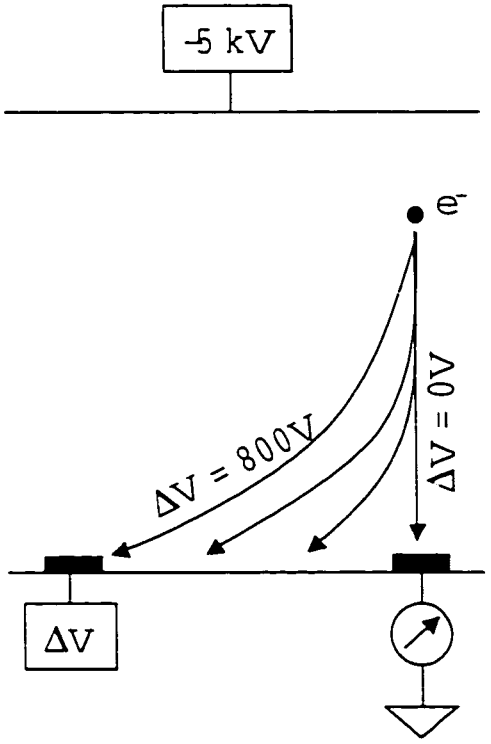

Figure 5.24: Schematic representation of the movement of electrons created by a gamma-ray source as ΔV is increased.

5.4 Conclusions about the Helical Detector

While it is clear that the coplanar mode was not achieved with the helical detector, there are important conclusions to be drawn from the available observations. Most importantly, all of the presented results show that there is no clear reason why the helical detector should not work. However, based on these results it was clear that the helical design was not directly analogous to the parallel plate coplanar semiconductor devices. So a new device was designed of a parallel plate geometry to try and determine whether or not a coplanar high pressure xenon detector was even possible. The results of this detector are presented in the next chapter.

In terms of the helical detector, it is evident that any future redesign must consider the anode structure more carefully. It was demonstrated above that a significant improvement in the photopeak was possible simply by changing the diameter of the anode wires to ensure that they protruded above the carved groove on the ceramic rod. It is possible that the wires are still not large enough and still limiting this detector. It is logical to question whether there is a upper limit on the wire diameter. The wires chosen for the replacement were chosen because they best fit within the groove with a slight protrusion. However, this was only verified by a rough, visual inspection.

It was demonstrated that neither the bulk nor the surface leakage current were dominant sources of noise with this detector. This was not surprising since the anode rod was made of a very high resistivity ceramic to minimize any surface leakage current problems. Additionally, the capacitance between the anodes was measured to be 48 pF – not excessively high so as to prevent coplanar mode operation.

The possible contribution of mutual inductance was also examined. This was done by injecting a charge pulse onto an anode rod simulator while observing the coupled signal on the opposite anode. Since the polarity of the coupled signal did not change when the direction of the magnetic field was reversed, it was determined that inductive coupling was not the source of the problem.

The possibility of electric field distortion was also considered from such sources as too much charge buildup on the anode rod surface. A calculation was performed to determine that a surface charge density on the order of 10^{-12}C would be required to significantly distort the field enough to prevent coplanar mode operation, but this possibility was eliminated when the equivalent potential was calculated to be on the same order of magnitude as the cathode bias. However, further experimentation was conducted on this concept by analyzing the IV curves from the detector. Based on considerations of the IV curves taken in the presence of a gamma-ray source, it is clear that the coplanar mode operation should have begun at potentials of greater than approximately 1000 V. While this was nearly a factor of two greater than that predicted by the mathematical model, it is still reasonable since the model makes many assumptions, including that the potential is constant throughout the detector at the critical point of one pitch width below the anode.

Despite the lack of evidence of coplanar mode operation, this design still has many advantages and, since a clear reason for its failure has not been demonstrated, is worth further exploration due to the benefits of operating with a detector of a cylindrical geometry using a $\frac{1}{r}$ field.

Chapter 6

RESULTS AND ANALYSIS OF THE PARALLEL PLATE DETECTOR

The parallel plate detector was constructed as a "proof of principles" detector since, based on the results in the previous chapter, it was not clear that the concept of coplanar anode designs could work. The parallel plate detector was built to answer this question. The anode structure was placed in an existing pressure vessel that was not optimized for this structure. As a result, there was a dead region of xenon in a cylindrical shell about the center, active region. Thus, more counts in the lower energy portion of the spectrum would be expected from down scatter within this region. The anode design is based on the Generation 3 designs developed for CdZnTe. [51] Based on the data to be presented in this chapter, it will be shown that it is possible to operate a high pressure xenon detector in coplanar mode. However, there are several limitations on this detector that prevented good spectroscopic performance. It is possible to either eliminate or minimize the contributions of some of these factors, as will be described in this chapter.

6.1 Preliminary Parallel Plate Pulses

When the detector was initially connected, the preamplifiers had a feedback capacitance of 0.3 pF. Assuming a W-value of 21.9 eV/ion pair, a pulse amplitude of approximately 16.1 mV was expected. However, in the case where $\Delta V = 0$ V, we would not expect that the pulses would be this large since there will be charge sharing between the anodes as with the helical detector. Since the expected electron cloud diameter in xenon compressed to 0.5 g/cm^3 is approximately 3.2 mm and the pitch of the parallel plate detector is 4 mm, the electron cloud, prior to any

diffusion considerations, will be large enough to induce signal on both anodes. It is only with the application of a high enough ΔV that charge sharing effects will be minimized.

Pulse waveforms were observed from a ^{137}Cs gamma-ray source with $\Delta V = 0$ V and a cathode bias of -4500 V. Clear pulses were obtained ranging in amplitude to approximately 8 mV. The majority of them, as expected, were shared between the two anodes. Attempts were made to increase the cathode bias beyond -4 kV, however the detector sparked at approximately -4.5 kV. Unfortunately, at this low bias, the electric field of 2 kV/cm required to minimize the effects of electron trapping would not be possible. For the protection of the anode preamplifiers, it was decided that the cathode bias should not be higher than -4 kV. It was hoped that an electric field of 1.3 kV/cm would be sufficiently high to avoid significant trapping.

The rise times of several pulses were measured in order to determine if there was significant trapping. For an electron traveling from the cathode to the anode under the given electric field of 1.5 kV (where measurements were taken before the detector sparked), the longest pulse rise time can be determined as follows:

$$t = \frac{d}{v_e} = \frac{3cm}{1\frac{mm}{\mu s}} = 30\mu s \tag{6.1}$$

where v_e, the electron drift velocity was chosen to be 1 $\frac{\mu m}{ns}$ for a field of 1.5 kV/cm and a density of 0.5 g/cm^3. [74] The rise time of the pulses was measured and it was observed that the events with the longest rise times had times even slightly greater than this value. This would be expected if the electrons were traveling at less than 1 mm/μs or of their pathlength was increased due to the lateral movement from the region beneath the non-collecting anode. So it was concluded that the gas was sufficiently pure so that electrons generated near the cathode could be collected.

The next step was to increase ΔV to a value sufficient for complete electron collection on the collecting anode. It was determined in Chapter 4 that, for a cathode bias of -4 kV, we require $\Delta V = 232$ V. As ΔV was increased to 100 V, a fluctuation was observed on the baseline of the signal with the pulses from gamma ray su-

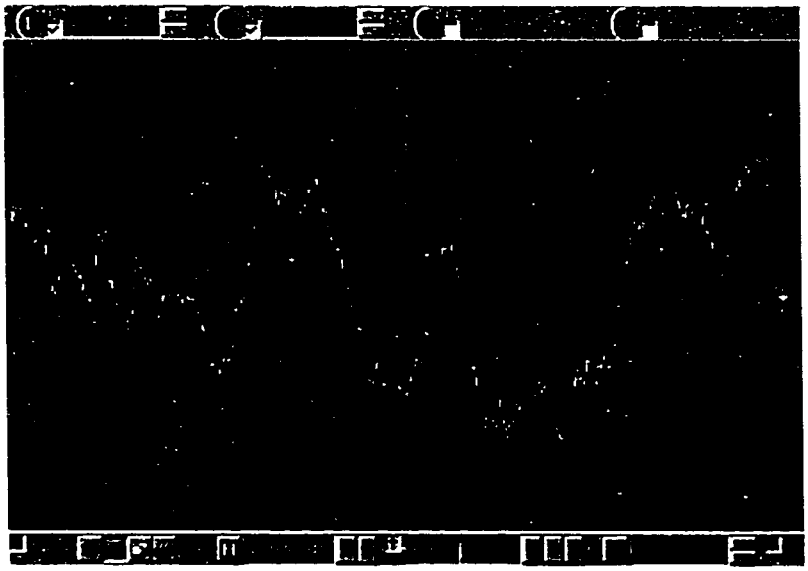

Figure 6.1: Example of the baseline fluctuation problem for ΔV = 300 V with no triggering at a time scale of 20 ms/division.

perimposed on it. This baseline fluctuation was of opposite polarity for the two anodes. It was found that as ΔV increased, the fluctuations increased as well. While their magnitude also fluctuated greatly, it was observed that the magnitude of fluctuation increased with ΔV. At ΔV = 240 V, the oscillations were as large as 400 mV with a preamplifier feedback capacitance of C_F = 0.3 pF or 40 mV with C_F = 1 pF. An example of this fluctuation for the default feedback loop is shown in Figure 6.1 where the yellow waveform is the collecting anode signal and the green is the non-collecting anode signal. No fluctuation was observed without a potential difference between the anodes, but as ΔV increased, so did the fluctuation. Since the frequency of the oscillation, while not constant, was of the same order of magnitude as the rise time of pulses due to gamma rays, the shaping amplifier was not able to filter it out.

An important observation can be made from the data shown in Figure 6.1. It is clear that the oscillation seen on the two anodes is opposite in polarity. This would suggest that there is some sort of charge movement between the two anodes since, if the signal resulted from somewhere else in the detector it would create a signal of the same polarity on both anodes.

In order to determine the source of the fluctuations, the pressure vessel needed to be opened in order to inspect the detector for damage or other clues that could indicate a problem. When the pressure vessel was opened, it was discovered that one of the anode wires was not properly connected. Since it is not possible to use solder in high pressure xenon detectors because it outgases material that could harm the gas, all connections in the detector must be either mechanical or made with a spot welder. In the case of the parallel plate detector, the later technique was used. When the anode wire connections were inspected, it was evident that one of the anode wires had not properly been welded resulting in a poor connection. When the wire was welded again to the connector, the aforementioned baseline fluctuation disappeared.

6.2 Pulse Waveforms After Detector Repair

Upon repair of the detector, the pulse waveforms were observed with a cathode bias of -4 kV and ΔV = 300 V. A sample of the pulse waveforms seen at these conditions is shown in Figure 6.2. As can be seen in the figure, coplanar pulses without a baseline fluctuation problem were evident for the first time in a high pressure xenon detector. The signal on the non-collecting anode was opposite in polarity as that of the collecting anode. Further data supporting this statement is evident if the individual pulse is analyzed on a shorter time scale as shown in Figure 6.3. As is demonstrated in the figure, the signals on the collecting and non-collecting anode initially increase in the first 20 μs of the event. The signals are equal, as reflected by the fact that the subtraction circuit signal is still zero in this time frame, in agreement with the predicted weighting potential shown in Figure 2.7. However, at a certain point corresponding to approximately one pitch width beneath the anode surface, the signal on the collecting anode rises quickly while that of the non-collecting anode returns to zero, also as predicted. The risetime in this portion of the pulse is approximately 8 μs, which differs slightly from the expected value of 4 μs. However, the predicted value is based on the fact that the detector has a 4 mm pitch determining that this transition point occurs exactly at

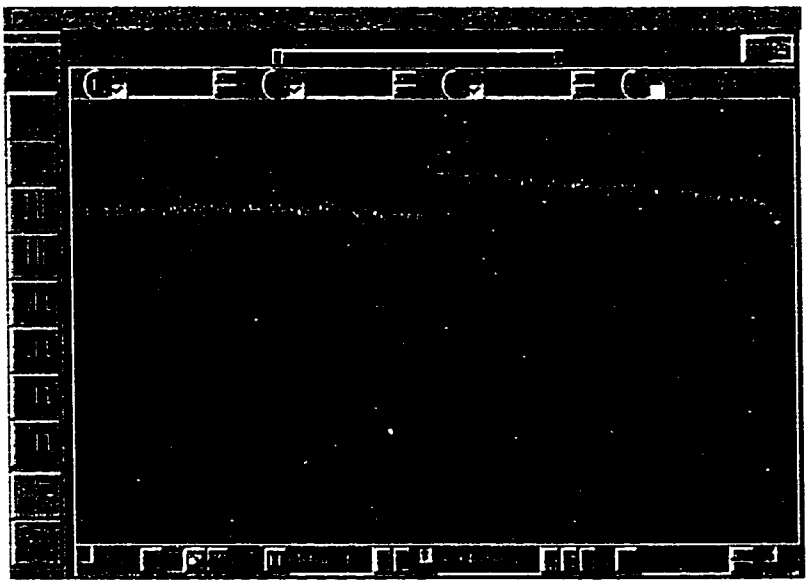

Figure 6.2: Sample coplanar pulses obtained with a cathode bias of -4 kV and ΔV = 300 V on a time scale of 100 μs/division.

this point beneath the anode surface. In reality, there will be some variation in the true distance to the anode that this really occurs. Additionally, the value of 4 μs assumes that the electrons are traveling at a velocity of 1 mm/μs. This is the reported velocity for a field of 2 kV/cm, but it may be lower since the pulses shown in Figure 6.3 were observed with a drift field of 1.3 kV/cm. Lastly, this assumes that the electrons go directly to the collecting anode without diversion from underneath the non-collecting anode. If the electrons are diverted from underneath the non-collecting anode, they will in reality travel further than 4 mm.

6.3 New Anode Spectra

Once it was demonstrated that the parallel plate detector was capable of operating in the coplanar mode, spectra were obtained for a variety of bias conditions. The spectrum for the comparison case with a cathode bias of -4 kV and ΔV is shown in Figure 6.4. A pulser peak is shown in this figure to demonstrate the contribution due to electronic noise, which has a width of 7.1%. As is evident in the figure, the photopeak is very broad with a resolution of 14.7 % FWHM. This was improved

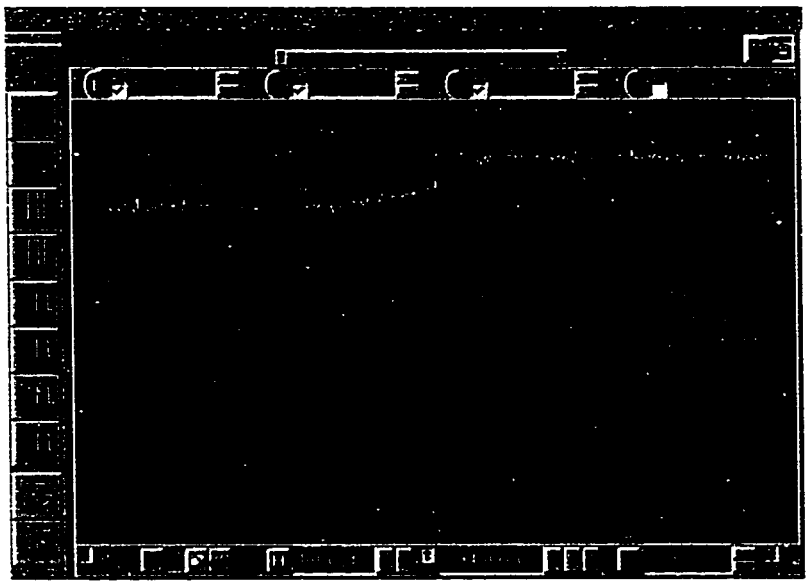

Figure 6.3: Sample coplanar pulses at a time scale of 10 μs/division, illustrating the slow rise as the electrons drift within the bulk and then the deviation between the collecting and non-collecting anode signals as the electrons are diverted to the collecting anode.

to 12.7% with 9.8% electronic noise using a different operational amplifier in the subtraction circuit with a smaller bandwidth (thus resulting in the electronic noise FWHM decreasing to 5.1%) as shown in Figure 6.5.

First, it is worth determining whether this is an improvement over a classical gridless ionization chamber. In order to determine this, the parallel plate detector was operated as a classical ionization chamber with 0 V between the two anodes. This was then compared to the spectrum with the same bias and ΔV = 300 V as obtained through the subtraction circuit. The results from this measurement are shown in Figure 6.6. As is evident from the figure, the spectrum from the classical ionization chamber shows no photopeak. This is to be expected since the weighting potential for this case would be approximately as shown in Figure 2.1. In this case, the movement of the slow ions contributes to the signal and the collection of the full energy deposited within the detector relies on their collection. However, when ΔV is increased to 300 V, a photopeak is clear. (Note that the change in location of the pulser peak is the result of the slight difference of gain between

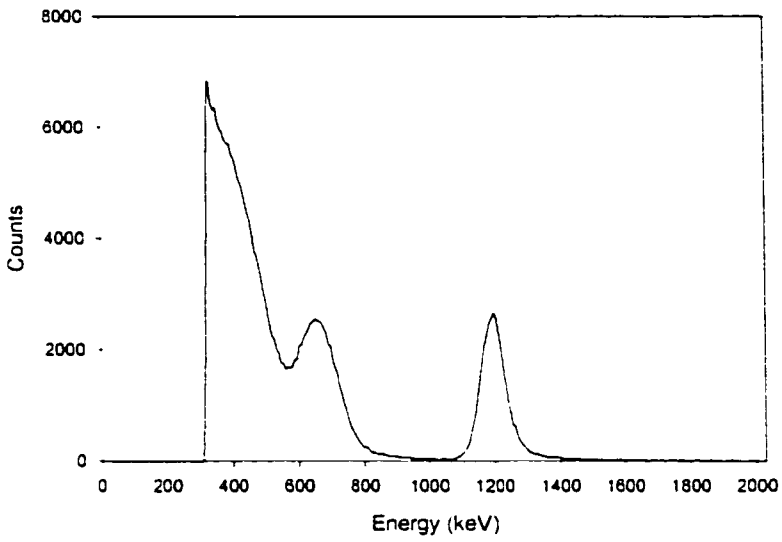

Figure 6.4: ^{137}Cs spectrum for a cathode bias of -4 kV and ΔV = 300 V.

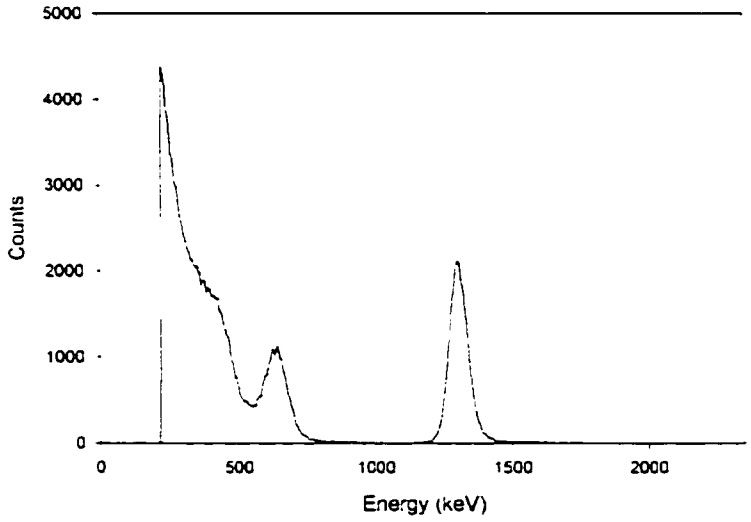

Figure 6.5: ^{137}Cs spectrum for a cathode bias of -3 kV and ΔV = 300 V.

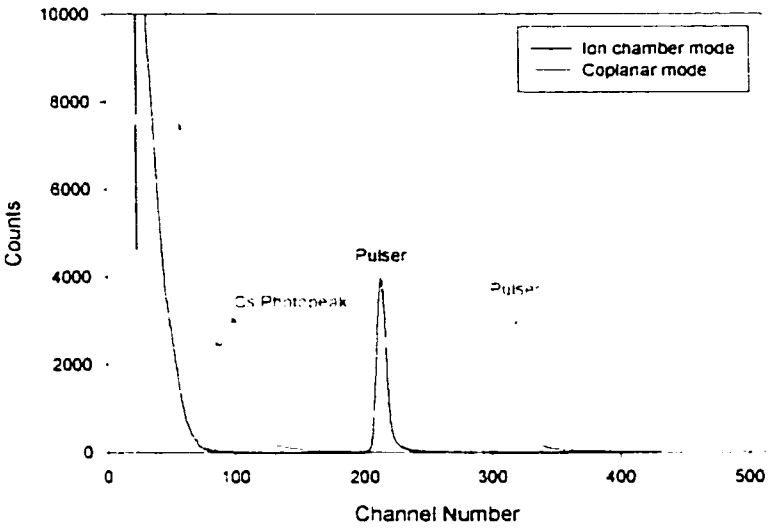

Figure 6.6: Comparison of the ^{137}Cs spectra for the parallel plate detector operated in the classical ionization chamber mode versus coplanar mode.

the signal shaped directly from the preamplifier as done for the classical ionization chamber versus that from the subtraction circuit, which was at a gain higher than unity.) This indicates that the use of the coplanar anode technique has improved the spectroscopic performance of the high pressure xenon detector.

6.4 Analysis of Electronic Noise from Leakage Current and Detector Capacitance

As with the helical detector, an analysis of the electronic noise was performed in order to ascertain its major contributors and determine if these problems could be fixed or minimized in future detectors. The electronic noise was measured through the subtraction circuit as a function of the different bias voltages both on the cathode and between the anodes. The former bias provided a measure of the contribution due to bulk leakage current while the later indicated the contribution of the surface leakage current. A measurement taken with 0 V applied to all electrodes indicates the severity of capacitance on the electronic noise.

The measurements of the noise due to the bulk and surface leakage currents is

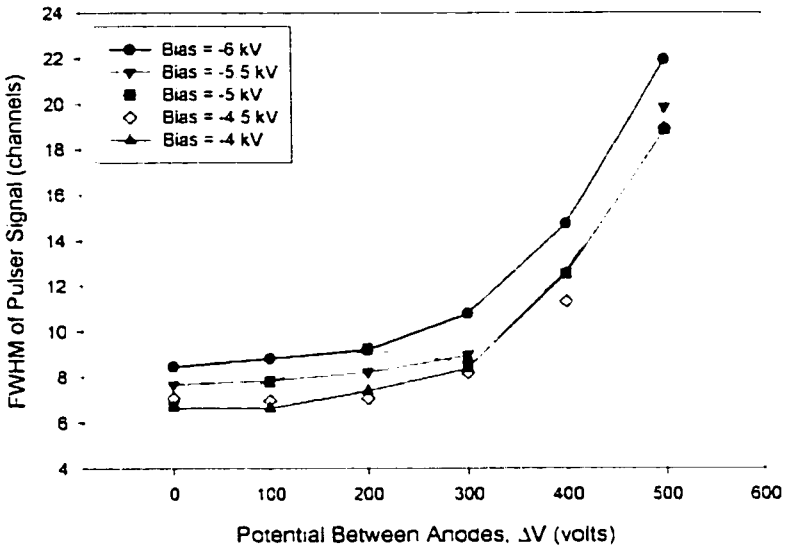

Figure 6.7: Measurement of the electronic noise of the parallel plate detector as a function of ΔV for various cathode biases.

shown in Figures 6.7 and 6.8. As is shown in the figures, there is very little change in the noise as a function of cathode bias, which agrees with the same data from the helical detector. This indicates again, as expected, that the contribution due to bulk leakage current is very small. However, unlike the case with the helical detector, when the surface leakage component was measured a very clear rise in the electronic noise is observed for cases where ΔV was greater than 300 V. At lower values of ΔV, the noise remains dominated by detector capacitance and the small contribution of bulk leakage current. This indicates that for larger values of ΔV, the surface leakage current begins to dominate. This is not entirely unexpected considering this anode is constructed of alumina. As previously stated, the bulk resistivity of alumina is approximately $10^{14}\Omega$·cm whereas Macor, used in the helical detector, has a bulk resistivity of $10^{17}\Omega$·cm. If this is indeed a problem of surface leakage current, it would be expected that using a higher resistivity ceramic should decrease the noise.

The contribution of detector capacitance on the electronic noise was measured to be 7.84 channels, providing a baseline to the subsequent measures of the bulk

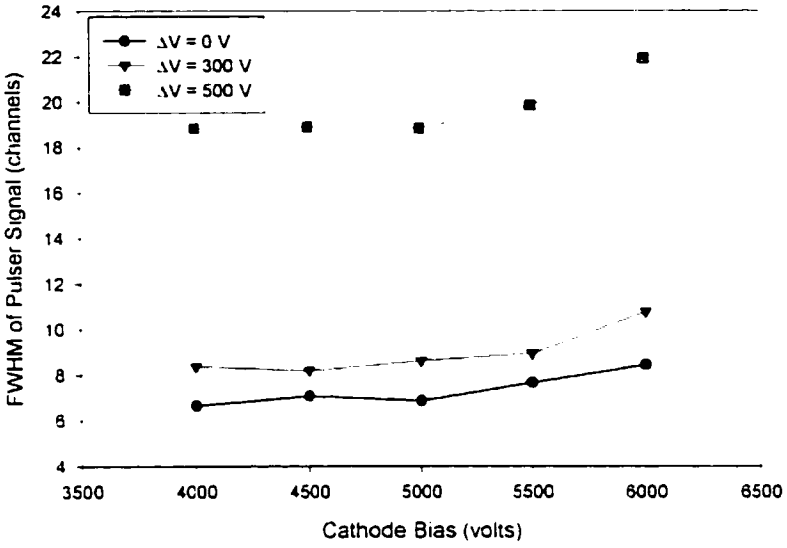

Figure 6.8: Measurement of the electronic noise of the parallel plate detector as a function of cathode bias for various values of ΔV.

and surface leakage current. The capacitance between each measurable structure is shown in Table 6.1.

As shown in the table, the largest contribution to the overall capacitance is the anode-anode capacitance, which contributes approximately 62 pF. However, the boundary electrode-pressure vessel capacitance is also large. This is an important measurement based on the area of the boundary electrode, which is much smaller than any other electrode within the detector. Since it is so small, the major-

Table 6.1: Measurements of the various capacitances of the parallel plate detector (all units in pF)

	Anode 1	Boundary Electrode	Anode 2	Cathode	Pressure Vessel
Anode 1	–	38.2±0.5	61.33±0.01	30.73±0.01	57±2
Boundary Electrode	38.9±0.5	–	38.2±0.1	30.1±0.1	47±1
Anode 2	62.38±0.01	38.17±0.01	–	30.98±0.01	50.3±0.5
Cathode	30.69±0.01	30.05±0.01	30.90±0.01	–	45±2
Pressure Vessel	58±1	46.7±0.5	50±1	44.8±0.5	–

ity of the capacitance in this measurement is not originating between its area and the pressure vessel, but the wires and connectors it attaches to. These will have some capacitance with the surrounding structure, however the exact values of the wire-pressure vessel and connector-pressure vessel capacitances could not be determined at the time of the measurement as it would require opening the sealed pressure vessel. This measurement does indicate, however, that there is significant coupling between the wires and connectors and the vessel itself.

It is also important to consider the other large capacitances measured here, such as the anode-pressure vessel capacitance. The three largest capacitances in the detector are the anode-anode, anode-pressure vessel, and boundary electrode-pressure vessel capacitances. These values will add as parallel capacitance on the input to the preamplifiers as shown in Figure 6.9. Considering only the contributions of these three values, the equivalent input capacitance is approximately 166 pF. This is a very large value for a radiation detector relying on the measurement of small signals and can be a serious limiting factor to its operation. However, based on the specifications of the preamplifiers used for this work, the resulting noise from a 166 pF input capacitance is approximately 30 keV, so this noise level is not unexpected.

To aid in future designs of the coplanar high pressure xenon detectors, it is important to determine the relative influences on the photopeak broadening from the electronic noise, detector capacitance, and leakage current. If the broadening is considered to be a function of only these three components, the contribution of each can be calculated using

$$\sigma_{total}^2 = \sigma_{elec}^2 + \sigma_{det}^2 \tag{6.2}$$

where σ_{total} is the total measured noise, σ_{elec} is the electronic noise, and σ_{det} is the contribution from the detector. For a cathode bias of -3 kV and ΔV = 300 V, the total noise measured was 17.83 channels and the contribution of electronic noise was measured to be 13.77 channels. Based on this, the contribution from the detector, such as from capacitance and leakage current, was calculated to be 11.48 channels.

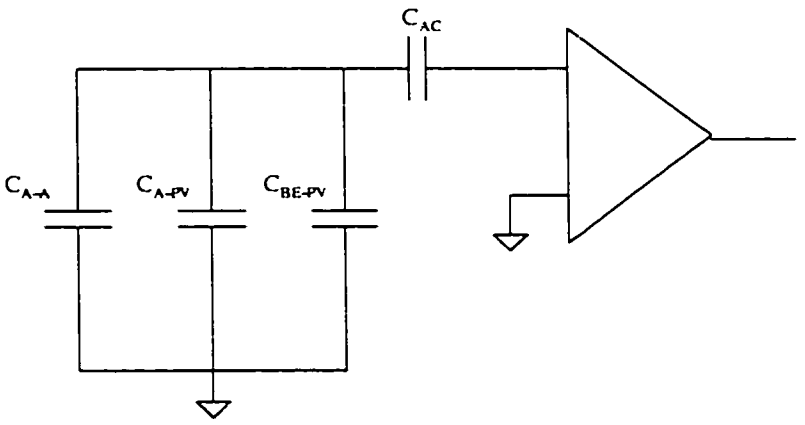

Figure 6.9: Schematic of the electronic circuit equivalent of the various detector capacitances. Here, C_{A-A} is the anode-anode capacitance, C_{A-PV} is the anode-pressure vessel capacitance, and C_{BE-PV} is the boundary electrode-pressure vessel capacitance.

Table 6.2: Calculated contributions to the broadening of the photopeak with a cathode bias of -3 kV and $\Delta V = 300V$

Total measured noise	64.7 keV
Overall noise from detector	53.9 keV
Contribution from capacitance	36.8 keV
Contribution from leakage current	39.4 keV

If this is further broken down into the contribution of surface leakage current, σ_i, and detector capacitance, σ_C, the contribution of the leakage current on the signal can be calculated with

$$\sigma_{det}^2 = \sigma_C^2 + \sigma_i^2. \tag{6.3}$$

Using equation 6.3, the surface leakage current was calculated to have contributed 8.39 channels to the measured noise at these bias conditions. The results of this measurement are summarized in Table 6.2.

It is clear from these results that there are things that can be modified to improve the noise performance in future designs. First, as previously stated, using a ceramic with a higher bulk resistivity would decrease the observed effects from surface leakage current, particularly at higher values of ΔV. It is also clear that a future design needs to minimize the capacitive component. One way this could be done is by reducing the wire length between the anode and the high voltage feed-throughs. Finally, it is clear that with the parallel plate detector, as was true with the helical detector, that the electronic noise is too high. Future work with high pressure xenon detectors should investigate the use of different preamplifiers that are more suited to the small pulses of xenon.

6.5 Contribution of Electron Recombination on the Observed Spectra

As described in the previous section, one of the contributions to the broadening of the photopeak is the surface leakage current, which begins to dominate at values of ΔV greater than 300 V. This is problematic because it was only for values around

300 V with a cathode bias of -4 kV that coplanar pulses were observed nearly 100% of the time. As such, while the detector might be operating in the coplanar regime, the benefits of doing so are lost to the leakage current problem. However, if the detector could be operated at a lower bias such that a lower ΔV would be required for complete electron collection on the collecting anode, it could minimize this problem. However, as previously stated, high pressure xenon detectors are usually operated at drift fields greater than 2 kV/cm to minimize the effects of electron recombination. Hence, it was important to determine what minimum cathode bias was necessary to prevent charge trapping within the gas.

An experiment was performed where spectra were taken for various cathode biases with ΔV at a constant 300 V. These results are presented in Figure 6.10. There are several pieces of important information that can be obtained from this figure. First, it is clear that a photopeak is not present, even with a sufficient ΔV for a cathode bias of -1.5 kV. As the bias is increased, the photopeak clearly begins to form and its centroid channel location increases. The presence of the photopeak indicates that at least a significant percentage of the electrons are being collected by the collecting anode. The shift in position indicates the presence of electron recombination, an effect that will decrease with increasing cathode bias. The FWHM of the photopeak improves from 17.08% at a bias of -2.5 kV to 12.35% for a bias of -3.5 kV. However, for a bias of -4 kV, the photopeak has degraded to a FWHM of 14.84%. This is due to the fact that at this bias ΔV is not quite sufficient to collect all of the electrons on the collecting anode at this higher cathode bias. This same measurement was repeated for the case where ΔV = 400 V, as shown in Figure 6.11. In this data, it is clear that the quality of the photopeak again improves with increases in ΔV where the resolution improves from 15.76% at a bias of -2.5 kV to 12.67% at a bias of -3 kV. In this case, at a cathode bias of -4 kV, the photopeak resolution has improved relative to the data for the -3 kV bias. However, there is still a slight degradation relative to the spectra at lower biases. The resolutions are worse for larger cathode biases such as -4 kV since, even with ΔV = 400 V, this is not sufficient to collect all of the electrons on the collecting anode so the detector is

Table 6.3: Summary of data from ^{137}Cs spectra for the parallel plate detector as a function of cathode bias and ΔV.

Cathode Bias (kV)	ΔV (V)	Photopeak Centroid Channel	Photopeak FWHM (channels)
-2.0	300	120.3	20.5 (17.1%)
-2.5	300	130.3	17.6 (13.5%)
-3.0	300	134.0	18.0 (13.4%)
-3.5	300	134.6	16.6 (12.4%)
-4.0	300	138.3	20.5 (14.8%)
-2.0	400	121.6	23.8 (19.5%)
-2.5	400	131.2	20.7 (15.8%)
-3.0	400	136.0	17.2 (12.7%)
-3.5	400	136.6	19.8 (14.5%)
-4.0	400	138.2	20.5 (14.8%)

not quite operating in coplanar mode. These results are summarized in Table 6.3.

In order to quantify the effect of cathode bias on electron recombination, the photopeak centroid channel was obtained for both cases where ΔV = 300 and 400 V. These results are shown in Figure 6.12. For cathode biases greater than -3 kV (or a drift field greater than 1 kV/cm), the photopeak centroid does not change significantly. Previous work in high pressure xenon reported that a drift field of 2 kV/cm was required to observe no degradation in the photopeak centroid, so the purity of the gas is quite high. Hence the detector can be operated with a cathode bias this low without significant loss of charge between the cathode and anode. Operating at a cathode bias of -3 kV would require ΔV = 174 V.

6.6 Contribution of Charge Sharing Between the Anodes

The above results demonstrate the effect of cathode bias on the centroid position of the photopeak. However, this does not quantify the coplanar pulses to indicate their quality with respect to the percentage of the events that are truly coplanar pulses. For events that are truly coplanar, there should be no collection of electrons on the non-collecting anode. By simple analysis of the spectra, it is not easy to determine what percentage of photopeak events truly have complete charge

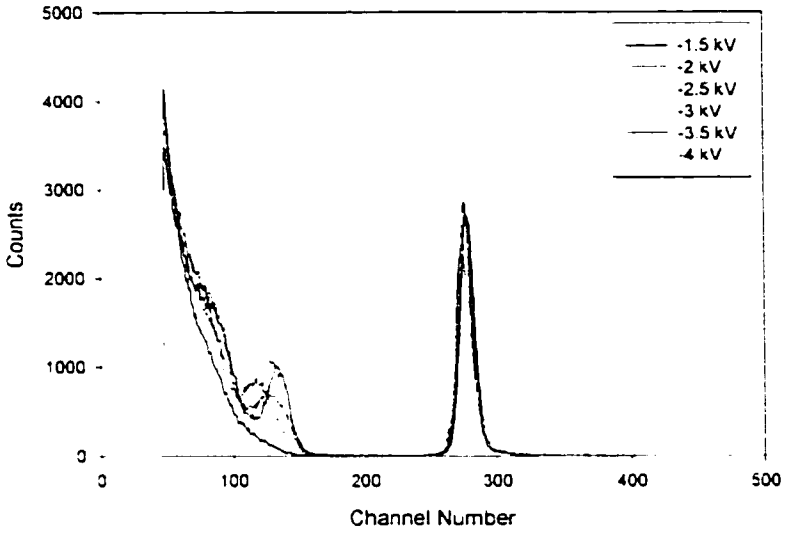

Figure 6.10: ^{137}Cs spectra with ΔV = 300 V for various cathode biases.

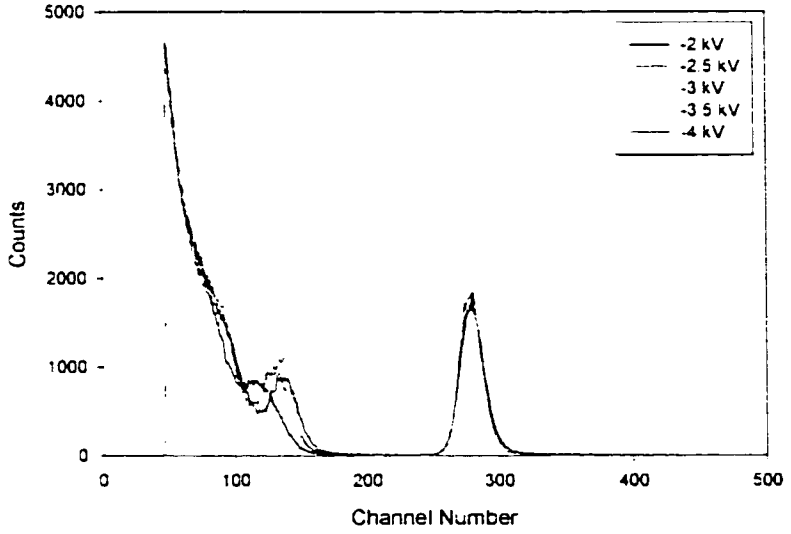

Figure 6.11: ^{137}Cs spectra with ΔV = 400 V for various cathode biases.

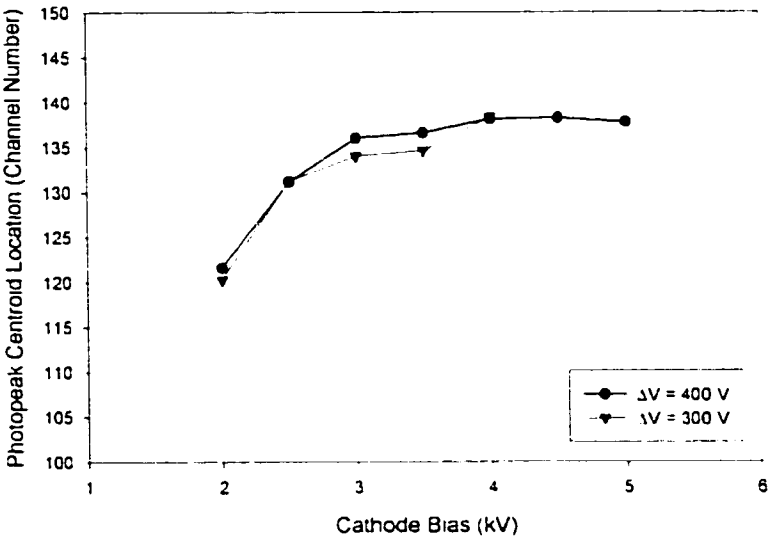

Figure 6.12: Results demonstrating the effect of electron trapping as a function of cathode bias.

collection on the non-collecting anode. If even 10% of the electrons created in photopeak events are shared by the non-collecting anode, this can result in a variation of pulse height through the subtraction circuit of 20%, which can provide a major source of photopeak broadening.

In order to ascertain the contribution of charge sharing and determine the quality of coplanar operation of the parallel plate detector, an experiment was conducted examining the subtracted and added signal from the preamplifiers. While the weighting potential for a coplanar detector has been shown in Figure 2.7, the signal resulting from the addition of the collecting and non-collecting anodes provides information on the depth of interaction. The weighting potential for this case is shown in Figure 6.13. For events originating near the cathode, the subtracted and added signal should be nearly identical. However, for events originating elsewhere in the detector, the signal of the subtraction circuit should be the same, but the added signal will be decreased by an amplitude proportional to the distance from the anode that the event originated.

Using this information, pulses were examined at a cathode bias of -3 kV and

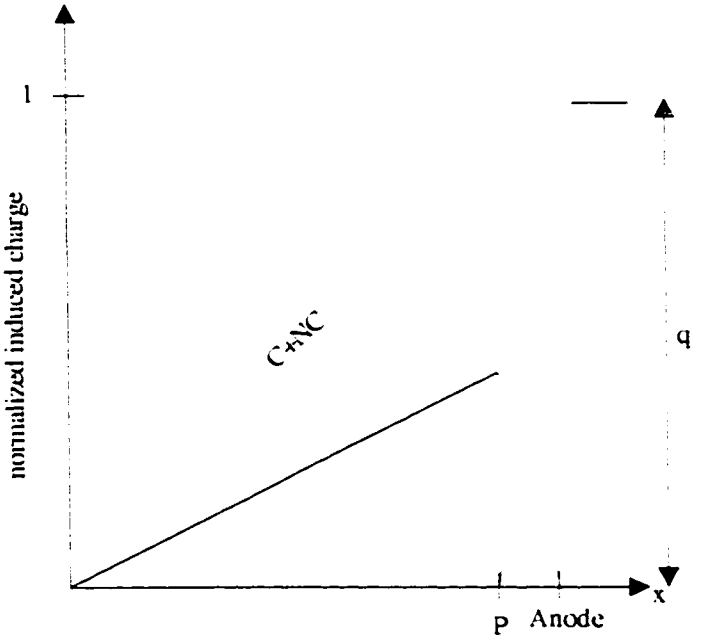

Figure 6.13: Weighting potential of the coplanar anode detector. The additional purple line indicates the summed weighting potential of the collecting and non-collecting anodes. P is the depth one pitch width from the anode surface.

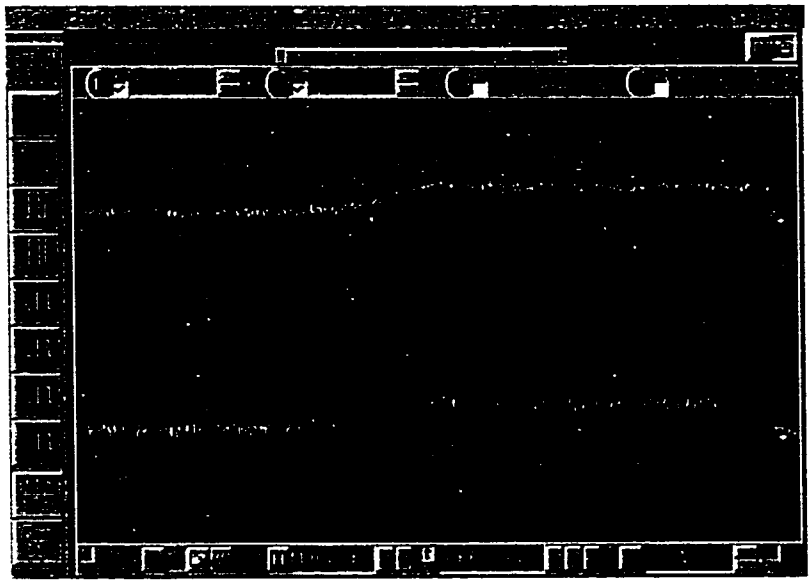

Figure 6.14: Sample pulse waveforms used to determine variations in the shaped pulse amplitude.

ΔV = 300 V. The output of the subtraction circuit was input to the shaping amplifier, which was used to trigger the oscilloscope. The trigger was set high enough to only include full-energy events. Events originating near the cathode were examined, which were identified by rise times greater than approximately 25 μs. Any difference between the subtracted and added signal here would indicate the severity of charge sharing between the anodes. A sample event from this experiment is shown in Figure 6.14 where the yellow trace is the collecting anode signal, the green is the non-collecting anode, the purple is a mathematical addition of the two signals, and the pink is a mathematical subtraction of the two signals. The results from this experiment are presented in Figure 6.15.

By inspecting the pulse waveforms such as those shown in Figure 6.14, there were observed instances where the added and subtracted signals of events originating near the cathode differed by about 1 mV of the total 5 mV expected pulse amplitude. However, for interactions near the cathode, the added and subtracted signal should be identical. This poses an additional source of deviation in the pulse amplitude of the shaped pulse for events that are considered to be full en-

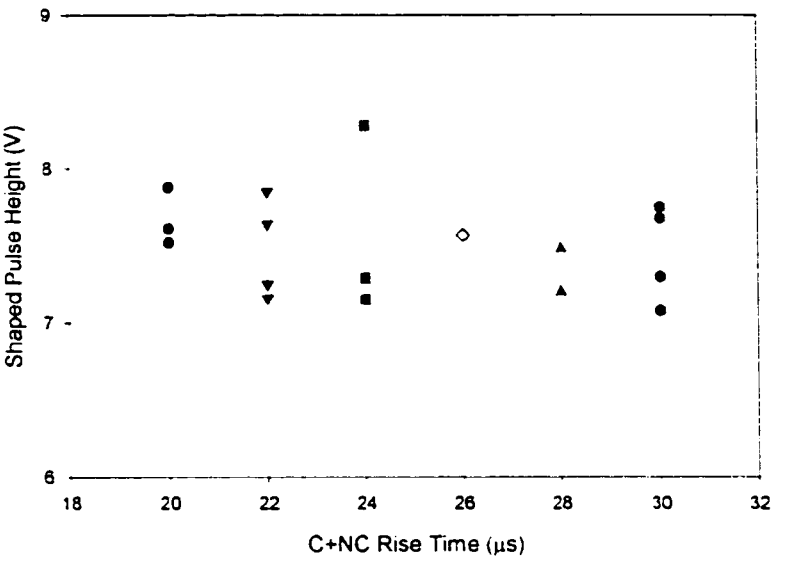

Figure 6.15: Pulse amplitudes for a series of pulses originating near the cathode.

ergy events. For pulses with a rise time of 30 μs, the average pulse amplitude from the shaping amplifier was 7.45 V. However, the data with the largest spread in this set exhibit a variation in this amplitude of 5.0%. Maximum variations of 5.02% and 9.34% were obtained for pulses with rise times of 22 and 24 μs respectively. This large variation suggests that, even with ΔV = 300 V, the detector is not quite operating in coplanar mode. However, this measurement was based on manual observations using the oscilloscope. Further measurements should be performed using a system that could collect and analyze thousands of pulses to more accurately determine these values. This measurement will have large errors associated with it based on the fact that so few pulse waveforms were analyzed, however it provides an indication that this could be a problem and should be further investigated.

6.7 Conclusions about the Parallel Plate Detector

The parallel plate detector, once the electrodes were properly connected, exhibited results that indicate the coplanar anode technique can work in high pressure

xenon. Coplanar pulses were observed 100% of the time at ΔV = 240 V with a cathode bias of -4 kV, which did not differ significantly from the calculated value of ΔV_{min} = 232 V. The spectroscopic results, while not very good, demonstrated that the coplanar technique is an improvement over the classical ionization chamber mode for this detector. However, many limitations to optimal operation were discovered that resulted in very broad photopeaks.

The first and most obvious source of resolution degradation was due to electronic noise. It was demonstrated that, at values of ΔV required for coplanar mode operation, the surface noise is too high. One possible source of this is from surface leakage current, a problem that is easily overcome in future detectors simply by metalizing the anode pattern onto a different ceramic with a higher bulk resistivity.

Another problem was discovered when the detector capacitance was measured. It was determined that this was dominated by the anode-anode, anode-pressure vessel, and boundary electrode-pressure vessel capacitances. These three components contributed 166 pF of input capacitance, which can be reduced in future designs by changes in the structure of the pressure vessel. Such changes, to name a few, could involve increasing the distance between the anodes, using shorter wires to connect the electrodes to the feedthroughs, and increasing the separation between the anode and the pressure vessel.

Lastly, the values of ΔV used were not quite large enough for complete charge collection on the collecting anode. However, if ΔV was increased to get to this region, the surface leakage current would begin to dominate the energy resolution. If the anode structure was made out of a higher resistivity ceramic, it would be possible to further increase ΔV and an improvement in the resolution would be expected.

Despite all of the limitations of this detector, the principle of single polarity charge sensing using a coplanar anode in high pressure xenon has been demonstrated.

Chapter 7

CONCLUSIONS AND FUTURE WORK

Based on the results presented, it is clear that there were several limitations for each detector. In the case of the helical detector, some problems prevented it from operating in coplanar mode, although the source is not clear. Work was abandoned on this detector in order to determine whether a coplanar anode high pressure xenon detector was possible. The parallel plate detector, on the other hand, was able to operate in coplanar anode mode, however its spectroscopic performance was quite poor.

As previously stated, although the helical detector never attained coplanar mode operation, none of the experiments performed suggested that it should not be able to work. ΔV was set to the values predicted by both the Coulomb simulations and the numerical calcuations, and even at several times these values no coplanar pulses were observed.

One key problem was discovered in the early stages of the work concerning the size of the anode wires. Significant spectroscopic improvement was observed when the size of the wires was increased so that they protruded from the support groove. This was explained using the technique of mirror charges and it was demonstrated that it is quite important that the anodes have a direct line-of-sight to each other so the non-collecting anode can return to a state of zero induced charge as a result of the electrostatic neutrality obtained between the true charge and the mirror charge when the electron is close to the surface of the collecting anode.

Several experiments were performed to determine the source of the coplanar mode failure. The possibility of mutual inductance on the anode wires was eliminated by examining the induced signal on each. The distortion of the field by the

build-up of charges on the surface of the anode rod was considered. A calculation was performed using Coulomb to ascertain what surface charge density would be required to distort the field enough that the non-collecting anode would be at a local maximum in potential. This possibility was eliminated since the surface charge necessary would create a potential on the order of magnitude of the cathode bias voltage. Lastly, the IV curves of the helical detector were obtained. As demonstrated in this experiment, the detector appeared to be moving towards coplanar mode operation at value of ΔV around 1000 V, however this was not supported by analysis of the pulse waveform. Additionally, the quality of the photopeak did not improve at these values as expected.

One obvious area remaining for experimentation lies in further improvements to the anode rod. It is clear that the initial wires were not large enough since there was noted improvement in the spectrum when their size was increased. However, it is not clear that the new wires were large enough either. In order to ascertain this, the pressure vessel should be opened and the wires should be inspected again. Replacing them with larger wires could offer further improvements to the spectra. Additionally, the technique of ceramic metalization, which was successfully demonstrated with the parallel plate detector, should be considered for future anode rods. Should this approach be used, care should be taken so the anode-anode capacitance does not dramatically increase, as was true for the parallel plate detector. This would also allow trial of other anode configurations, such as parallel strips running length-wise down the rod. In this case the calculated field is much easier to characterize.

The parallel plate detector was capable of coplanar mode operation near the predicted value of ΔV_{min} once the problem of the poor connection of one of the anodes was eliminated. With ΔV set sufficient for coplanar mode operation, spectra were obtained for this detector indicating an electronic noise problem. The best resolution obtained was 84 keV (12.7%) for 662 keV gamma rays.

Emphasis was placed in determining the various contributions to the photopeak broadening. It was determined that leakage current across the surface of

the anodes was a problem for values of ΔV greater than approximately 300 V. Unfortunately, this corresponded to the potential where the coplanar mode was observed. For a cathode bias of -3 kV and ΔV = 300 V, the surface leakage current contributed 39.4 keV of noise. This could be minimized in future designs by constructing the anode using a higher resistivity ceramic. The contribution due to detector capacitance was determined to be 36.8 keV, which was largely dominated by the anode-anode, anode-pressure vessel, and boundary electrode-pressure vessel capacitances. These three values resulted in a 166 pF input capacitance. This could also be minimized in future designs by shortening the electrode wires between the anode surface and the high voltage feedthroughs.

In an attempt to run the detector at a lower bias thus requiring a smaller value of ΔV (and thus a smaller contribution due to surface leakage current), the effect of electron recombination as a function of cathode bias was examined. It was observed that there was little movement in the centroid of the photopeak for biases greater than -3 kV. However, even with ΔV = 300 V, significant variations were observed on the subtracted signal of the two anodes for cases where the electrons originated near the cathode. This was due to charge sharing on the non-collecting anode due to insufficient ΔV. The variations on the pulse height of photopeak events originating near the cathode was approximately 5% for a cathode bias of -3 kV and ΔV = 300 V. This also could be due to the fact that the width of the strips was rather large resulting in a region beneath the collecting anode of low electric field where the electrons may not fully be collected.

Further diagnosis would have been possible with the both detectors if it the pulse height as a function of interaction position could be controlled by the use of a collimated source. However, in order to properly use this technique to map the detector response for the helical detector, it would be necessary to introduce the gamma ray through the end caps of the pressure vessel since side-illumination would not provide control over the interaction location in the radial coordinate. However, the end cap for this pressure vessel is approximately one inch thick of stainless steel, which would attenuate the gamma rays too much, even at higher

energies. The same technique was also not possible with the parallel plate detector due to the cylindrical shell of dead xenon around the active region of the detector. Attenuation in this region would result in gamma ray energies in the detection region that were not uniform. This can be done in future designs if this dead region is eliminated, either by the construction of a new pressure vessel or by the introduction of a cylindrical shell of ceramic to keep all of the xenon between the anode and cathode.

The parallel plate detector demonstrated that the technique of single polarity charge sensing with coplanar anodes in high pressure xenon can work, however many modifications should be made in order to obtain better energy resolutions. First, a larger anode should be built to increase the efficiency of the detector. However, emphasis should be placed on reducing the capacitance, especially the anode-anode capacitance, which will increase with anode size. A pressure vessel should be specifically designed for this anode to minimize both the region of dead xenon around the active region and to reduce the effects of detector capacitance. The anode itself should be constructed of a high resistivity ceramic and consideration should be made to changing the strip width to minimize the possibility of electrons recombining in a region of lower electric field such as beneath the non-collecting anode.

References

1. E. Aprile, A. Bolotnikov, D. Chen, R. Mukherjee, F. Xu, D.F. Anderson, and V. Peskov. Performance of CsI photocathodes in liquid Xe, Kr, and Ar. *Nuclear Instruments and Methods in Physics Research A*, 338:328–335, 1994.

2. E. Aprile, A. Bolotnikov, D. Chen, F. Xu, and V. Peskov. First observation of the scintillation light from solid Xe, Kr, and Ar with a CsI photocathode. *Nuclear Instruments and Methods in Physics Research A*, 353:55–58, 1994.

3. E. Aprile, V. Egorov, K.L. Giboni, T. Kozu, F. Xu, T. Doke, J. Kikuchi, T. Kashiwagi, G.J. Fishman, R. Rehage, and D. Trice. The electronics read out and data acquisition system for a liquid xenon time projection chamber as a balloon-borne Compton telescope. *Nuclear Instruments and Methods in Physics Research A*, 412:425–436, 1998.

4. G. Arfken. *Mathematical Methods for Physicists*. Academic Press, Inc., New York, NY, second edition, 1968.

5. A. Athanasiades, J.L. Lacy, C.S. Martin, R.A. Austin, N.N. Shehad, and L. Sun. Position sensing in a cylindrical ionization detector with a resistive cathode. *Nuclear Instruments and Methods in Physics Research A*, in publication.

6. E.A. Babichev, S.E. Baru, V.R. Groshev, A.G. Khabakhpashev, G.S. Krainov, V.V. Leonov, V.A. Neustroev, V.V. Porosev, G.A. Savinov, and L.I. Shekhtman. Usage of two types of high-pressure xenon chambers for medical radiography. *Nuclear Instruments and Methods in Physics Research A*, 461:430–434, 2001.

7. J.E. Baciak and Z. He. Comparison of 5 mm and 10 mm thick hgI_2 pixelated gamma-ray spectrometers. *Nuclear Instruments and Methods in Physics Research A*, in publication.

8. J.E. Baciak, Z. He, and R.P. DeVito. Electron trapping variations in single-crystal pixelated hgI_2 gamma-ray spectrometers. *IEEE Transactions on Nuclear Science*, 49(3), 2002.

9. H.H. Barret, J.D. Eskin, and H.B. Barber. Charge transport in arrays of semiconductor gamma-ray detectors. *Physical Review Letters*, 75(1):156–159, 1995.

10. M.R. Bishai, E.K.E. Gerndt, I.P.J. Shipsey, A.V. Bagulya, V.M. Grishin, M.A. Negodaev, and V. Ligachev. Micro strip gas chambers overcoated with carbon, hydrogenated amorphous silicon, and glass films. *Nuclear Instruments and Methods in Physics Research A*, 400:233–242, 1997.

11. M.R. Bishai, E.K.E. Gerndt, I.P.J. Shipsey, P.N. Wang, A.V. Bagulya, V.M. Grishin, M.A. Negodaev, and P. Geltenbort. Performance of microstrip gas chambers passivated by thin semiconducting glass and plastic films. *Nuclear Instruments and Methods in Physics Research A*, 365:54–58, 1995.

12. M. L. Boas. *Mathematical Methods in the Physical Sciences*. John Wiley and Sons, Inc., New York, NY, 1966.

13. B. Boimska, R. Bouclier, M. Capeans, W. Dominik, G. Million, L. Ropelewski, F. Sauli, A. Sharma, and T. Temmel-Ropelewski. Progress with diamond over-coated microstrip gas chambers. *Nuclear Instruments and Methods in Physics Research A*, 404:57–70, 1998.

14. A. Bolotnikov and B. Ramsey. Purification techniques and purity and density measurements of high-pressure Xe. *Nuclear Instruments and Methods in Physics Research A*, 383:619–623, 1996.

15. A. Bolotnikov and B. Ramsey. Improving the energy resolution of high-pressure Xe cylindrical ionization chambers. *IEEE Transactions on Nuclear Science*, 44(3):1006–1010, 1997.

16. A. Bolotnikov and B. Ramsey. The spectroscopic properties of high-pressure xenon. *Nuclear Instruments and Methods in Physics Research A*, 396:360–370, 1997.

17. A. Bolotnikov and B. Ramsey. Studies of light and charge produced by alpha-particles in high-pressure xenon. *Nuclear Instruments and Methods in Physics Research A*, 428:391–402, 1999.

18. A. E. Bolotnikov, I. V. Chernycheva, V. V. Dmitrenko, A. M. Galper, V. M. Gratchev, O. N. Kondakova, S. V. Krivov, V. I. Lyagushin, G. A. Shmatov, S. I. Sutchkov, S. E. Ulin, Z. M. Uteshev, K. F. Vlasik, and Yu. T. Yurkin. Observation of gamma-ray lines with high pressure xenon spectrometer on board of the orbital station "MIR" in the gamma-ray burst 20 Dec 1990. *Proceedings of the 23rd International Cosmic Ray Conference*, 1, 1993.

19. A. E. Bolotnikov, V. V. Dmitrenko, A. S. Romanyuk, S. I. Suchkov, and Z. M. Uteschev. Factors determining energy resolution of compressed-xenon gamma ray spectrometers at densities of >0.6 g/cm3. *Pribory i Tekhnika Eksperimenta*, 4:42–45, 1984.

20. A. Bolozdynya, V. Egorov, A. Koutchenkov, G. Safronov, G. Smirnov, S. Medved, and V. Morgunov. A high pressure xenon self-triggered scintillation drift chamber with 3D sensitivity in the range of 20–140 keV deposited energy. *Nuclear Instruments and Methods in Physics Research A*, 385:225–238, 1997.

21. F.I.G.M. Borges, J.M.F. dos Santos, T.H.V.T. Dias, F.P. Santos, P.J.B.M. Rachinhas, and C.A.N. Conde. Operation of gas proportional scintillation counters in a low charge multiplication regime. *Nuclear Instruments and Methods in Physics Research A*, 422:321–325, 1999.

22. R. Bouclier, M. Capeans, G. Million, L. Ropelewski, F. Sauli, T. Temmel, R.A. Cooke, S. Donnel, S.A. Sastri, and N. Sonderer. High rate operation of microstrip gas chambers of diamond-coated glass. *Nuclear Instruments and Methods in Physics Research A*, 369:328–331, 1996.

23. R. Bouclier, C. Garabatos, G. Manzin, F. Sauli, L. Shektman, T. Temmel, G. Della Mea, G. Maggioni, V. Rigato, and I. Logachenko. Development of microstrip gas chambers on substrata with electronic conductivity. *IEEE Transactions on Nuclear Science*, 41(4):821–825, 1994.

24. R. Bouclier, G. Million, L. Ropelewski, F. Sauli, Yu.N. Pestov, and L.I. Shekhtman. Performance of gas microstrip chambers on glass substrata with electronic conductivity. *Nuclear Instruments and Methods in Physics Research A*, 332:100–106, 1993.

25. H. Brauning, A. Breskin, R. Chechik, V. Dangendorf, A. Demian, K. Ullmann, and H. Schmidt-Brocking. A large volume 3D imaging gas scintillation counter with CsI-based wire chamber readout. *Nuclear Instruments and Methods in Physics Research A*, 348:223–227, 1994.

26. CERN European Organization for Nuclear Research. *Geant4 User's Guide for Application Developers*, 4.4.1 edition, 2002.

27. H.S. Cho, W.S. Hong, J. Kadyk, V. Perez-Mendez, J.G. Kim, and J. Vujic. Performance of microstrip gas chambers with conductive surface coating of doped amorphous silicon carbide (a-Si:C:H). *Nuclear Instruments and Methods in Physics Research A*, 401:81–88, 1997.

28. Coulomb. *Integrated Engineering Software, Inc.* Winnipeg, Manitoba, Canada, 1998.

29. T.H.V.T. Dias, J.M.F. dos Santos, P.J.B.M. Rachinhas, F.P. Santos, and C.A.N. Conde. Full-energy absorption of x-ray energies near the Xe L- and K-photoionization thresholds in xenon gas detectors: simulation and experimental results. *Journal of Applied Physics*, 82(6):2742–2753, 1997.

30. T.H.V.T. Dias, F.P. Santos, and C.A.N. Conde. The primary electron cloud in xenon for x-rays in the 0.1 to 10 keV energy range. *Nuclear Instruments and Methods in Physics Research A*, 310:137–139, 1991.

31. T.H.V.T. Dias, F.P. Santos, J.M.F. dos Santos, J.A.M. Lopes, J.F.C.A. Veloso, P.J.B.M. Rachinhas, R.E. Morgado, A.D. Stauffer, and C.A.N. Conde. The response of xenon x-ray detectors to full-energy absorption and fluorescence-escape events: measurement and modelling. *IEEE Transactions on Nuclear Science*, 43(3):1432–1441, 1996.

32. T.H.V.T. Dias, F.P. Santos, P.J.B.M. Rachinhas, F.I.G.M. Borges, J.M.F. dos Santos, and C.A.N. Conde. Xenon-neon gas proportional scintillation counters: experimental and simulation results. *Journal of Applied Physics*, 85(9):6303–6312, 1999.

33. T.H.V.T. Dias, F.P. Santos, A.D. Stauffer, and C.A.N. Conde. The Fano factor in gaseous xenon: a Monte Carlo calculation for x-rays in the 0.1 to 25 keV energy range. *Nuclear Instruments and Methods in Physics Research A*, 307:341–346, 1991.

34. V.V. Dmitrenko, I.V. Chernyhsheva, V.M. Gratchev, O.N. Kondakova, K.V. Krivova nd S.E. Ulin, Z.M. Uteshev, and K.F. Vlasik. Vibrostability of high pressure xenon gamma-ray detectors. *IEEE Transactions on Nuclear Science*, 47(3):939–943, 2000.

35. V.V. Dmitrenko, A.G. Dvornyak, V.M. Gratchev, O.N. Kondadova, K.V. Krivova, A.Yu Papchenko, D.V. Sokolov, S.E. Ulin, Z.M. Uteshev, and K.F. Vlasik. A thermostable high pressure xenon gamma-ray detector for monitoring concentration of KCl during fertilizer manufacturing. *Nuclear Instruments and Methods in Physics Research A*, 422:326–330, 1999.

36. V.V. Dmitrenko, V.M. Gratchev, S.E. Ulin, Z.M. Uteshev, and K.F. Vlasik. High-pressure xenon detectors for gamma-ray spectrometry. *Applied Radiation and Isotopes*, 52:739–743, 2000.

37. V.V. Dmitrenko, V.N. Levedenko, A.S. Romanuk, and Z.M. Uteshev. Cylindrical ionization chamber for low-energy gamma-ray spectrometry (0.1–3MeV). *Instruments and Experimental Techniques*, N5:49–51, 1981.

38. V.V. Dmitrenko, V.N. Levedenko, Z.M. Uteshev, and V.K. Chernyatin. Spectrometric capabilities of drift ionization chamber. *Instruments and Experimental Techniques*, N1:51–53, 1982.

39. J.M.F. dos Santos, R.E. Morgado, L.M.N. Tavora, and C.A.N. Conde. The energy nonlinearity of a xenon gas proportional scintillation counter at the K-absorption edge in xenon. *Nuclear Instruments and Methods in Physics Research A*, 350:216–220, 1994.

40. J.M.F. dos Santos, J.F.C.A. Veloso, R.E. Morgado, and C.A.N. Conde. The performance of a compact gas proportional scintillation counter for hard x-ray spectrometry. *Nuclear Instruments and Methods in Physics Research A*, 353:195–200, 1994.

41. P. C. Dunn. *Gateways into Electronics*. John Wiley and Sons, Inc., New York, NY, 2000.

42. J. Engler, D. Moucka, and J. Wochele. Glow discharge cleaning of stainless steel surfaces for ionization chambers. *Nuclear Instruments and Methods in Physics Research B*, 100:183–187, 1995.

43. R. Fang, R. Blaes, J.M. Brom, W. Geist, A. Michalon, J.L. Riester, and C. Voltolini. Charge accumulation at the interface between two dielectrics and gas gain variation of microstrip gas chambers. *Nuclear Instruments and Methods in Physics Research A*, 365:59–64, 1995.

44. R. Fang, W. Geist, J.M. Brom, A. Bergdolt, and J.L. Riester. Gain stability of microstrip gas chambers with high resistivity substrates. *Nuclear Instruments and Methods in Physics Research A*, 378:439–442, 1996.

45. W.G. Gong, H. Wieman, J.W. Harris, J.T. Mitchell, W.S. Hong, and V. Perez-Mendez. Microstrip gas chambers on glass and ceramic substrates. *IEEE Transactions on Nuclear Science*, 41(4):890–897, 1994.

46. D. J. Griffiths. *Introduction to Electrodynamics*. Prentice Hall, Englewood Cliffs, NJ, second edition, 1989.

47. Z. He. Potential distribution within semiconductor detectors using coplanar electrodes. *Nuclear Instruments and Methods in Physics Research A*, 365:572–575, 1995.

48. Z. He. Review of the Shockley-Ramo theorem and its applications in semiconductor gamma-ray detectors. *Nuclear Instruments and Methods in Physics Research A*, 463:250–267, 2001.

49. Z. He and M.H. Khachaturian. Analytical derivation of critical bias voltage for complete electron collection in 2D radial room temperature semiconductors using alternating electrodes. To be published, 2002.

50. Z. He, G. F. Knoll, D. K. Wehe, R. Rojeski, C. H. Mastrangelo, M. Hammig, C. Barrett, and A. Uritani. 1-D position sensitive single carrier semiconductor detectors. *Nuclear Instruments and Methods in Physics Research A*, 380:228–231, 1996.

51. Z. He, G.F. Knoll, D.K. Wehe, and Y.F. Du. Coplanar grid patterns and their effect on energy resolution of CdZnTe detectors. *Nuclear Instruments and Methods in Physics Research A*, 411:107–113, 1998.

52. Z. He, G.F. Knoll, D.K. Wehe, and J. Miyamoto. Position-sensitive single carrier CdZnTe detectors. *Nuclear Instruments and Methods in Physics Research A*, 388:180–185, 1997.

53. Z. He, W. Li, G.F. Knoll, D.K. Wehe, J. Berry, and C.M. Stahle. 3-D position sensitve CdZnTe gamma-ray spectrometers. *Nuclear Instruments and Methods in Physics Research A*, 422:173–178, 1999.

54. Z. He, W. Li, G.F. Knoll, D.K. Wehe, and Y.F. Du. Effects of charge sharing in 3-D position sensitive CdZnTe gamma-ray spectrometers. *Nuclear Instruments and Methods in Physics Research A*, 439:619–624, 2000.

55. Z. He, W. Li, G.F. Knoll, D.K. Wehe, and C.M. Stahle. Measurement of material uniformity using 3-D position sensitive CdZnTe gamma-ray spectrometers. *Nuclear Instruments and Methods in Physics Research A*, 441:459–467, 2000.

56. S. Huang and G. R. Freeman. Electron mobilities in gaseous, critical, and liquid xenon: density, electric field, and temperature effects: quasilocalization. *Journal of Chemistry and Physics*, 68(4):1355–1362, 1978.

57. N. Ishida, M. Chen, T. Doke, K. Hasuike, A. Hitachi, M. Gaudreau, M. Kase, Y. Kawada, J. Kikuchi, T. Komiyama, K. Kuwahara, K. Masuda, H. Okada, Y.H. Qu, M. Suzuki, and T. Takahashi. Attenuation length measurements of scintillation light in liquid rare gases and their mixtures using an improved reflection suppresser. *Nuclear Instruments and Methods in Physics Research A*, 384:380–386, 1997.

58. J. D. Jackson. *Classical Electrodynamics*. John Wiley and Sons, Inc., New York, NY, second edition, 1975.

59. H. Johnson. The real truth about crosstalk. *Electrical Design*, 45:115, 1997.

60. L.T. Jones and P.B. Woollam. Resolution improvement in CdTe gamma detectors using pulse-shape discrimination. *Nuclear Instruments and Methods*, 124:591–595, 1975.

61. B.D. Keele, R.S. Addleman, and G.L. Troyer. A method to improve spectral resolution in planar semiconductor gamma-ray detectors. *IEEE Transactions on Nuclear Science*, 43(3):1365–1368, 1996.

62. R. Kessick and G. Tepper. A hemispheric high-pressure xenon gamma radiation spectrometer. *Nuclear Instruments and Methods in Physics Research A*, 490:243–250, 2002.

63. G. F. Knoll. *Radiation Detection and Measurements*. John Wiley and Sons, Inc., New York, NY, third edition, 2000.

64. R. V. Langmuir. *Electromagnetic Fields and Waves*. McGraw-Hill Book Company, Inc., New York, NY, 1961.

65. C. Levin, J. Germani, and J. Markey. Charge collection and energy resolution studies in compressed xenon gas near its critical point. *Nuclear Instruments and Methods in Physics Research A*, 332:206–214, 1993.

66. M. Li, M.S. Dixit, and P.C. Johns. Photon-counting digital radiography using high-pressure xenon filled detectors. *Nuclear Instruments and Methods in Physics Research A*, 471:215–221, 2001.

67. W. Li. *Three-Dimensional Position Sensitive CdZnTe Gamma Ray Spectrometers*. PhD thesis, University of Michigan, Department of Nuclear Engineering and Radiological Sciences, 2001.

68. D. R. Lide, editor. *Handbook of Chemistry and Physics*. CRC Press LLC, Boca Raton, FL, eighty-second edition, 2001.

69. P.N. Luke. Single-polarity charge sensing in ionization detectors using coplanar electrodes. *Applied Physics Letters*, 65(22):2884–2886, 1994.

70. P.N. Luke. Unipolar charge sensing with coplanar electrodes – application to semiconductor detectors. *IEEE Transactions on Nuclear Science*, 42(4):207–213, 1995.

71. P.N. Luke. Electrode configuration and energy resolution in gamma-ray detectors. *Nuclear Instruments and Methods in Physics Research A*, 380:232–237, 1996.

72. P.N. Luke and E.E. Eissler. Performance of CdZnTe coplanar-grid gamma-ray detectors. *IEEE Transactions on Nuclear Science*, 43(3):1481–1486, 1996.

73. T.M. Maddern and L.M. Mitchell. Ion transport in xenon gas applications to double beta decay. *Nuclear Instruments and Methods in Physics Research A*, 359:506–510, 1995.

74. G.J. Mahler, B. Yu, G.C. Smith, W.R. Kane, and J.R. Lemley. A portable gamma-ray spectrometer using compressed xenon. *IEEE Transactions on Nuclear Science*, 45(3):1029–1032, 1998.

75. D.S. McGregor, R.A. Rojeski, Z. He, D.K. Wehe, M. Driver, and M. Blakely. Geometrically weighted semiconductor Frisch grid radiation spectrometers. *Nuclear Instruments and Methods in Physics Research A*, 422:164–168, 1999.

76. G.D. Minakov, Yu.N. Pestov, V.S. Prokopenko, and L.I. Shekhtman. Performance of gas microstrip chambers on glass with ionic and electronic conductivity. *Nuclear Instruments and Methods in Physics Research A*, 326:566–569, 1993.

77. W. R. Nelson, H. Hirayama, and D. W. O. Rogers. *The EGS4 Code System (SLAC-Report-265)*. The Department of Energy, December 1985.

78. H. Okada, T. Doke, K. Hasuike, J. Kikuchi, K. Masuda, M. Shinoda, T. Takahashi, and K. Terasawa. Time stability of liquid xenon photoionization detectors. *Nuclear Instruments and Methods in Physics Research A*, 374:188–192, 1996.

79. P. Olmos, J.M. Perez, G. Garcia-Belmonte, A. Bru, and J.L. de Pablos. Computer simulations of the behaviour of the partial charge collection model in thick hgi_2 gamma detectors. *Nuclear Instruments and Methods in Physics Research A*, 302:91–104, 1991.

80. F. Ortuno-Prados and C. Budtz-Jorgensen. The electron-conducting gas sCHOTT s8900 as substrata for microstrip gas chamber. *Nuclear Instruments and Methods in Physics Research A*, 364:287–289, 1995.

81. R.L. Palmer and G.C. Tepper. Development of a high-pressure xenon ionization chamber gamma-ray spectrometer for field deployment in cone penetrometers. *Journal of Radioanalytic and Nuclear Chemistry*, 248(2):289–294, 2001.

82. Yu.N. Pestov and L.I. Shekhtman. Influence of the bulk resistivitgy of glass with electronic conductivity on the performance of microstrip gas chamber. *Nuclear Instruments and Methods in Physics Research A*, 338:368–374, 1994.

83. P.C.P.S. Simoes P.J.B.M. Rachinhas, J.A.M. Lopes, T.H.V.T. Dias, R.E. Morgado, J.M.F. dos Santos, A.D. Stauffer, and C.A.N. Conde. Simulation and experimental results for the detection of conversion electrons with gas proportional scintillation counters. *Nuclear Instruments and Methods in Physics Research A*, 441:468–478, 2000.

84. P.J.B.M. Rachinhas, T.H.V.T. Dias, F.P. Santos, C.A.N. Conde, and A.D. Stauffer. Absorption of electrons in xenon for energies up to 200 keV: a Monte Carlo simulation study. *IEEE Transactions on Nuclear Science*, 46(6):577–579, 1999.

85. P.J.B.M. Rachinhas, T.H.V.T. Dias, F.P. Santos, A.D. Stauffer, and C.A.N. Conde. Monte Carllo simulation of xenon filled cylindrical proportional counters. *IEEE Transactions on Nuclear Science*, 41:984–988, 1994.

86. P.J.B.M. Rachinhas, T.H.V.T. Dias, F.P. Santos, A.D. Stauffer, and C.A.N. Conde. Energy resolution of xenon proportional counters: Monte Carlo and experimental results for 5.9 keV x-rays. *IEEE Nuclear Science Symposium Conference Record*, 1:90–92, 1995.

87. P.J.B.M. Rachnihas, T.H.V.T. Dias, A.D. Stauffer, F.P. Santos, and C.A.N. Conde. Energy resolution of xenon proportional counters: Monte Carlo

simulation and experimental results. *IEEE Transactions on Nuclear Science*, 43(4):2399–2405, 1996.

88. M. Salomon, J. Armitage, G. Chapman, M. Dixit, J. Dubeau, W. Faszer, L.A. Hamel, and G. Oakham. Passivation of gas microstrip detectors and stability of long-term operation. *Nuclear Instruments and Methods in Physics Research A*, 351:313–316, 1994.

89. F.P. Santos, T.H.V.T. Dias, P.J.B.M. Rachinhas, C.A.N. Conde, and A.D. Stauffer. The w-value and the Fano factor for x-rays in xenon-neon gas mixtures: a Monte Carlo simulation study. *IEEE Nuclear Science Symposium Conference Record*, 1:572–576, 1999.

90. F.P. Santos, T.H.V.T Dias, P.J.B.M. Rachinhas, A.D. Stauffer, and C.A.N. Conde. The electroluminescence of Xe-Ne gas mixtures: a Monte Carlo study. *IEEE Transactions on Nuclear Sciences*, 45(2):176–185, 1998.

91. F.P. Santos, T.H.V.T. Dias, A.D. Stauffer, and C.A.N. Conde. Variation of energy linearity and w value in gaseous xenon radiation detectors for x-rays in the 0.1 to 25 keV energy range: a Monte Carlo simulation study. *Nuclear Instruments and Methods in Physics Research A*, 307:347–352, 1991.

92. F.P. Santos, J.M.F. dos Santos, T.H.V.T. Dias, and C.A.N. Conde. Pulse-height-spectrum distortion in xenon gaseous detectors for soft X rays: experimental results. *IEEE Transactions on Nuclear Science*, 42:611–614, 1995.

93. F. Sauli. Recent developments and applications of fast position-sensitive gas detectors. *Nuclear Instruments and Methods in Physics Research A*, 422:257–262, 1999.

94. M.L. Simpson, T.W. Raudorf, T.J. Paulus, and R.C. Trammell. Charge trapping corrections in Ge spectrometers. *IEEE Transactions on Nuclear Science*, 36(1):260–266, 1989.

95. R.K. Sood, Z. Ye, and R.K. Manchanda. Ultra-high pressure proportional counters, part ii. xenon. *Nuclear Instruments and Methods in Physics Research A*, 344:384–393, 1994.

96. L.M.N. Tavora, E.J. Morton, F.P. Santos, and T.H.V.T. Dias. Simulation of x-ray tubes for imaging applications. *IEEE Transactions on Nuclear Science*, 47(4):1493–1498, 2000.

97. G. Tepper. Personal Communication, 2002.

98. G. Tepper and J. Losee. High resolution room temperature ionization chamber xenon gama radiation detector. *Nuclear Instruments and Methods in Physics Research A*, 356:339–346, 1995.

99. G. Tepper and J. Losee. A compressed xenon ionization chamber x-ray/gamma-ray detector incorporating both charge and scintillation collection. *Nuclear Instruments and Methods in Physics Research A*, 368:862–864, 1996.

100. G. Tepper, J. Losee, and R. Palmer. A cylindrical xenon ionization chamber detector for high resolution, room temperature gamma radiation spectroscopy. *Nuclear Instruments and Methods in Physics Research A*, 413:467–470, 1998.

101. N. Tralli. *Classical Electromagnetic Theory*. McGraw-Hill Book Company, Inc., New York, NY, 1963.

102. G.L. Troyer, B.D. Keele, and G.C. Tepper. Pulse rise-time characterization of a high pressure xenon gamma detector for use in resolution enhancement. *Journal of Radioanalytics and Nuclear Chemistry*, 248(2):267–271, 2001.

103. G.A Tutin, I.V. Ryzhov, V.P. Eismont, A.V. Kireev, H. Conde, K. Elmgren, N. Olsson, and P.-U. Renberg. An ionization chamber with frisch grids for studies of high-energy neutron-induced fission. *Nuclear Instruments and Methods in Physics Research A*, 456:646–652, 2001.

104. S.E. Ulin, V.V. Dmitrenko, A.E. Bolotnikov, K.F. Vlasik, A.M. Galper, V.M. Grachev, O.N. Kondakova, V.B. Komarov, S.V. Krivov, S.V. Minaev, S.I. Suchkov, Z.M. Uteshev, I.V. Chernysheva, and Yu.T. Yurkin. Cylindrical high-pressure xenon detector of gamma radiation. *Instruments and Experimental Techniques*, 37(2):142–145, 1994.

105. S.E. Ulin, V.V. Dmitrenko, V.M. Grachev, O.N. Kondakova, S.V. Krivov, Z.M. Uteshev, K.F. Vlasik, Yu.T. Yurkin, and I.V. Chernysheva. A cylindrical ionization chamber with a shielding mesh filled with xenon under a pressure of 50 atm. *Instruments and Experimental Techniques*, 38(3):326–330, 1995.

106. C. S. Walker. *Capacitance, Inductance, and Crosstalk Analysis*. Artech House, Inc., Norwood, MA, 1990.

107. F. Zhang and Z. He. Personal Communication, 2002.